IMPACT OF COHESION FORCES ON PARTICLE MIXING AND SEGREGATION

by

Hongming Li

B.S., Tianjin University, China, 1992

M.S., University of Pittsburgh, 2002

Submitted to the Graduate Faculty of

the School of Engineering in partial fulfillment

of the requirements for the degree of

Doctor of Philosophy

University of Pittsburgh

2005

UNIVERSITY OF PITTSBURGH

SCHOOL OF ENGINEERING

This dissertation was presented

by

Hongming Li

It was defended on

June 20, 2005

and approved by

Joseph J. McCarthy, Ph.D., Associate Professor, Chemical and Petroleum Engineering

Robert Enick, Ph.D., Professor, Chemical and Petroleum Engineering

Sachin S Velankar, Ph.D., Assistant Professor, Chemical and Petroleum Engineering

Patrick Smolinski, Ph.D., Associate Professor, Mechanical Engineering)

Dissertation Director: Joseph J. McCarthy, Ph.D., Associate Professor, Chemical and Petroleum Engineering

ABSTRACT

IMPACT OF COHESION FORCES ON PARTICLE MIXING AND SEGREGATION

Hongming Li, PhD

University of Pittsburgh, 2005

The objective of this work is to advance the fundamental understanding of mixing and segregation of cohesive granular materials. Cohesion can arise from a variety of sources: van der Waals forces, electrostatic forces, liquid bridging (capillary) forces. These forces may play a significant role in the processing of fine and/or moist powders in many industries, from pharmaceuticals to materials synthesis; however, despite its prevalence, there is only limited information available in the literature on processing of cohesive materials. Instead, the vast majority of work has been directed at the study of non-cohesive (i.e., free-flowing) particles, and a wealth of information has been learned about the behavior of cohesionless materials. With growing emphasis on controlling the structure of materials at increasingly small length-scales (even tending toward the nano-scale), understanding the effects of particle interactions – which tend to dominate at smaller length-scales – on processing operations has become more important than ever.

This project focuses on the effects of cohesion on mixing and segregation in simple, industrially-relevant, granular flows. In particular, the paradigm cases of a slowly rotated tumbler and the flow in a simple shear cell are examined. We take a novel approach to this problem, placing emphasis on microscopic (particle-level), discrete modeling so as to take as its staring point the well understood interaction laws governing cohesion (capillary, van der Waals, etc.), and build to the view of the macroscopic flow via experiment and Particle Dynamics Simulation. We develop and use discrete characterization tools of cohesive

behavior in order to construct a simple theory regarding the mixing and segregation tendency of cohesive granular matter. This theory allows us to analytically determine a phase diagram, showing both mixed and segregated phases, and agrees both quantitatively and qualitatively with experiment. These results have implications for industrial mixing/separation processes as well as novel particle production methods (e.g., engineered agglomerates with precisely prescribed compositions).

DESCRIPTORS

Capillary force	Cohesion
Granular material	Interparticle forces
Liquid-bridge	Mixing/segregation
Particle dynamics	van der Waals force

TABLE OF CONTENTS

LIST OF TABLES

LIST OF FIGURES

PREFACE

Inspired by my curiosity for scientific research, I started my graduate study in 2000 in my early 30's and joined Prof. McCarthy's Granular Transport Group in January of 2002. My Ph.D. thesis fulfilled my intellectual curiosity and made full use of my knowledges and experiences. In particular I learned the most important things about research from Prof. McCarthy — spirited thinking, strict derivation and professionalism — , thanks to his extreme patience and enlightening instruction. I'm deeply grateful to Prof. McCarthy for his never-ending input to the cultivation of his graduate students.

I would like to thank my colleagues who accompanied me through all my happy or tough times at the University of Pittsburgh: Ann Hays, Adetola Abatan, Deliang Shi, Kunal Jain, John Harrold and Abhishek Soni. Particularly I am grateful to Deliang Shi and Adetola Abatan for their invaluable discussion with me about my project.

Finally, I would like to dedicate this work to my wife, Yeni Wang, for her support and sacrifice, as well as to my son, Xiushi Li, and my daughter, Sylvia(Xiuzhu) Li for their smiles when I am home. I also acknowledge my parents and parents-in-law for their supports of my family during my studies.

1.0 INTRODUCTION

Granular materials are simply assemblies of a large number of discrete particles, yet are quite central to many industries like pharmaceuticals, ceramics, coating, food processing, agrochemicals, basic chemicals, mineral processing and so on. There are a number of particle processing unit operations in these industries, such as packing, conveying, coating, drying, mixing and segregation, to name a few. It has been estimated that 40 percent of the value added to the U.S. chemical industry is linked to particle technology[2]. There are enormous costs associated with handling these materials. For example, a straightforward process such as crushing ores uses approximately 1-3 percent of the U.S. annual energy consumption[3]. Therefore, there is no doubt that particle technology is quite important, especially when considering today's tough demands of increased production rates, tight quality control, and minimization of product loss.

Despite the fact that a substantial amount of work has been directed at the study of particles[4, 5, 6, 7, 8, 9, 10, 11], a fundamental understanding of the behavior of granular material still remains poor. Most of the particulate handling knowledge is still empirical and no general approach to analyzing these flows exists. According to a recent study of 40 solids processing plants in the U.S. and Canada, 80 percent of the facilities experienced solids handling problems[12]. Furthermore, once operational, handling problems continued, resulting in performance of only 40 to 50 percent that of design [12]. This disconnect can be attributed to several unique characteristics of granular materials:

1. **Granular materials behave differently from other familiar forms of matter.** They can withstand some stress without deformation, like solids; they can be made to flow, like liquids; and they also can be compressed, like gases[13]. These properties of

granular materials make them very hard to analyze[14]. A typical example is, that there is no particulate motion equivalent to the molecular diffusion of gases and liquids, and actually the randomization rate of particles is determined by the flow characteristics or the method used to handle the particles[15].

2. **Granular materials tend to segregate or demix.** Segregation is commonly observed in granular flow when differences exist in the properties of the materials — e.g., size, density or shape. Often these differences cause particles to segregate into different regions of a container when sheared or vibrated[4, 5, 6]. This is contrary to that encountered in fluid mixing, where more agitation implies better mixing[16].
3. **There is no accepted universal continuum description for granular material flow.** Because of the intrinsic physical complexity of granular material flow (e.g., discontinuous and inhomogeneous), and also the difficulty in experimental measurement of properties of their flow (e.g., void fraction, velocity profiles and particle positions), a accepted universal continuum description for granular material flow has not been developed to date.

Cohesion forces between particles have a significant effect on the properties of granular material. For example, it is well known that the angle of repose of a wet granular pile is greater than that of a dry pile made of the same material, making things like sand castles possible. This effect is caused by capillary forces which are introduced by liquid bridges formed between particles. Many of the industries which deal with particulate materials are in some way affected by cohesion, most notably the pharmaceutical, metallurgical, and pigment industries. Cohesion between particles could arise from a variety of sources: van der Waals forces, electrostatic forces, and liquid bridging (capillary forces). As the particle size decreases, these inter-particle forces become increasingly important, and substantial departure from the behavior of free-flowing particulate systems becomes evident.

In traditional approaches to granular flow[17], the global effects of particle cohesion have long been incorporated into a continuum model as an offset from the origin of the stress-strain curve. However, it is difficult to distinguish between modes of cohesion with this method. In addition, due to relatively small sizes of particles in a typical cohesive system, the experimental measurement of the properties of the bulk flow is more difficult and un-

reliable compared to non-cohesive systems. These issues, in part, explain why the vast majority of present research has been directed at the study of free-flowing particles and a body of literature has been published about the behavior of cohesionless materials[4, 5, 6, 7, 8, 9, 10, 11], while cohesive materials have received only limited attention[18, 19].

In this work, we study the effect of cohesion on particle mixing/segregation operations. Based on the well understood interaction laws governing each mode of cohesion (capillary, van der Waals, etc.), we take a novel approach to this problem by developing microscopic, discrete models which could connect the macroscopic properties of the granular flow to the effects of inter-particle forces. Contrary to a traditional (macroscopic) approach to this problem, which doesn't account for the origin of cohesion, discrete (microscopic) characterization tools are developed by our group to directly quantify a *priori*, the effect of cohesion on the flow of the material. To achieve these goals, a combination of experiment and computer simulation is used in simple, industrially-relevant, granular flows.

This dissertation is organized as follows. Part II covers relevant background about mechanisms of mixing and segregation, and cohesion in granular materials. Also included is a discussion of a discrete modeling technique — Particle Dynamics — which is commonly used to simulate granular flows. Finally, the previous work of our group related to cohesive characterization is reviewed. Part III examines the successful use of a discrete view of cohesion in particle mixing and segregation both in the systems where shearing effects are negligible and in the systems where shearing effects are important. Also covered is a discussion about the impact of van der Waals interactions on the behavior of adhesive particles. Finally the conclusions and outlook are addressed in part VI.

1.1 MIXING

Mixing is a operation in which a relatively homogeneous substance is obtained from two or more ingredients[20], aimed at the manufacture of a product of an acceptable quality or to control rates of heat transfer, mass transfer or chemical reaction[21]. For example in pharmaceuticals, a single medicine tablet might be comprised of more than 5 or 10 ingredients which are physically mixed. Each ingredient has its own function: either to cure the ill, enhance absorption, minimize side effects, make the pill taste good, or even just for beauty(color)[22]. The results of such mixing operations are often critical processing steps. From the same example, with insufficient active ingredient, the product will lack potency, with too much active ingredient, the product will cause side effects.

Unlike mixing miscible liquids or mixing a soluble solid into a liquid, it can be difficult to achieve a homogeneous result when mixing two or more solids. Inspired by the problems industries encounter during granular material processing, much of the work in granular mixing has been directed either to studies of the action of specific mixers and the design of mixers — e.g., tumbling[23], air-driven mixing[24], and grinding[25] or to kinetics studies[26, 27, 28] — e.g, how much time it will take for a given combination of materials to mix. Fundamental knowledge about solid mixing — e.g., discussing how mixing works or predicting the rate of mixing for a given combination of components (particles) — is rare, especially compared to liquid mixing[29].

Several mechanisms of solid mixing were originally proposed by Lacey(1954)[30]:

Convective mixing: *the transfer of groups of particles from one location to another.* The macroscopic transport of groups of particles is often referred to as convective mixing. Groups of particles move relative to one another, and this relative motion between aggregates causes a macroscopic mixing of the particles (see Figure 1).

Shear mixing: *the setting up of slipping planes within the mass.* Shearing forces acting on the particles cause bed dilation and oblique inter-particle collision, and can result in relative motion between particles (see Figure 1).

Dispersive mixing: *the distribution of particles over a freshly developed surface.* When particles roll down a free surface, a one-dimensional random walk occurs in the direction

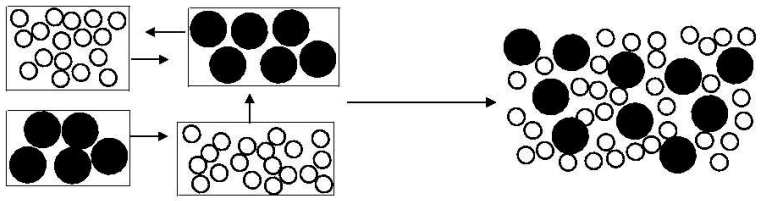

Convective mixing

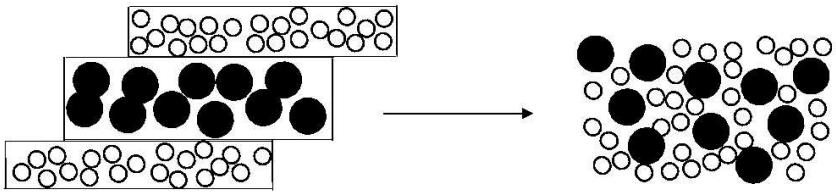

Shearing mixing

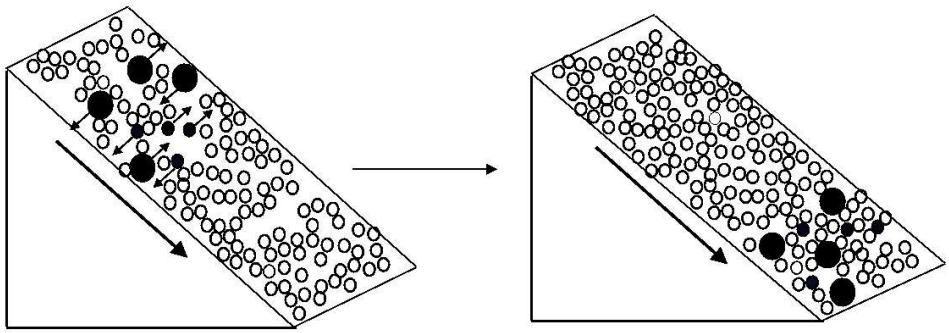

Dispersive mixing

Figure 1: Mixing mechanisms

perpendicular to the mean particle motion, induced by collisions between the migrating particles and particles on the surface[29]. For example, when the particles roll down a slope or rotate in tumbler, dispersive mixing occurs (see Figure 1).

1.2 SEGREGATION

Segregation, which is a commonly observed phenomena in many industrial operations (e.g., tumbling, conveying, and fluidization, etc., Figure 2), invariably occurs in competition with particle mixing[31, 32, 33, 34, 35]. An asymptotic state may be reached when the rates of mixing and segregation are equal and the particle distribution is statistically constant[20]. There are many causes of this phenomenon. Typically, differences in the sizes, densities and/or shapes of particles will cause segregation while the particles are in movement. In his review paper about segregation, Williams proposed three mechanisms of segregation[36]:

Trajectory segregation If a particle of diameter d and density ρ is projected horizontally with velocity v into a fluid of viscosity μ, the stopping distance, —the distance the particle travels horizontally — is:

$$S = \frac{v\rho d^2}{18\mu}. \tag{1.1}$$

An example of trajectory segregation is when particles come off a conveyor belt in the mine, food or chemical industries (see Figure 3)[37]. Based on this equation, it is seen that a particle twice as large can proceed four times as far as its smaller counterpart, but a particle twice as dense can only proceed twice as far.

Percolation segregation Percolation segregation is very common in any granular processing operation where there is a difference in particle size. In a system comprised of particles with different sizes, a particle will be prevented from moving within a bed by the surrounding particles. When flow occurs, the particle bed must dilate. This dilation causes the larger particles to yield a space into which the smaller ones can pass and proceed to the bottom of the container (see Figure 3)[37].

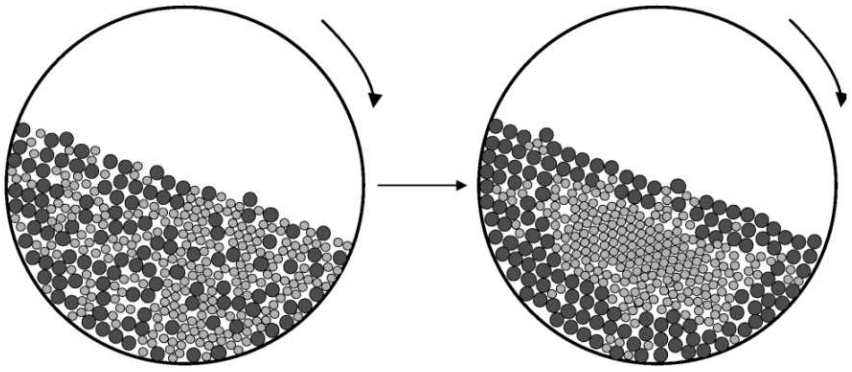

Tumbling segregation

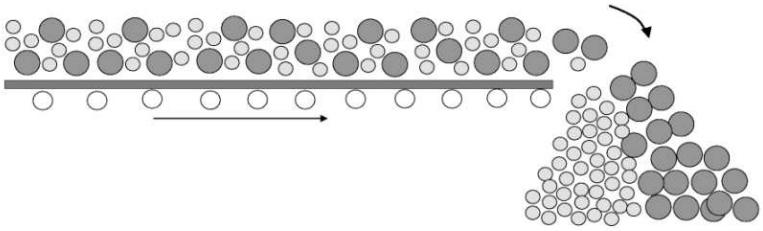

Conveying segregation

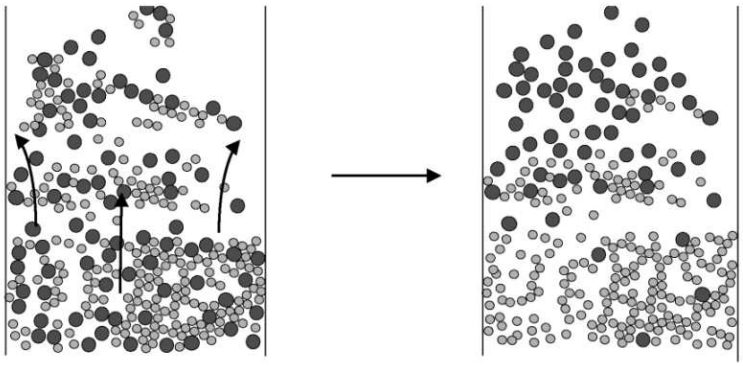

Fludization segregation

Figure 2: Industrial operational segregations

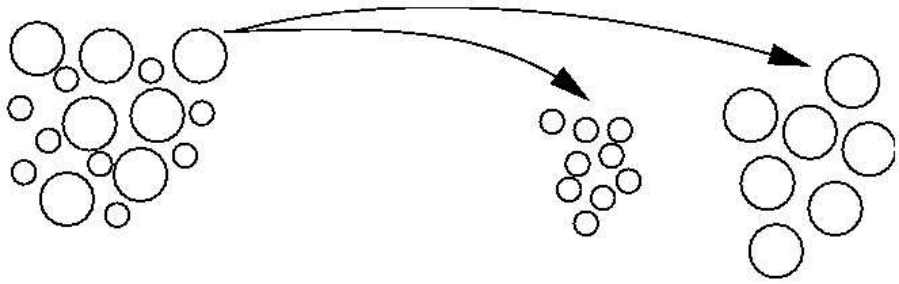

Trajectory segregation

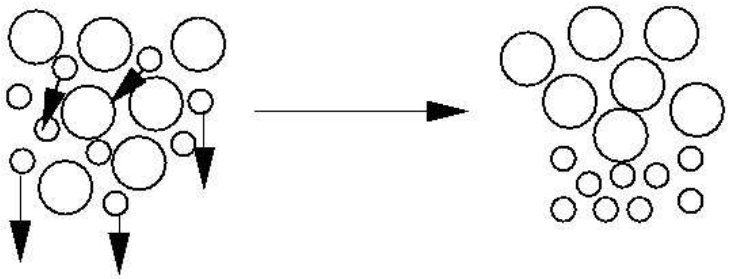

Percolation segregation

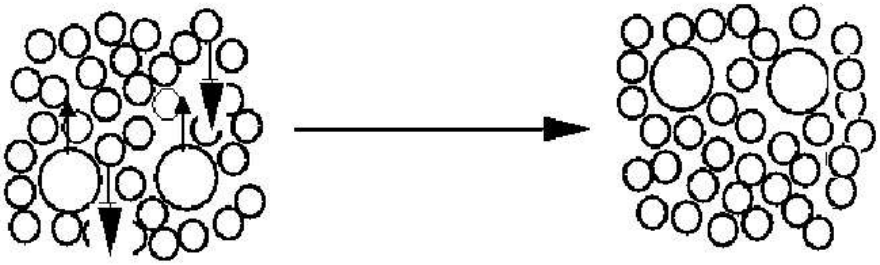

Rise of coarse particle

Figure 3: Segregation mechanisms

The rise of coarse particles on vibration When a granular system comprised of different sizes of particles is vibrated, the granular (collisional) pressure below a large particle is high so that it prevents the particles from moving downward, however, any upward movement allows small particles to run in under the large particle, and eventually the large particle can be made to migrate to the surface[36] (see Figure 3).

2.0 COHESION IN GRANULAR MATERIALS

Cohesion between particles can arise from a variety of sources: capillary forces, van der Waals forces, electrostatic forces, and can have a significant effect on the behavior of the granular material[38]. However the vast majority of work has been directed at the study of non-cohesive (i.e., free-flowing) particles[39, 40, 41, 35, 42, 43, 8, 9, 44, 45, 46], and a wealth of information has been learned about the behavior of cohesionless materials. With growing emphasis on controlling the structure of materials at increasingly small length-scales (even tending toward the nano-scale), understanding the effects of particle interactions – which tend to dominate at smaller length-scales – on processing operations has become more important than ever.

2.1 ORIGINS OF COHESION

2.1.1 Capillary forces

Capillary forces are induced by liquid bridges formed between particles. The total capillary force is the sum of the surface tension force and the force created by the pressure difference across the air-liquid interface[37]. Depending on the amount of liquid added to the system, there are four degrees of saturation (see Figure 4)[47]: pendular, funicular, capillary and droplet.

In the pendular regime, all liquid bridges are separate and independent, and the attractive forces between particles are larger relative to those in the other three regimes[37]. With the addition of more liquid to the system, the saturation degree of the system changes first to funicular, then capillary and finally reaches the droplet state.

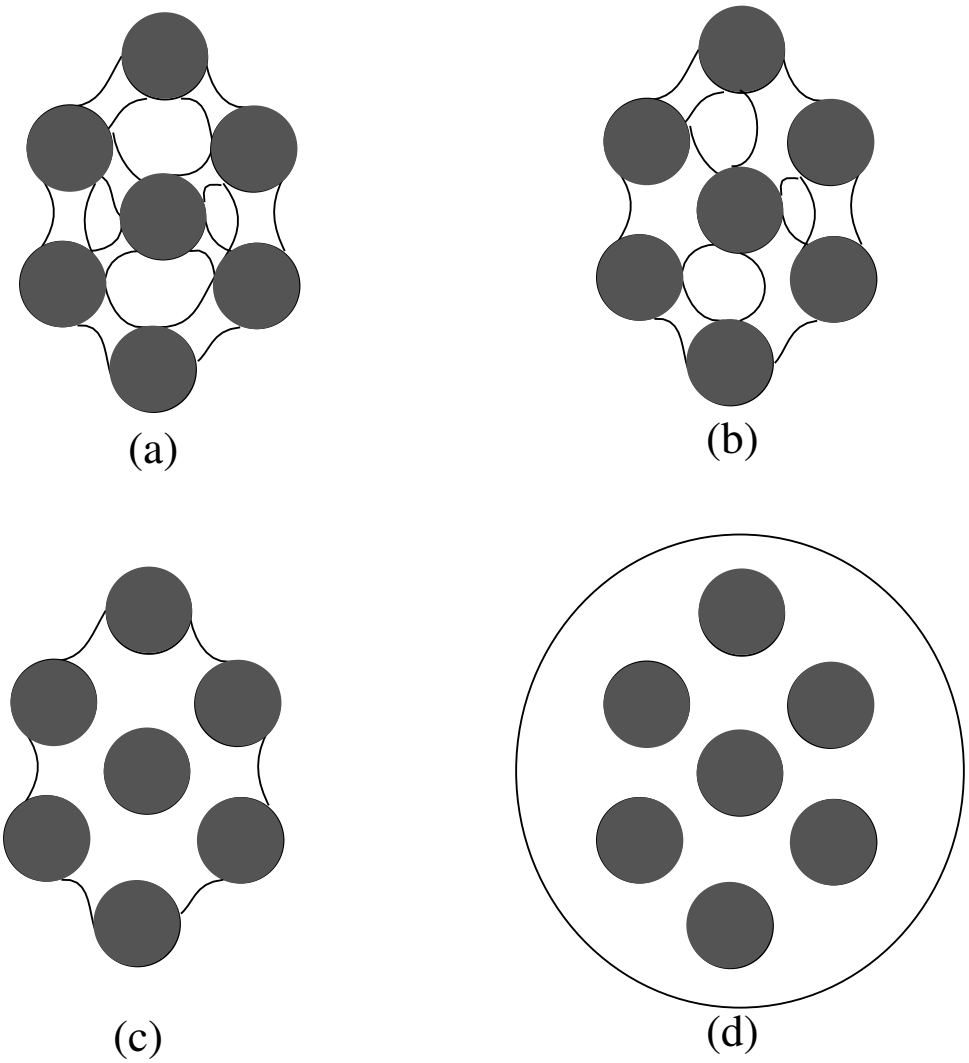

Figure 4: Degrees of liquid saturation: (a) pendular; (b) funicular; (c) capillary; (d) droplet.

A schematic pendular bridge is seen in Figure 5. The equation for the capillary force is as follows:

$$F_c = 2\pi R\gamma sin^2\beta[1 + \frac{R\Delta P}{2\gamma}], \tag{2.1}$$

where R is the particle radius, γ is the fluid's surface tension, β is the half-filling angle, and ΔP represents the pressure difference. The capillary force equation is further developed in Section 4.3 to incorporate this force into the Particle Dynamics simulations for cohesive (liquid-bridge induced) systems.

Viscous forces should also be considered when particles with connecting liquid bridges undergo relative motion. In the limit of rigid spheres, the normal viscous force can be calculated using[48]:

$$F_{v_n} = 6\pi\mu R v_n \frac{R}{S} \tag{2.2}$$

where μ is the interstitial fluid's viscosity, v_n is the relative normal velocity of the spheres, and S is the separation between particles. In the tangential direction, Goldman *et al.*'s solution[49] for the viscous force between a sphere and a planar surface should be used and is given by

$$F_{v_t} = (\frac{8}{15} ln \frac{R^*}{S} + 0.9588) 6\pi\mu R^* v_t, \tag{2.3}$$

where v_t is the relative tangential velocity of the spheres.

2.1.2 van der Waals forces

van der Waals interactions are caused by induced electrostatic attractions between molecules[50]. The electrons in an atom can arrange themselves anywhere within their orbitals, and may group toward one side of the molecule, thus creating a temporary slight negative charge on one side and positive on the other side. The nonpolar molecule neighboring that polar one will then tend to become polar with opposite polarity on the end close to the polar molecule[50]. van der Waals interactions are a function of the inter-particle spacing at the molecular level (see Figure 6[47]). When the distance increases, attraction takes place; as the

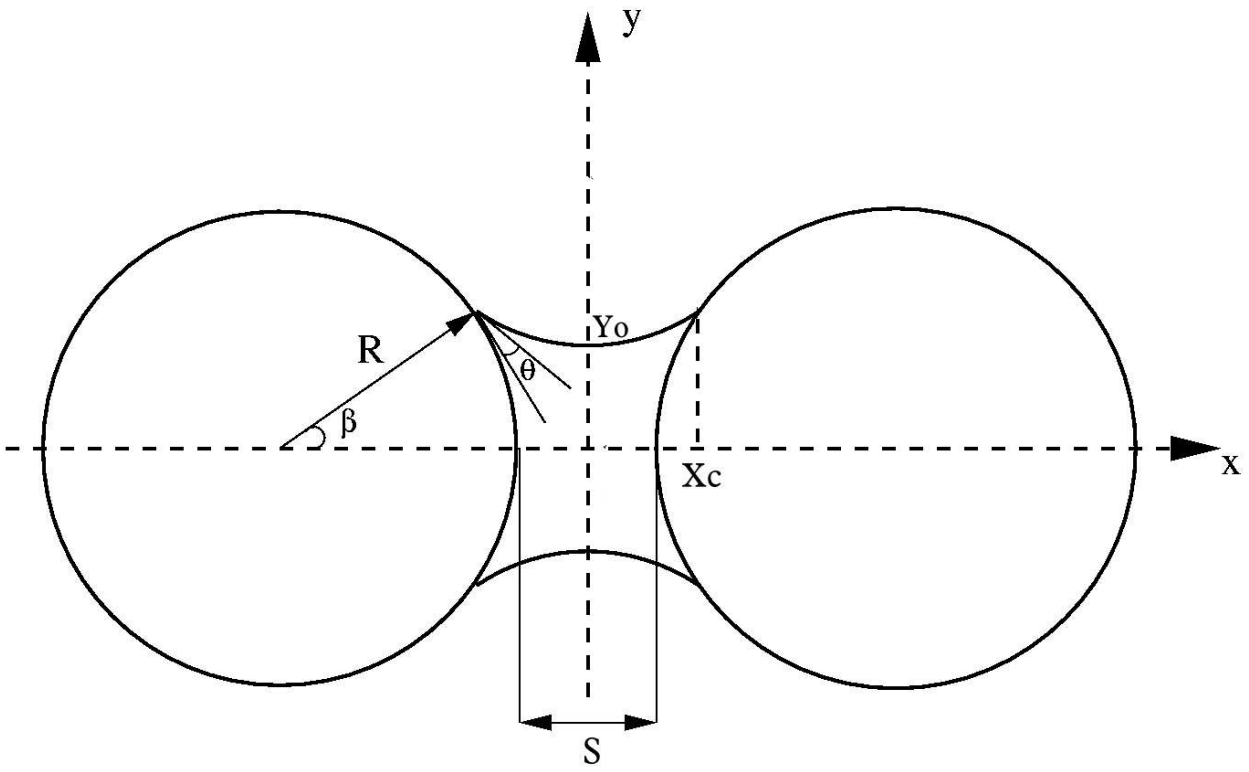

Figure 5: Schematic of a symmetric liquid bridge.

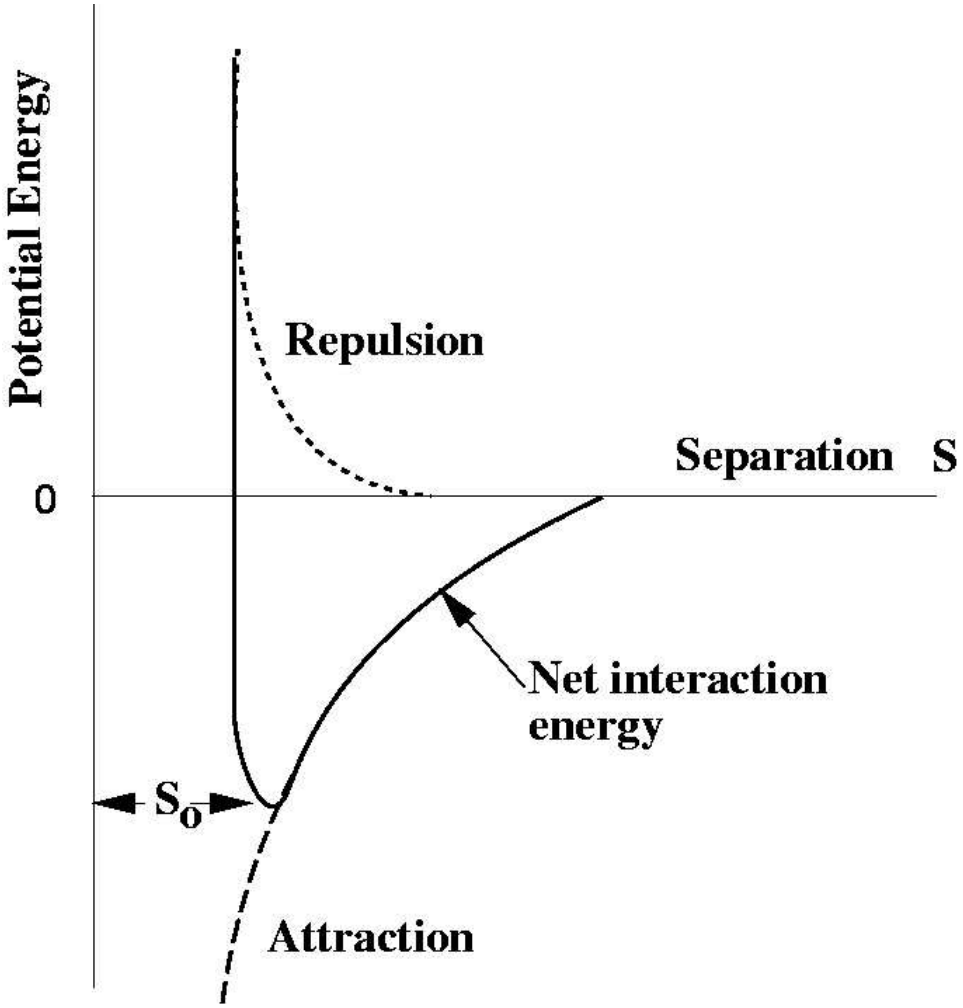

Figure 6: Potential energy diagram

distance decreases, the electron clouds associated with the molecules overlap, hence repulsion occurs. The total intermolecular pair potential is obtained by summing the attractive and repulsive potential. The van der Waals pair potential for two molecules can be represented as

$$W(r) = \frac{-C}{S^n}, \tag{2.4}$$

where C is a constant, r is the distance between the molecules and n could be taken as 6 as suggested by London[51]. The resulting force between the molecules is simply equal to

$$F(S) = \frac{dW(S)}{dS} = \frac{Cn}{S^{n+1}}. \tag{2.5}$$

Granular particles are large bodies containing many molecules. The Hamaker theory [52] assumes that the interaction energies between the isolated molecule and all the molecules in the large body are additive and non-interacting[53]. Thus the net interaction energy can be found by integrating the molecular interaction over the entire body, and can result in energy/force relations that are effective over vastly larger distances than when only a pair of molecules are considered[53]. For example, the interaction energy between a sphere and a surface can be

$$W(S) = \frac{-AR}{6S}, \tag{2.6}$$

and the resulting force is

$$F(S) = \frac{AR}{12S^2}, \tag{2.7}$$

where A is the Hamaker constant, R is the radius of the sphere and S is the distance between the sphere and the surface.

2.1.3 Electrostatic forces

Electrostatic forces can arise through friction (i.e., tribocharging) that leads to electrostatic charging of the objects, due to the electron transfer between objects[37]. The most common electrostatic force is the Coulombic force which corresponds to the case when both spherical particles are charged. The force acting between the two spherical particles is:

$$F_e = \frac{Q_1 Q_2}{4\pi\epsilon_r\epsilon_o S^2}, \tag{2.8}$$

where Q_i represents the charge on each particle 1 and 2, ϵ_o and ϵ_r are the permittivity of the free space and the relative permittivity of the interstitial fluid (ϵ_r=1 for air) , and S represents the distance between the particle centers[53]. If F_e is positive, then the force is repulsive; if it is negative, then it is attractive.

In addition to being attractive or repulsive, electrostatic forces, like van der Waals forces, do not require contact, but can actually act over relatively long distances compared to other inter-particle forces[37].

2.2 WET GRANULAR MATERIALS

Liquid-bridge induced cohesion forces can change behaviors of particles greatly, and has gained increasing attention in the literature.

The effect of liquid-bridge induced cohesion forces on the repose angle of particles has been extensively explored[54, 55, 56]. Hornbaker *et al*[54] conducted experiments with the addition of small quantities of oil to spherical beads. They observed that small quantities of liquid can lead to a large increase in the repose angle, clustering and correlation in grain motion. Bocquet *et al*[55] studied the effect of waiting time on the repose angle of glass beads contained in a rotating tumbler, and found logarithmic aging of the maximum static angle. They argued that this originates from capillary condensation of water vapor between the packed particles, which results in the formation of liquid bridges. As a result, the friction between different layers of granular particles and the maximum static angle are increased.

Some other experiments are directed at the effect of wet cohesion on particle mixing and segregation[57, 58, 18, 59]. Samadani and Kudrolli[57] poured a granular mixture slowly into a silo from a reservoir, and studied the images of the resulting piles. They observed that after a small amount of liquid is added, segregation is remarkably reduced. The segregation decreases rapidly with an increase in the amount of the liquid. They also stated that the extent of segregation decreases with increasing viscosity of the liquid. This may be interpreted as meaning that Samadani and Kudrolli's experiments do not represent the asymptotic distribution of particles due to the finite size of the pile. Geromichalos *et al*[58] horizontally shook a cylindrical jar containing bidisperse beads and varying amounts of water. They found a strong dependence of mixing on the liquid content, and that a transition to a viscoplastic regime, i.e, "perfect mixing", occurring at a critical liquid content.

In addition, Iveson and Litster[60, 61] conducted consolidation experiments to study the effects of liquid content and viscosity on granule strength. They found that the rate of consolidation increases with the amount of a low viscosity binder, and decreases with the amount of a high-viscosity binder. In other words, granule strength is controlled by the interaction of capillary, viscous and friction forces. Zhou *et al*[62] examined the effect of water addition on the packing of multi-sized coarse spheres under standard poured packing conditions. The results show that porosity is strongly affected by particle sizes and their distribution, in addition to water content.

3.0 REDUCTION OF SEGREGATION

Mixing and segregation mechanisms cannot usually be separated within a powder-handling system. The final mixture quality will be determined by the relative importance of the two mechanisms. Mitigating segregation is very important and necessary in order for a mixing process to achieve the best result. Nevertheless, methods of segregation reduction are largely empirical. Based both on the empirical experiences and understanding of mechanisms of mixing and segregation, several methods have been suggested to reduce segregation[63, 64].

First, since segregation occurs in an industrial setting primarily as a result of size differences, one strategy of segregation reduction lies in making the size of the components as similar as possible[64]. This technique is well known in the food, ceramics and pharmaceuticals industries. For example, when a small amount of flavoring is added to a food mixture, the flavor can be encapsulated with a gelatin additives to make its size similar to that of the majority of the other ingredients, thus expediting mixing [64]. Granulation[37, 65], a size increase technique to improve homogeneity, flow and compressibility, is widely used in pharmaceutical industry as well.

Typically, modifying other particle properties, such as density or surface chemistry/roughness, is not an option. If modifying size is not possible, then some other method of segregation reduction must be considered. As discussed in Section 1.2, the freedom to move relative to each other is one of the prerequisites for the occurrence of particle segregation. Therefore usually the relative movement between particles should be suppressed in favor of the mixing operation. Adding a small amount of liquid into the system can lessen the degree of relative movement between particles and may reduce the segregation under some conditions[63]. This technique is extensively in the pharmaceutical industry. It should be note that limiting mobility of particles also limits mixing in addition to segregation, since mixing depends on the relative movement between particles too.

Finally, if one of the components is very fine and the other is comparatively large, it has been suggested that the fines can be made to coat the surface of the large particles. In this way, segregation will not occur and it may be possible to achieve a mixture which is more homogeneous than a random mixture[66, 67] (see Figure 7). However, to date, no general technique for achieving this type of mixing has been developed.

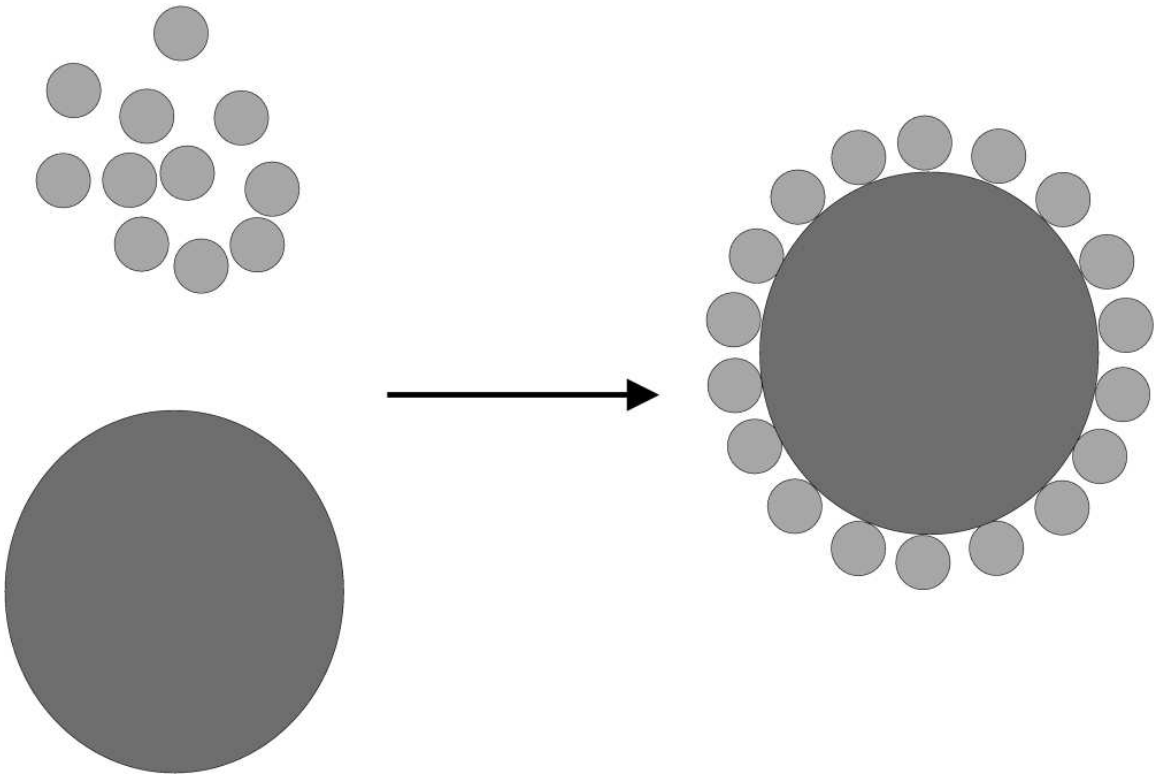

Figure 7: Coating larger particle with fine particles

4.0 PARTICLE DYNAMICS

Experiments with granular materials are difficult for several reasons. For example, the relatively small size of individual particles causes difficulties in measuring particle velocities and bed void fraction. Wall effects, which are encountered in almost every experiment, also affect the accuracy of experimental results. One technique which can be used to avoid these problems is discrete modeling of particulate flows – specifically Particle Dynamics Simulation (i.e., PD).

Particle Dynamics has been quite successful in simulating granular materials [68, 69, 70, 71, 72, 73, 74, 75, 76, 77, 78, 79, 80, 81], yielding insight into such diverse phenomena as force transmission [82], agglomerate formation and breakage [83], and segregation of cohesionless materials [84]. Since its inception in 1979 by Cundall and Strack [85], this type of approach has become quite prevalent and is an important tool in granular mechanics today. The basic advantage of the method over continuum techniques is that it simulates effects at the particle level. In other words, individual particle properties can be specified directly and the assembly performance, like segregation, is simply an output from the simulation. There is less need for global assumptions that are typically necessary but difficult to discern when using continuum models. On the other hand, the growth of the technique can be attributed, in part, to the increasing speed of modern computers.

4.1 METHODOLOGY

Depending on the bulk density and characteristics of the flow to be modeled, different methods of calculating the trajectories are used: hard-particle model and soft-particle model.

Hard-particle model The hard sphere model works in rapid, not-so-dense flows where the system exhibits instantaneous binary collisions. In this regime, one applies conservation of linear and angular momentum for each collision sequentially[86]. The collisions are typically inelastic with a coefficient of friction for tangential impact, and restitution for normal impact[87].

Soft-particle model A soft-particle technique is used in slow, dense granular flows where particles have enduring contacts and/or multi-particle collisions occur. In these flows, the particle trajectories are obtained via explicit solution of Newton's equations of motion for every particle at discrete time intervals.

In this project, we use a soft-particle model since the systems we are dealing with involve slow, dense granular flows. In this model, PD captures the bulk flow of the material via simultaneous integration of the interaction forces between individual pairs of particles, and the particle trajectories are obtained via explicit solution of Newton's equation of motion for every particle[85, 88]. Specifically, first the particle initial positions are reasonably (often randomly) assigned. From these positions all the forces acting on each particle are determined and the net acceleration of the particle is determined, both linear and angular. The positions and orientation at the end of the next time step are then evaluated explicitly using the method of integration initially adopted by Verlet and attributed to Störmer[89]

$$\dot{x}_{t+\frac{1}{2}\Delta t} = \dot{x}_t + \frac{1}{2}\ddot{x}_t \Delta t \ , \tag{4.1}$$

$$x_{t+\Delta t} = x_t + \frac{1}{2}(\dot{x}_t + \dot{x}_{t+\Delta t})\Delta t \ . \tag{4.2}$$

The particle positions are determined at certain time intervals. Constant or linearly varying conditions are assumed over the time interval, and hence the time interval must be small enough to maintain sufficient accuracy. If it is too large the errors become significant and the result are inaccurate or the model becomes unstable because it may lead to unrealistic big overlap and then large accelerations. If the time step is too small the computer run time will be unnecessarily long. Rounding errors can propagate over the time steps causing errors for time steps which are too small. Thornton and Randall([72]) suggest the time step be chosen to correspond with the Rayleigh wave speed so that

$$\Delta t = (\pi R/\alpha)(\rho/G)^{1/2} \tag{4.3}$$

where R is the particle radius, α is a constant (0.9-0.95), ρ is the particle density and G is the shear modulus.

4.2 CONTACT FORCE

The force models are integral to a soft particle simulation. These forces include external forces and contact forces. While external particle interaction forces (e.g., capillary force and van der Waals force, etc.) can be easily added, the forces in the system typically include only contact forces and gravity. The accuracy of a soft particle simulation is almost wholly dependent on the choice of contact mechanics, which may act in the direction normal to the contact surface (normal force) or tangential to the contact surface (tangential force). Cundall and Strack ([85]) first built their force model accounting for the contact mechanics through the use of a spring, a dash-pot and a slider configuration, as shown in Figure 8.

4.2.1 Normal force

In our work, the normal force is modeled as an elastic-plastic interaction after the work of Thornton[90]. The deformation of the particles is mimicked via a computational "overlap" (see Figure 9) so that $\alpha = (R_i + R_j) - \Delta_{ij}$, where R_i and R_j are the particle radii and Δ_{ij} is the distance between the centers of particle i and j. At the initial stages of loading (see Figure 10), the normal force, F, is purely elastic and is given by

$$F = k_n \alpha^{3/2}, \tag{4.4}$$

where k_n is the normal force constant from the Hertz theory[91]. This constant is a function of the particle radii, R, and elastic properties (Young's modulus, E, and Poisson ratio, ν):

$$k_n = \frac{4}{3} E^* \sqrt{R^*}, \tag{4.5}$$

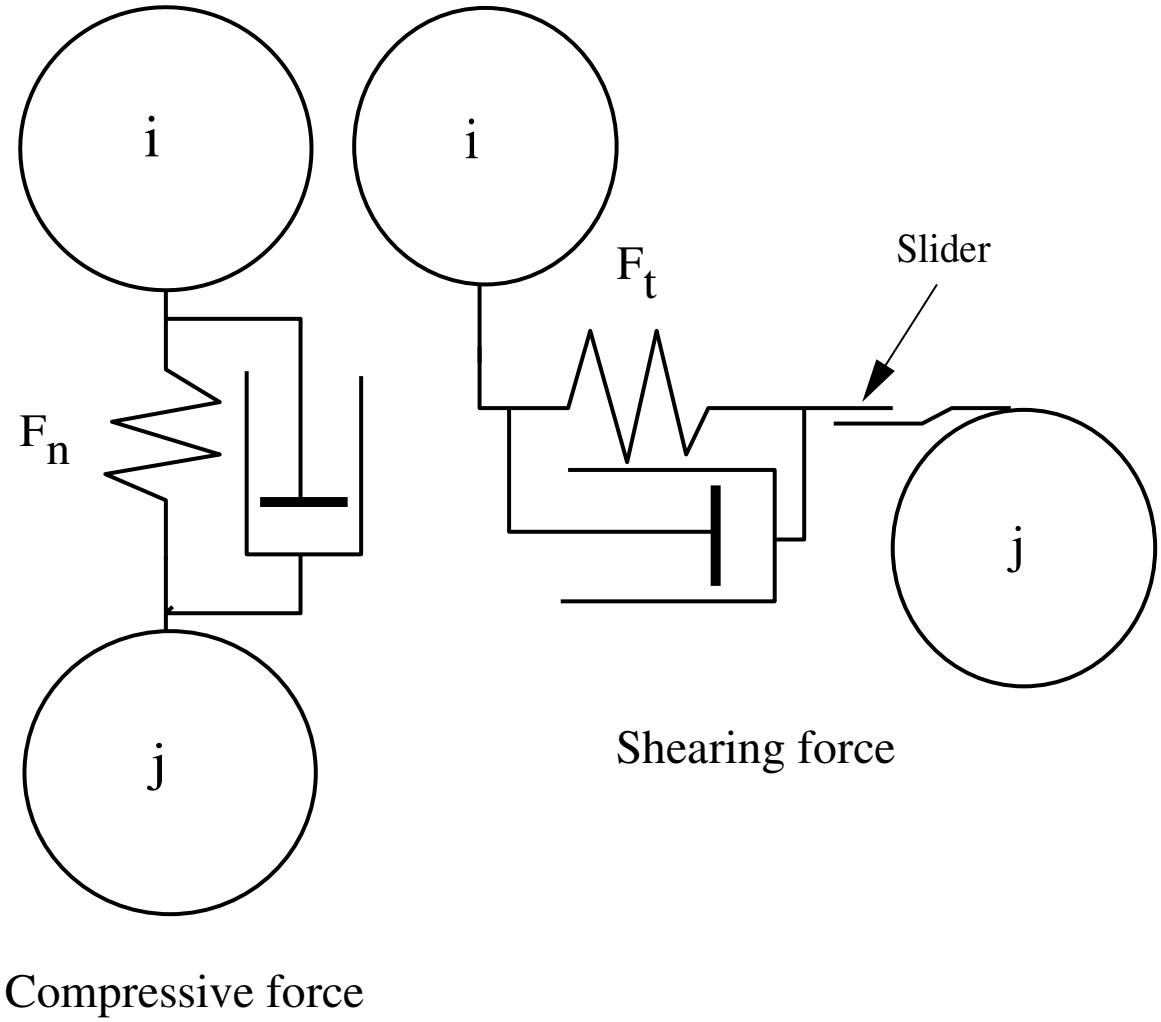

Figure 8: Contact forces modeling

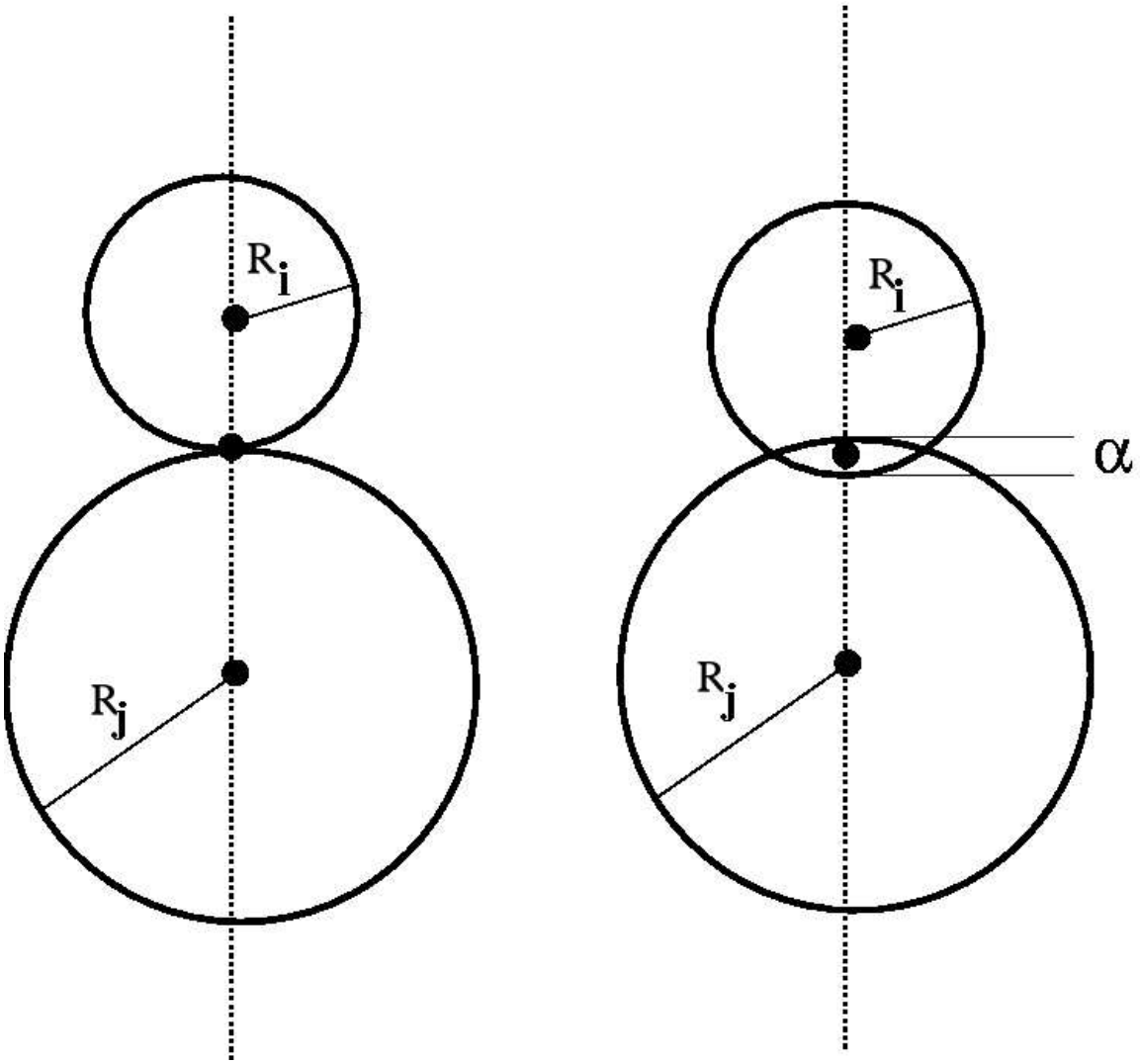

Figure 9: Contact point between two particles

where E^* and R^* are given by

$$\frac{1}{E^*} = \frac{1-\nu_1^2}{E_1} + \frac{1-\nu_2^2}{E_2} \tag{4.6}$$

$$\frac{1}{R^*} = \frac{1}{R_1} + \frac{1}{R_2} \tag{4.7}$$

respectively. Once the normal force exceeds a yield force, F_y (see Figure 10), further loading is given by the linear expression

$$F = F_y + k_y(\alpha - \alpha_y). \tag{4.8}$$

In this expression, k_y is the plastic stiffness which is related to the yield force by $k_y = (3/2)(F_y/\alpha_y)$, and α_y is the deformation at the point of yield. Unloading (see Figure 10) prior to exceeding the yield limit is purely elastic, while unloading after the yield limit is given by

$$F = F_{max} - k_n\sqrt{\bar{R}}(\alpha_{max} - \alpha)^{3/2}, \tag{4.9}$$

where F_{max} and α_{max} are the maximum force and deformation, respectively and $\bar{R}$ is the ratio of the new contact radius due to plastic deformation, R', to R^*,

$$\bar{R} = \frac{R'}{R^*} = \frac{F_y}{F_{max}}\left(\frac{2F_{max} + F_y}{3F_y}\right)^{3/2}. \tag{4.10}$$

4.2.2 Tangential force

Walton and Braun derived the tangential (frictional) force[77], and Walton gave a complete description of the implementation of this expression[92]. For each time-step, the new tangential force acting at a particle-particle contact, F_t, is given as:

$$F_t = F_{t_o} - k_t\Delta s, \tag{4.11}$$

where F_{t_o} is the old tangential force and $k_t\Delta s$ is the incremental change in the tangential force during the present time-step due to relative particle motion; i.e., Δs is the displacement

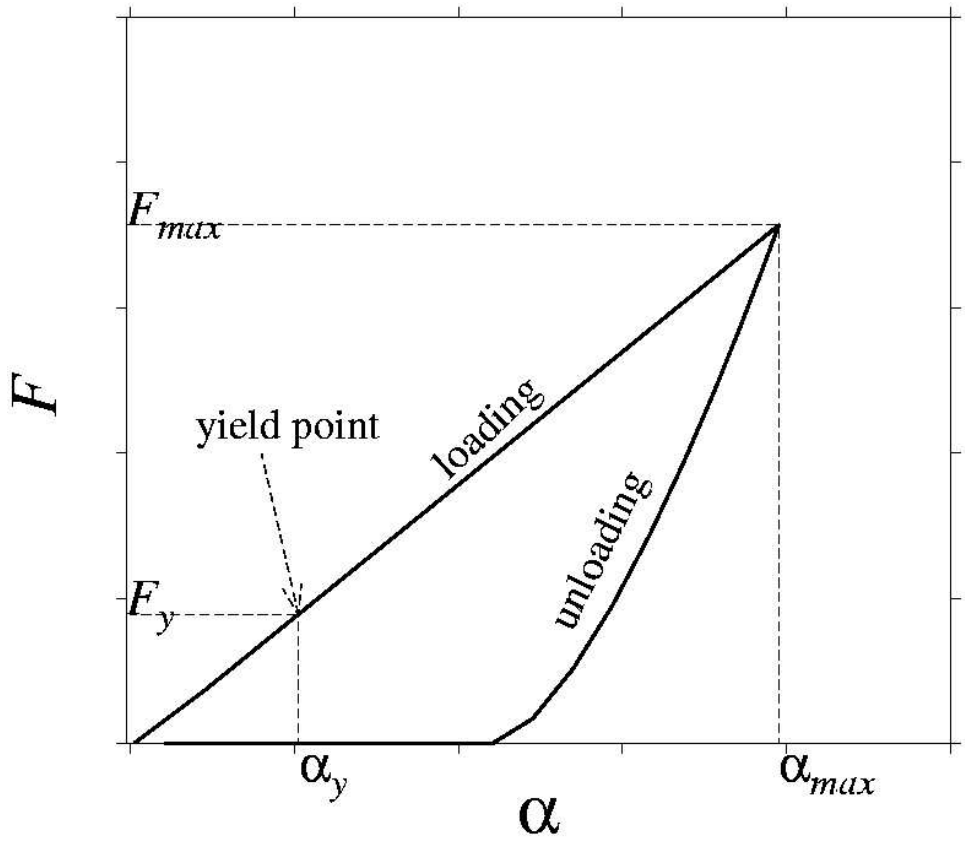

Figure 10: Force-displacement curve of elastic-plastic deformation without adhesion

during the present time-step. This displacement is easily calculated from the component of velocity tangent to the contact surface, v_t (i.e., $\Delta s = v_t dt$ where dt is the time-step). In order to mimic an annular region of microslip at the edge of the contact as well as limit the overall tangential force to the Amonton's Law limit ($F_t \leq \mu_f F_n$ where μ_f is the coefficient of sliding friction), the frictional stiffness, k_t, is given by the expressions[93]

$$k_t = k_{t_o}\left(1 - \frac{F_t - F_t^*}{\mu_f F_n - F_t^*}\right)^c, \quad for\ increasing\ F_t \tag{4.12}$$

$$k_t = k_{t_o}\left(1 - \frac{F_t^* - F_t}{\mu_f F_n + F_t^*}\right)^c, \quad for\ decreasing\ F_t. \tag{4.13}$$

F_t^* refers to F_t at the point where the direction of tangential slip changes. The constant c is usually set to (1/3) to parallel the expression from Mindlin [93] and k_{t_o} is the initial tangential stiffness. It should be noted that the rates of change of displacement with loading are similar for tangential versus normal interaction, and their ratio is given as

$$\frac{ds/dF_t}{d\alpha/dF_n} = \frac{1-\nu/2}{1-\nu}. \tag{4.14}$$

4.3 LIQUID-BRIDGE INDUCED COHESION FORCE

The capillary force induced by a liquid bridge accounts for both the surface tension and pressure difference over the interface. If the particle bed is assumed to remain in the pendular state, (i.e., liquid bridges act only pair-wise), then multiple particle interactions can be modeled as the sum of many two-body interactions[94, 95, 40].

The phenomenon of liquid bridging between particles was first treated quantitatively by Fisher[96], and recently by Lian, Thornton, and Adams[94]. Using these models, the cohesive force of a liquid bridge can be calculated as a function of particle separation. In addition to the capillary force, "wet" particles encounter a viscous force resisting motion, which can be derived from lubrication theory (see equation 2-2).

An approximate expression for the capillary force may be written as[94]

$$F_c = 2\pi R\gamma sin^2\beta + \pi R^2 \Delta P sin^2\beta, \tag{4.15}$$

where the first term is the force due to the surface tension of the fluid, and the second term is the force due to the pressure difference. R is the radius of the particle (see Figure 5), β is the half-filling angle, γ is the fluid's surface tension, and the contact angle is assumed as zero (a simplifying restriction that is easily removed), ΔP is the pressure deficiency across the air-liquid interface. This equation could be re-written as

$$F_c = 2\pi R\gamma sin^2\beta[1 + \frac{R\Delta P}{2\gamma}]. \tag{4.16}$$

Defining the dimensionless mean curvature, H^* as

$$H^* = \frac{R\Delta P}{2\gamma} \tag{4.17}$$

allows us to write the total capillary force now as

$$F_c = 2\pi R\gamma sin^2\beta[1 + H^*]. \tag{4.18}$$

The solution for the liquid bridge force may then be obtained by determining H^* from the Laplace-Young equation

$$2H^* = \frac{(d^2Y/dX^2)}{(1 + ((dY/dX)^2)^{3/2}} - \frac{1}{Y(1 + Y^2)^{1/2}}, \tag{4.19}$$

where Y signifies the position of the gas-liquid interface (see Figure 5).

By fixing the values of the half-filling angle, β, and the neck radius, Y_o, the boundary conditions are known (and the liquid-bridge volume and particle separations can be determined). The boundary conditions at $X = X_c$ (see Figure 5) are

$$Y = sin\beta \tag{4.20}$$

and

$$\frac{dY}{dx} = cot\beta, \tag{4.21}$$

while at $X = 0$ they are

$$Y = Y_o \tag{4.22}$$

and

$$\frac{dY}{dx} = 0. \tag{4.23}$$

This results in a liquid bridge volume of:

$$V = 2\pi \int_0^{X_c} Y\, dx - \frac{2}{3}\pi(1 - cos\beta)^2(2 + cos\beta), \tag{4.24}$$

and the separation between particle surfaces becomes:

$$S = 2(X_c - R(1 - cos\beta)). \tag{4.25}$$

By evaluating the solution for a range of half-filling angles, β, and neck radii, Y_o, and further tabulating the results as a function of liquid-bridge volume and particle separation, we can incorporate this force into a PD simulation.

4.4 APPLICATIONS OF PARTICLE DYNAMICS

PD simulations have become very popular in the field of multiphase flows pioneered by Tsuji, Kawaguchi and Tanaka[76]. The approach is a Lagrangina-Eulerian modeling of the multiphase fluidized medium. Kafui *et al*[97] simulated the fluidization of pseudo-2D bed. In this model, a numerical integration of the individual particle trajectories is coupled to a continuum integration of the Navier-Stokes equation of fluid motion. They examined the two forms of the coupling term, i.e., the **PGF** model (using the pressure gradient force) and **FDB** model (using a buoyancy force in a pseudo-2D fluidized bed), and found the **PGF** model generates results most consistent with empirical correlations. Li *et al*[98] built a model where the gas-liquid-solid flow in a fluidized bed is simulated by a combined method of the CFD

(Computational Fluid Dynamics), PD and VOF (Volume-of-Fluid). Kawaguchi *et al*[99] performed quasi-three-dimensional simulations of spouted beds in cylinder. The calculated spout diameter based on their model matches well with their experimental results.

Thornton's group has performed quite a few PD simulations to investigate agglomerate formation and breakage. Mishra and Thornton[100] studied the effects of impact velocity, solid fraction, and contact density using a polydisperse spherical agglomerate impacting a wall. Their simulations show that, above a critical impact velocity, dense agglomerates display clear fracture patters, while loose agglomerates disintegrate under the same conditions. Lian, Thornton and Adams[95] conducted PD simulations with two wet agglomerates experiencing collisions. They found the structure of the resultant coalesced agglomerate is highly disordered and depended on the impact velocity.

More recently, the McCarthy group used PD to examine cohesive mixing processes[101, 59, 102]. They found that, depending on the relative importance of various forces acting on particles, cohesion may enhance segregation which is contrary to the traditional thought that cohesion produces a monotonic mitigating effect on segregation.

It is apparent that PD is a powerful tool to explore properties and flows of granular material; however, a significant drawback of PD is that it requires considerable computational resources, therefore limiting the utility of PD to processes with relatively small number of particles. For example, a simulation with 100,000 particles may take months to get results, but an industrial system (e.g., tumbler) could easily contain billions of particles. Therefore, currently PD is still complementary to continuum models and experimentation, for gaining an insight into the physics of granular systems [53].

5.0 COHESIVE CHARACTERIZATION

In this section, we review the related work conducted by our group[1] to demonstrate the successful use of a discrete view in characterizing cohesion in granular flows. Both experimental and computational results are discussed in the context of the impact of the cohesion force (liquid-bridge induced) on the angle of repose, in both "static" and "dynamic" system. We show that, by applying the characterization tools we developed, we could intuitively explain the transition of a granular system from a free-flowing regime to a cohesive regime.

5.1 "STATIC" SYSTEM

Granular Bond Number (Bo_g) refers to the ratio of the maximum capillary force, Fc, to the weight of the particle, Wg, in a monodisperse system:

$$Bo_g = \frac{Fc}{Wg} = \frac{2\pi\gamma R}{\frac{4}{3}\pi R^3 \rho g} = \frac{3\gamma}{2R^2\rho g}, \tag{5.1}$$

where γ is the interstitial fluid's surface tension, R and ρ are radius and density of particle respectively, and g is the acceleration due to gravity.

In general, when material is poured into a pile, a more "flowable" (less cohesive) powder will exhibit a more shallow surface slope and a less "flowable" material, a steeper slope. The quasi-static formation of the angle of repose allows observation of the angle of repose as a function of Bo_g in the absence of (significant) shearing effects. Results from Nase's experiments[47] in a heap show that a marked increase of the angle of repose occurs at roughly $Bo_g \approx 1$ (see Figure 11). Taking a discrete view of particle cohesion allows a

simple, intuitive explanation of this sharp increase: when the particle's self-weight becomes smaller than the interstitial cohesive force, a "static" system ($Bo_g < 1$) becomes "cohesive" ($Bo_g > 1$).

5.2 "DYNAMIC" SYSTEM

In contrast to the "static" case, in a "dynamic" system (e.g., a rotated tumbler) the variation of the dynamic angle of repose shows a much less severe change in the surface angle with increasing Bo_g, and there is no clear transition between the free-flowing and cohesive regimes(see Figure 12, left). This is due to the fact that during flow the shearing force (arising from particle collisions, which are not significant in the static case) play a more important role and vary over the range of experimental parameters. In order to capture this effect, our group developed another characterization tool, the Collision Number, Co, which is given by the ratio of the maximum capillary force to the collisional force[103], F_{Bg}, in a monodisperse system

$$Co = \frac{Fc}{F_{Bg}} = \frac{2\pi R\gamma}{\pi\rho R^4\lambda^2(\frac{du}{dy})^2} = \frac{2\pi\gamma}{\pi\rho R^3\lambda^2(\frac{du}{dy})^2} \tag{5.2}$$

where ρ and R are the density and radius of the particle, respectively, λ^2 is a constant, and du/dy is the shear rate of the flowing region.

One might hypothesize three limits for this number. First, there exists a "slow" flow where the collisional force may be small relative to the particle's self-weight. In this case, $Co \gg Bo_g > 1$ (recall that in a cohesive system $Bo_g \geq 1$). This implies that the impact of the collision force on particle mixing/segregation is negligible, and Bo_g alone is sufficient to characterize the system. This case represents the "static" system. Second, a "fast" flow may occur where the collisional force becomes larger than the particle's weight, so that $Bo_g > Co > 1$. In this case cohesion is dictated primarily by the Co. Third, an "intermediate" flow can be found where the collisional force is comparable to the particle's

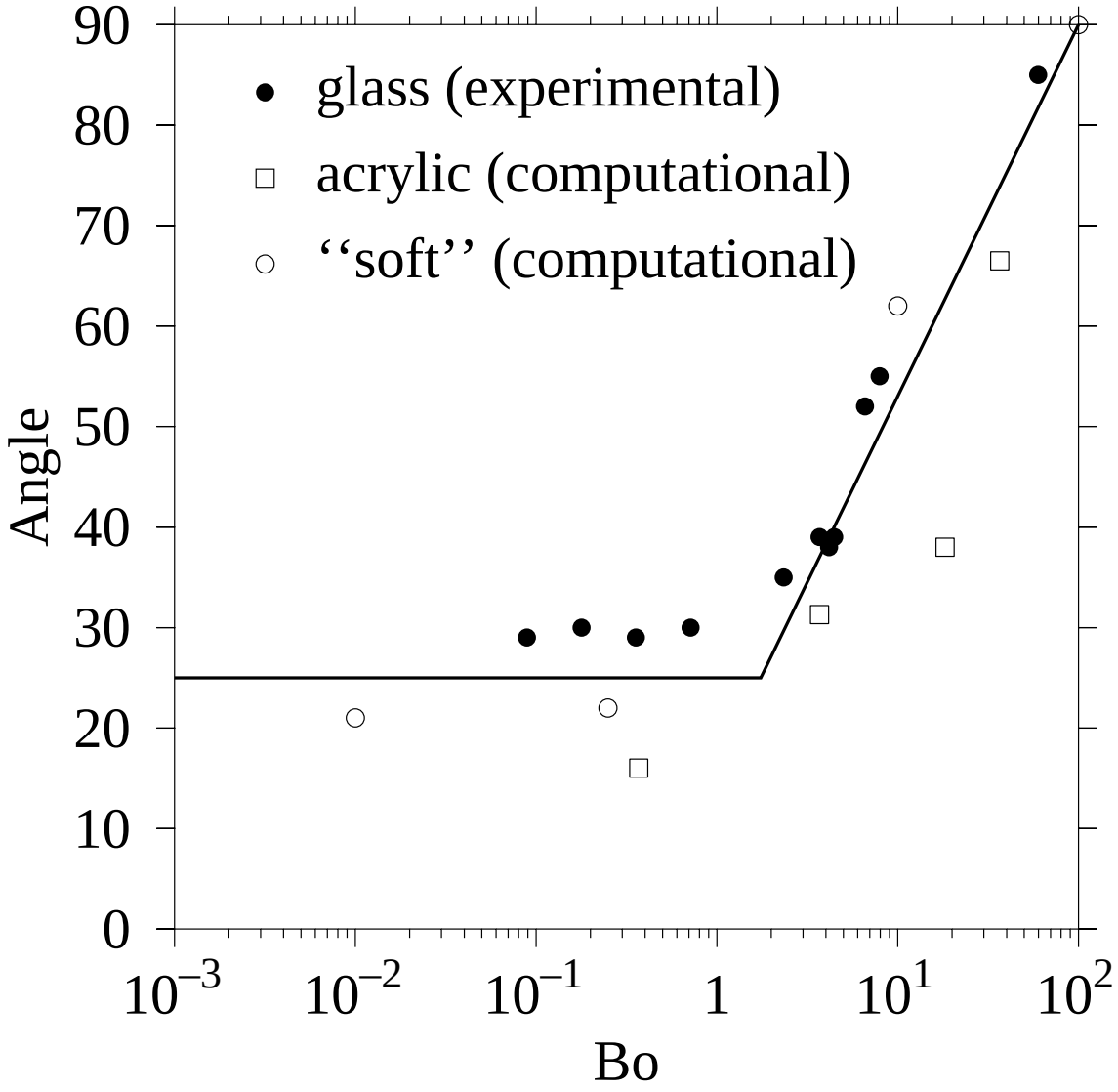

Figure 11: Variation of heaping angle with Bo_g.

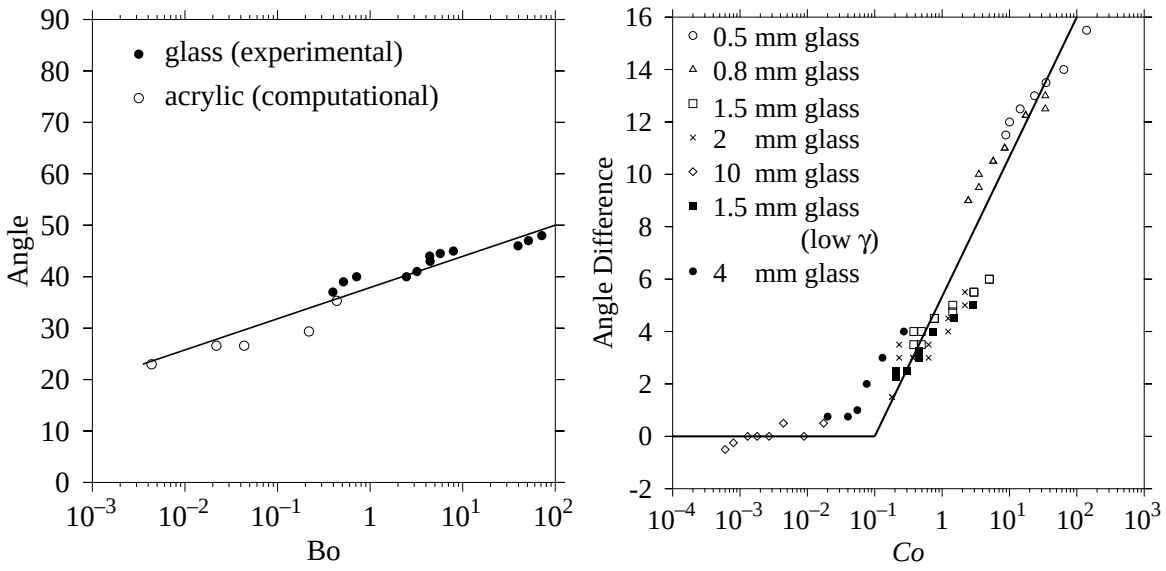

Figure 12: Variation of dynamic surface angle in a tumbler with Bo, (*left*)[1]. Dynamic angle difference as a function of Co, (*right*)[1]

weight, consequently $Co \approx Bo_g > 1$. In this case, both of Bo_g and Co need be taken into consideration.

Experimental and computational results from our group display that the departure of the dynamic angle from that obtained in the cohesionless (dry) case has a marked increase at roughly $Co \approx 1$ (see Figure 12, right)[47]. In other words, the free-flowing/cohesive transition of the system occurs at $Co \approx 1$.

In general, in a system where the shearing forces are negligible, the condition of "$Bo_g > 1$" is sufficient to determine the system as "cohesive"; however if the shearing forces are dominant in a granular flow, the system can be identified as "cohesive" only when Co and Bo_g are both greater than 1.

Traditionally people have long believed that cohesion mitigates segregation[37, 104, 105], however the origin of this phenomenon has been elusive [36, 106]. Despite recent advances in cohesive flow [107, 108, 109, 110, 111, 112, 54, 113], an understanding of the mixing and segregation of cohesive particles is still poor. Our group takes a discrete view of cohesion in granular systems. By reconciling cohesion with its origin (i.e., inter-particle forces), we attempt to develop a microscopic (particle-level), discrete model which is robust to changes in both cohesive behavior and granular micro-structure.

While the ubiquitous sink of granular thermal energy – inelastic collisions – makes meta-stable or non-equilibrium states quite commonplace in particulate systems [114], a continuous input of energy supply can be used to exactly balance the energy lost to inelastic collisions. As a result, the system may eventually reach an asymptotic state, where the reversible process between mixing and segregation cancels and the particle distribution is essentially invariant. It is the asymptotic state which is of interest in this work.

Unlike mixing miscible liquids or mixing a soluble solid into a liquid, a longer mixing operation doesn't necessarily get a better mixing extent as desired. In other words, there exists a intermediate state where the mixing result is the best. After that the mixing is actually lessened till the asymptotic state is reached, i.e., over mixing occurs[27] (see Figure 13). How to predict the optimal mixing and stop the operation at the right time has long been the subject of much empirical work[28]. It is one of our goals to achieve a similar mixing extent not by stopping at some intermediate state, but instead by manipulating the asymptotic state. (see Figure 13).

In our discrete-based model, we hypothesize that the relative importance of the various forces acting on pairs of particles can be used to determine the behavior of the system at its asymptotic state. Furthermore, we believe that by examining the relative magnitude of the cohesion force (here liquid-bridge induced) when compared to other relevant forces, we can quantify and elucidate the impact of the cohesion force on the asymptotic state of system. In this work, our group focuses on a fixed volume (percent) of interstitial liquid and differing particle properties. As will be discussed, our particle flow is sufficiently gentle as to be located within the "mixing" phase of Geromichalos [58], although a variety of mixing/segregation behavior is observed as particle properties are varied.

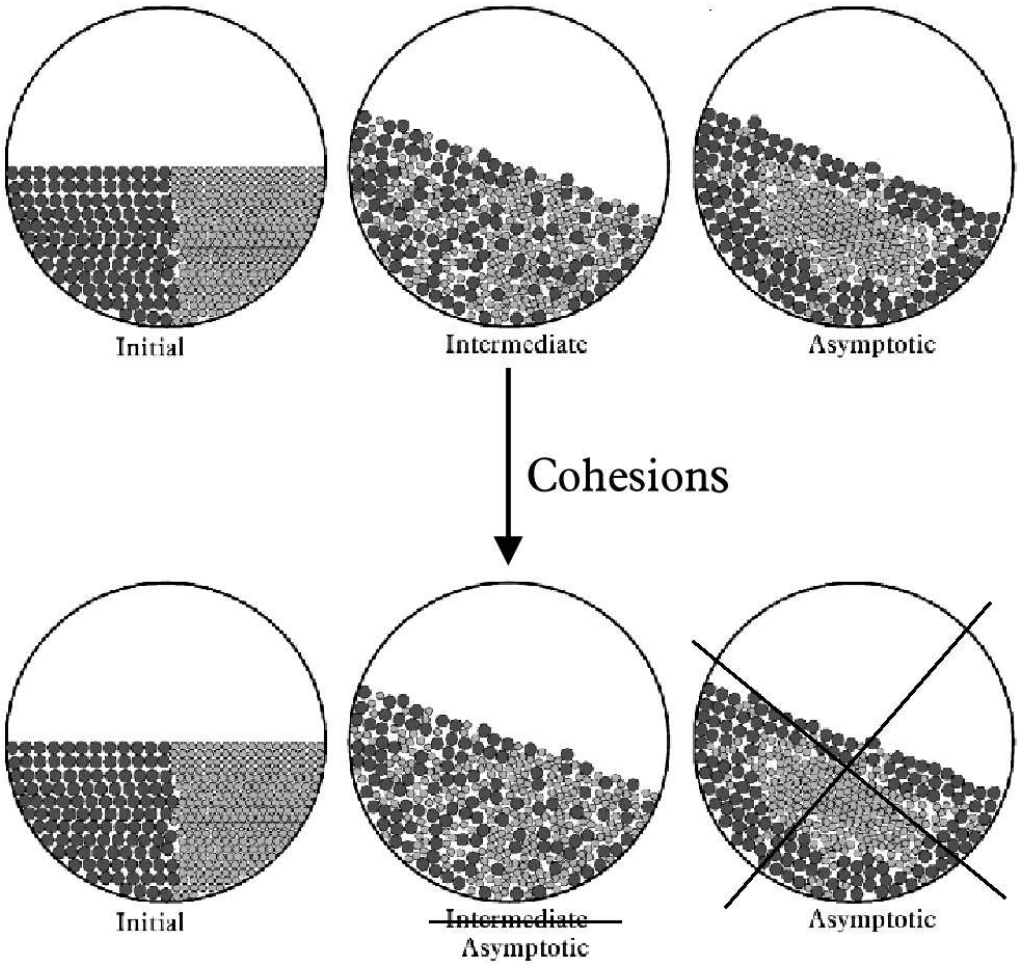

Figure 13: "Over mixing" may be mitigated by cohesions.

6.0 COHESIVE MIXING IN "STATIC" SYSTEMS

In this section, in order to use the Granular Bond Number to examine the impact of cohesion on particle mixing/segregation, we extend the argument about our characterization tool, Bo_g, for a homogeneous system to binary systems. In particular, we allow variation in particles sizes, densities and/or wetting characteristics (Figure 14).

6.1 BO_G IN BINARY COHESIVE SYSTEM

In interpreting the Bond Number, it is clear that the rationale for defining a material as "cohesive" is that one particle within a two particle grouping may be thought of as a "guest" particle (obviously, the less massive of the two) and "stick" to the other particle (i.e., consider sand sticking to a bowling ball). Thinking of the Bo_g in this way suggests that we re-define the Bo_g as

$$Bo_g = \frac{2\pi\gamma R_e(cos\theta)_{min}}{\frac{4}{3}\pi g\ (R^3\rho)_{min}} = \frac{3\gamma R_e(cos\theta)_{min}}{2g\ (R^3\rho)_{min}}, \tag{6.1}$$

where γ is the interstitial fluid's surface tension, $(R^3\rho)_{min}$ is the smaller of the two masses and is used to represent the fact that the less massive particle's motion will be dominated by the more massive particle, θ is the wetting angle, R_e is the geometric mean radius ($R_e = 2R_1R_2/(R_1+R_2)$), and differing wetting characteristics are incorporated simply by using the larger value of θ (or the smaller value of $cos\theta$)[115].

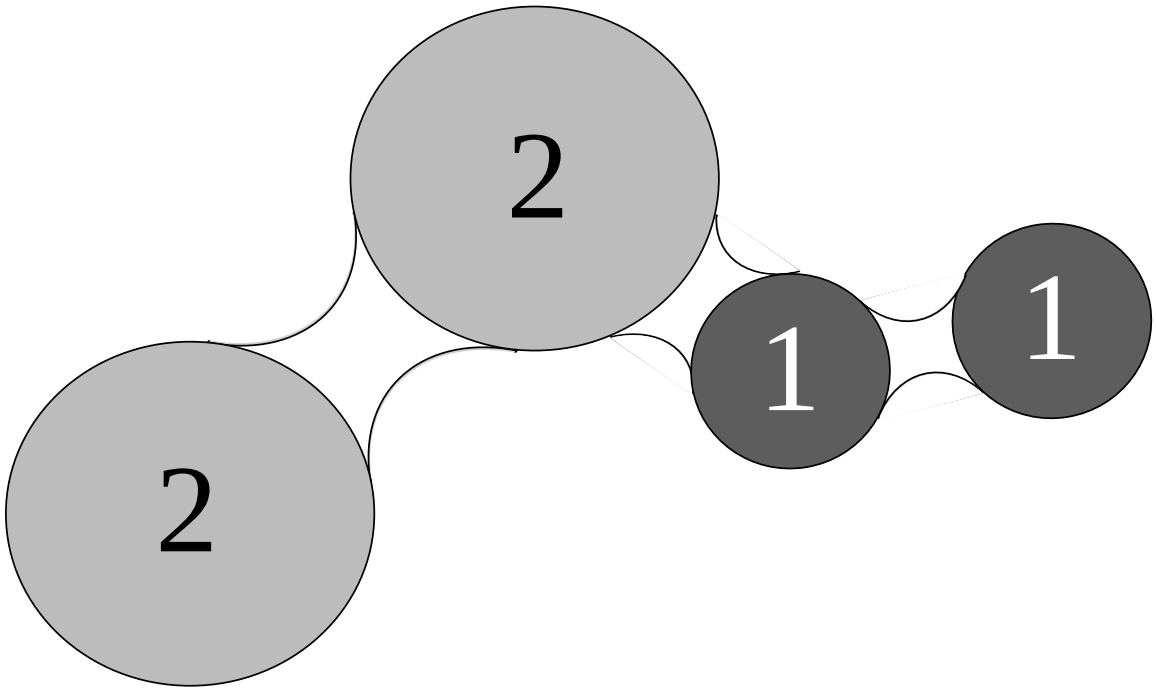

Figure 14: Schematic demonstration of the possible interactions between particles in a binary cohesive system.

6.2 PHASE DIAGRAM

The values of the Bo_g for each potential pair of particles, i and j, within the system (i.e., for a binary system, the $Bo_{g_{11}}$, $Bo_{g_{22}}$, and $Bo_{g_{12}}$, where 2 is defined as the larger of the particles) need to then be compared. It should be noted that this approach necessarily limits our applicable range of size ratios for two reasons. First, as the size ratio becomes (infinitely) small, maintaining the bed in the pendular regime will become impossible and two particle interactions will become meaningless. Secondly, directly comparing pairwise particle interactions neglects both multi-particle interactions as well as the reality that for small size ratios the probability of the three types of pairwise interactions may be very different (so some scaled comparison would be warranted). Nevertheless, as can be seen in Section 6.4, this simple approach works well even down to size ratios of 0.25 (i.e., interaction probability ratios of 16 to 1).

Comparing the magnitudes of these $Bo_{g_{ij}}$ leads to two dimensionless groups

$$\Re_1 = \frac{Bo_{g_{11}}}{Bo_{g_{12}}} = \frac{R_1 + R_2}{2R_2} \quad \frac{cos\theta_1}{(cos\theta_1, cos\theta_2)_{min}} \frac{(R_1^3\rho_1, R_2^3\rho_2)_{min}}{R_1^3\rho_1} \tag{6.2}$$

$$\Re_2 = \frac{Bo_{g_{22}}}{Bo_{g_{12}}} = \frac{R_1 + R_2}{2R_1} \frac{cos\theta_2}{(cos\theta_1, cos\theta_2)_{min}} \frac{(R_1^3\rho_1, R_2^3\rho_2)_{min}}{R_2^3\rho_2}, \tag{6.3}$$

which can be re-written by defining $\alpha = \rho_1/\rho_2$, $\beta = R_1/R_2$, and $\lambda = \cos\theta_1/\cos\theta_2$, yielding

$$\Re_1 = \frac{Bo_{g_{11}}}{Bo_{g_{12}}} = \frac{\beta + 1}{2} \quad \frac{\lambda}{(\lambda, 1)_{min}} \frac{(\alpha\beta^3, 1)_{min}}{\alpha\beta^3} \tag{6.4}$$

$$\Re_2 = \frac{Bo_{g_{22}}}{Bo_{g_{12}}} = \frac{\beta + 1}{2\beta} \frac{1}{(\lambda, 1)_{min}} \frac{(\alpha\beta^3, 1)_{min}}{1}. \tag{6.5}$$

In order to determine the mixing behavior we can then *analytically* determine the locations of the phase boundaries of our mixing/segregation diagram by identifying where in the parameter space of size ratio (β), density ratio (α), and wetting angle ratio (λ) differing hierarchies of $Bo_{g_{ij}}$ are observed.

The following cases may be observed

If $\alpha\beta^3 > 1$

$$\begin{aligned} 1 < \Re_1, 1 < \Re_2 \qquad & \lambda > \tfrac{2\alpha\beta^3}{1+\beta} \\ \Re_1 < 1 < \Re_2 \qquad & \lambda < \tfrac{2\alpha\beta^3}{1+\beta} \end{aligned} \tag{6.6}$$

If $\alpha\beta^3 < 1$

$$\begin{aligned} \Re_1 < 1, \Re_2 < 1 \qquad & \tfrac{(\beta^3+\beta^2)\alpha}{2} < \lambda < \tfrac{2}{1+\beta} \\ \Re_1 < 1 < \Re_2 \qquad & \lambda < \tfrac{(\beta^3+\beta^2)\alpha}{2} \\ \Re_2 < 1 < \Re_1 \qquad & \lambda > \tfrac{2}{1+\beta} \end{aligned} \tag{6.7}$$

In the case of $\alpha\beta^3 > 1$ (i.e., the smaller particle is more massive than the larger particle), $\Re_2 > 1$ is always true for any combination of particle properties (i.e., size, density and/or surface characteristics). This implies that the interaction of the two dissimilar particles (i.e., the "mixing" interaction) is always less significant than the interaction of the two largest particles (see Figure 14). In fact, for some values of λ, the dissimilar particles interaction is the least significant of the three possible interactions. We expect that this region of parameter space will therefore always favor segregation as larger particles cluster together and exclude smaller ones. This suggests that cohesion here will lead to a novel mechanism of segregation and ultimately *more* segregation than would be achieved in the dry case.

In contrast, in the case of $\alpha\beta^3 < 1$ (i.e., the small particle is less massive), when $\alpha(\beta^3 + \beta^2)/2 < \lambda < 2/(1 + \beta)$, both $\Re_1$ and $\Re_2$ are less than 1. This indicates that the interaction between dissimilar particles is the most significant, therefore favoring intimate particle mixing. Systems that lie in this region of parameter space are expected to be more mixed than the corresponding dry experiment. For other values of λ, however, $\Re_2 > 1$ or $\Re_1 > 1$, so that in this region as well, we expect some instances of cohesion-enhanced segregation.

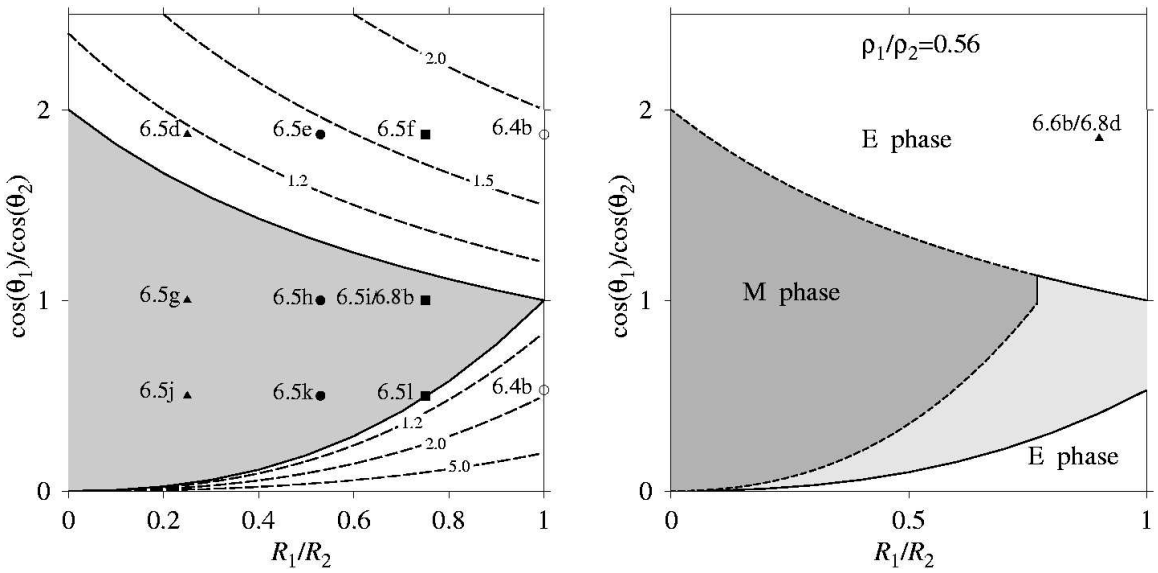

— Phase diagrams are a function of the ratios of sizes, densities, and values of the cosine of the wetting angles. (**Left**) Phase diagram for the systems with $\rho_1/\rho_2 = 1$. Solid lines depict phase boundaries, while dashed lines show contours of the larger $\Re_i$ values. (**Right**) The size of the M phase for a density ratio of 0.56 grows, and the phase boundary is shown as a solid line; while that of the inverse case (density ratio of 1.78) shrinks, the phase boundary is shown as a dashed line, i.e., the lighter gray region becomes part of the E phase.—

Figure 15: Phase diagrams for binary cohesive systems.

It is instructive at this point to examine in detail why hierarchies of properly scaled cohesive force (i.e., Bo_g) are used as opposed to simply comparing that of the unscaled value, Fc. Consider particles of the same density and surface properties, but differing diameters. Clearly, the largest unscaled cohesive force will be found to exist between two larger particles ($F_c \propto R_e$). Nevertheless, the particle sizes may be chosen in such a way that $Bo_{g_{22}} < 1 < Bo_{g_{12}}$. In this case, despite the fact that the unscaled cohesive force is strongest between the two large particles (i.e., $Fc_{22} > Fc_{12}$), the larger particles will not adhere to each other, yet the smaller ones will adhere to the larger ones (a simple physical example might be sand sticking to a bowling ball)[18]. In fact, under these conditions – particles differing only in size – it is easily shown that the mixing interaction is always most significant (largest Bo_g) despite the fact that the unscaled Fc values may lead one to think otherwise.

The implications of combining equations 6.6 and 6-7 are best visualized by phase diagrams, which outline regions of mitigated (M phase) and enhanced (E phase) segregation for particle mixing/segregation. The definitions of these phases are based on the values of $\Re_1$ and $\Re_2$, as discussed above; that is, values of $\Re_i$ greater than 1 lead to segregation. Figure 15 shows the phase diagrams for the case of $\alpha = 1$ (left), $\alpha = 0.56$ (right with both light and dark gray M phase), and $\alpha = 1.78$ (right with only dark gray M phase). In both plots, the white region corresponds to the E phase where $\Re_i > 1$ for either i =1, 2 or both, while the gray region corresponds to the M where both $\Re_i$ values are less than 1. From the rightmost plot it is clear that, in general, varying the density ratio causes a relative change in the size of the M and E phases – the M phase grows when the smaller particle is less dense and shrinks when it is more dense. Finally, in anticipation of using the model for quantitative analysis of the extent of segregation, the leftmost plot in Figure 15 shows dashed lines corresponding to various values of $\Re_i > 1$. It should be noted that on the far right axis (where the size ratio is equal to 1), the value of $\Re_i$ for λ is equal to that of $1/\lambda$, as the identity of particle 2 (the larger one) is not defined.

It should be noted here that M and E phases in the diagrams only locate the cohesive systems where the particles will evolve into a **more** mixed or segregated configuration as compared to the dry case, but not necessarily absolute values of mixing/segregation. In other words, for any given system where the particles segregate in the dry case, with these phase

diagrams we could predict whether the particles in this system will be **more** segregated or **less** after the introduction of liquid-bridging induced cohesion force.

6.3 EXPERIMENT SETUP

As a simple way to obtain an unquenched, asymptotic granular state, we choose a pseudo-two-dimensional tumbler mixer, because of its industrial prevalence and a long history of academic study[116, 117, 118, 119, 120, 121, 122, 123] (see Figure 16). The tumbler is around 14cm in diameter and 2cm in depth, and treated with a hydrophobic silane to reduce adhesion of particles to the surfaces. Binary mixtures of spherical particles, glass or acrylic, fill half of the tumbler (specifically, 75ml of one size of beads and 75ml of the other size of beads). Because the half-filled container is circular in cross section and operated in the rolling regime, the particles trace out regular, closed streamlines as they flow. During the rotation, the bulk of the bed undergoes a solid-body rotation by following the cylinder motion. Near the surface, the particles flow downward along the surface in a thin layer continuously (i.e., without avalanches) until they enter the bed again, and the process repeats[124, 125]. Since the particles undergo multiple passes through this layer, the bulk of the bed essentially stores the particle positions until their next pass through the layer. In this way, we can explore the interplay between mixing/segregation and cohesion[18]. Under these conditions, mixing occurs almost solely due to collision-induced diffusion in the thin surface layer[126]. After many revolutions, the particle distribution in the bed remains time invariant and the system is assumed to reach its asymptotic state.

Experimentally, if we rotate a tumbler with sufficiently small speed (typically 6-9 rpm) such that the forces of interest include only the cohesive interaction (Fc) and the particle's weight (Wg), we obtain a condition where $Co >> 1$, — i.e., shearing forces are negligible, so that we are in a Bo_g dominated flow.

Before each experiment, all of the glass beads are soaked in a dilute HF solution both to clean the surfaces as well as to produce approximately uniform surface roughnesses. Subsequently half of the beads are further treated with a surface-modifying hydrophilic silane

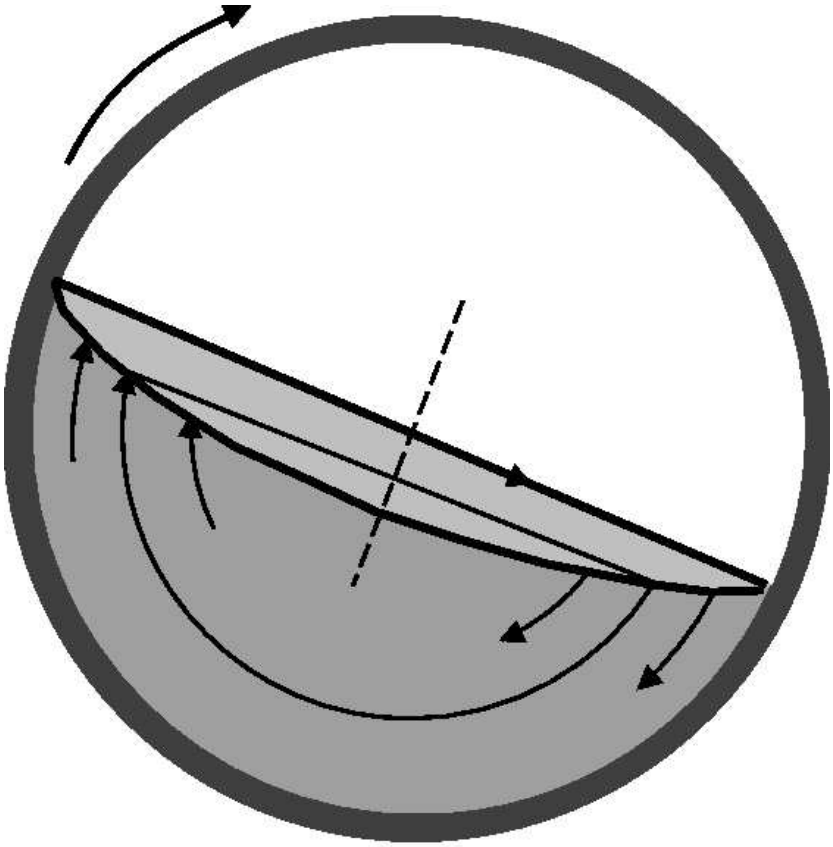

Figure 16: A schematic plot of a rotating tumbler.

(and a trace amount of fluorescent green silane), and the other half with a hydrophobic silane (and a trace amount of fluorescent red/orange silane). The resulting particles have wetting angles of $\theta \approx 20^\circ$ and $\theta \approx 60^\circ$.

Experimentally, the particles are initially completely segregated, with component i being contained in the lower left quarter of the tumbler and component j in the lower right quarter. After approximately 30 revolutions the particle distribution becomes time invariant and is assumed to represent the asymptotic state of the system. We conduct the dry experiment first, then repeat the experiment with the addition of a very small amount of water ($\approx$1% water by volume). The digitized images of the particle distribution at both initial and asymptotic states are taken for later comparison and image processing to obtain qualitative and quantitative information. The effect of the cohesion force can be elucidated with an examination of the difference in the pictures at asymptotic states between the dry and wet case. Experimentally we restrict the rotation speed such that it is sufficiently small ($6 \sim 9\ rpm$) to assure the system is in the rolling regime and that the cohesion is primarily dictated by the Granular Bond Number (Bo_g).

6.4 RESULT AND DISCUSSION

6.4.1 Qualitative analysis

In general, segregation by density will force the less dense particles to the periphery and the more dense particles to the inner core, while segregation by size will promote larger particles migrating to the periphery and smaller particles to the inner core [36]. In all experiments, all the dry systems will end up with the particles segregated but with differing segregation distribution with the exception of experiment 6.4a (Table 1) where the particles are mechanically identical, but have different wetting angles so that they are perfectly mixed at the asymptotic state, when dry.

As discussed in detail below, the results from the wet experiments show a dramatic change of particle distribution (i.e., mixing/segregation) relative to that of the dry cases.

Table 1: List of experiments conducted in "static" systems.

Exp.	R_1 (mm)	R_2 (mm)	ρ_1 (g/cm^3)	ρ_2 (g/cm^3)	θ_1	θ_2	*Phase*
6.4a	0.4	0.4	2.5[1]	2.5			dry
6.4b	0.4	0.4	2.5	2.5	20°	60°	E
6.5a	0.25	1.0	2.5	2.5			dry
6.5d	0.25	1.0	2.5	2.5	20°	60°	E
6.5g	0.25	1.0	2.5	2.5	20°	20°	M
6.5j	0.25	1.0	2.5	2.5	60°	20°	M
6.5b	0.4	0.75	2.5	2.5			dry
6.5e	0.4	0.75	2.5	2.5	20°	60°	E
6.5h	0.4	0.75	2.5	2.5	20°	20°	M
6.5k	0.4	0.75	2.5	2.5	60°	20°	M
6.5c/6.8a	0.75	1.0	2.5	2.5			dry
6.5f	0.75	1.0	2.5	2.5	20°	60°	E
6.5i/6.8b	0.75	1.0	2.5	2.5	20°	20°	M
6.5l	0.75	1.0	2.5	2.5	60°	20°	M
6.6a	0.9	1.0	1.4[2]	2.5			dry
6.6b	0.9	1.0	1.4	2.5	50°	70°	E
6.8c	0.9	1.0	1.4	2.5			dry
6.8d	0.9	1.0	1.4	2.5	20°	60°	E

Each change is both qualitatively and quantitatively in agreement with the predictions of our model.

6.4.1.1 Varying wetting angles The particles in system 6.4b ($\alpha = 1$, $\beta = 1$, $\lambda = 1.88$ or 0.53) have the same size and density but different wetting angles (see Table 1, experiment 6.4b) so that it represents the E phase (point(s) 6.4b in Figure 15; note that the "larger" particle is undefined in this case). While the particles are perfectly mixed in the dry case (Figure 6.4(a)), our model predicts that adding water will make the particles segregate. Figure 6.4(b) (wet case) shows that there are more bright beads (here, hydrophobic) clustered in the center of the tumbler. This can be easily understood in this way: since the weights of both types of particles are the same, the smaller wetting angle between hydrophilic beads (here, dark) yields a larger cohesion force, and thus a bigger Granular Bond Number (Bo_g). The hydrophilic particles (dark) then preferentially cluster together and migrate toward the outside.

6.4.1.2 Varying wetting angles and size ratios We next conduct three sets of experiments with varying particle size ratio in addition to the wetting angle (Figure 6.5). One set of experiments is with glass beads of 0.25 mm (radius) along with 1.0mm – i.e., the size ratio is 0.25 (Table 1, experiments 6.5a, 6.5d, 6.5g, 6.5j; Figure 15). The second set of experiments is with glass beads of 0.4 mm along with 0.75 mm – i.e., the size ratio is 0.53 (Table 1, experiment 6.5b, 6.5e, 6.5h, 6.5k; Figure 15). The last set of experiments is with glass beads of 0.75 mm along with 1.0 mm – i.e., the size ratio is 0.75 (Table 1, experiment 6.5c, 6.5f, 6.5i, 6.5l; Figure 15).

It is obvious that, for all three size ratios, the dry case leads to strong radial segregation due to size differences (Figure 6.5(a), 6.5(b) and 6.5(c)). The smaller particles stay at the center (dark) areas while the larger ones remain at the periphery. When the small particle is more hydrophilic (here, bright), the systems represent the E phase (point 6.5d, 6.5e and 6.5f in Figure 15). We therefore expect that the segregation achieved in the dry cases will be enhanced (or remain strong) by adding water. While Figure 6.5(d), 6.5(e) and 6.5(f) confirm our prediction, the macroscopic segregation patterns are beyond our expectation,

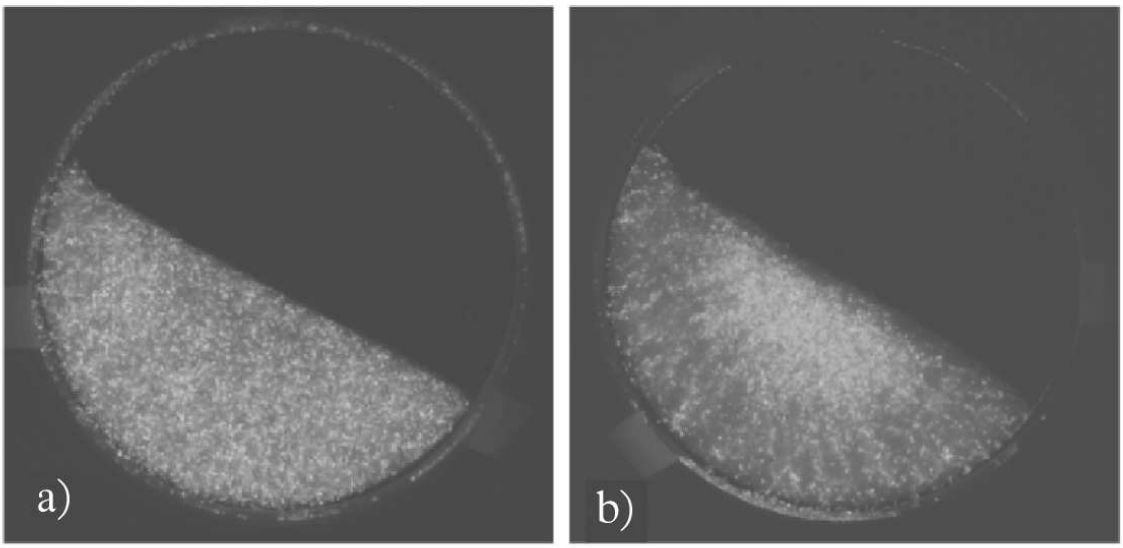

— (a) Particles with differing surface properties (dark-hydrophilic and bright-hydrophobic) but otherwise identical in all other respects (Figure 6.2, point(s) 6.4b) will mix perfectly when tumbled dry; however, (b) when interstitial water is added, they will instead segregate.—

Figure 17: Varying Wetting Angles.

but may be related to the time-varying surface angle resulting from the difference in cohesion between the two materials [127]. When the particles have almost identical wetting angles, the systems represent the M phase (point 6.5g, 6.5h and 6.5i, Figure 15). Figure 6.5(g), 6.5(h) and 6.5(i) show the core (dark) areas in all experiments shrink after adding water, i.e., particles mix more than in the dry cases, as expected. Finally, when the larger particles are more hydrophilic (point 6.5j, 6.5k and 6.5l in Figure 15), the 0.25 and 0.53 cases remain firmly in the M phase and mix more than in the dry case (i.e., core (dark) area shrinks), however, since the 0.75 case lies near the phase boundary, the experiment is essentially unaffected by cohesion (see Figure 6.5(j), 6.5(k) and 6.5(l))[59].

6.4.1.3 Varying density ratio, size ratio and wetting angles

Finally, we vary the density ratio, size ratio, and wetting characteristics at the same time. Figure 5 shows the results for the case α =0.56, β =0.9, and λ =1.88 (i.e., point 6.6b in Figure 2). The asymptotic distribution for dry particles represents only mild radial segregation as the density and size effects compete and almost cancel each other (see Figure 6.6(a)). In the wet case, however, the same initial condition instead evolves to a more segregated state as predicted[18] (Figure 6.6(b)).

6.4.2 Quantitative analysis

Quantitatively, we process the digitized images of the asymptotic state from both the dry and wet cases to extract concentration maps. In the digitized images each pixel is identified as its own RGB value that represents the degree of red, green and blue. The processing of the RGB images involves first transforming the image from the RGB color space into HSI color space. The transformation used for calculating the HSI values follows the procedure described by Peterson *et al.*[128]. The HSI representation of the RGB color space is obtained through the transformation

$$\mathbf{H} = \quad cos^{-1}\left|\frac{0.5[(R-G)+(R-B)]}{[(R-G)^2+(R-B)(G-B)]^{1/2}}\right| \tag{6.8}$$

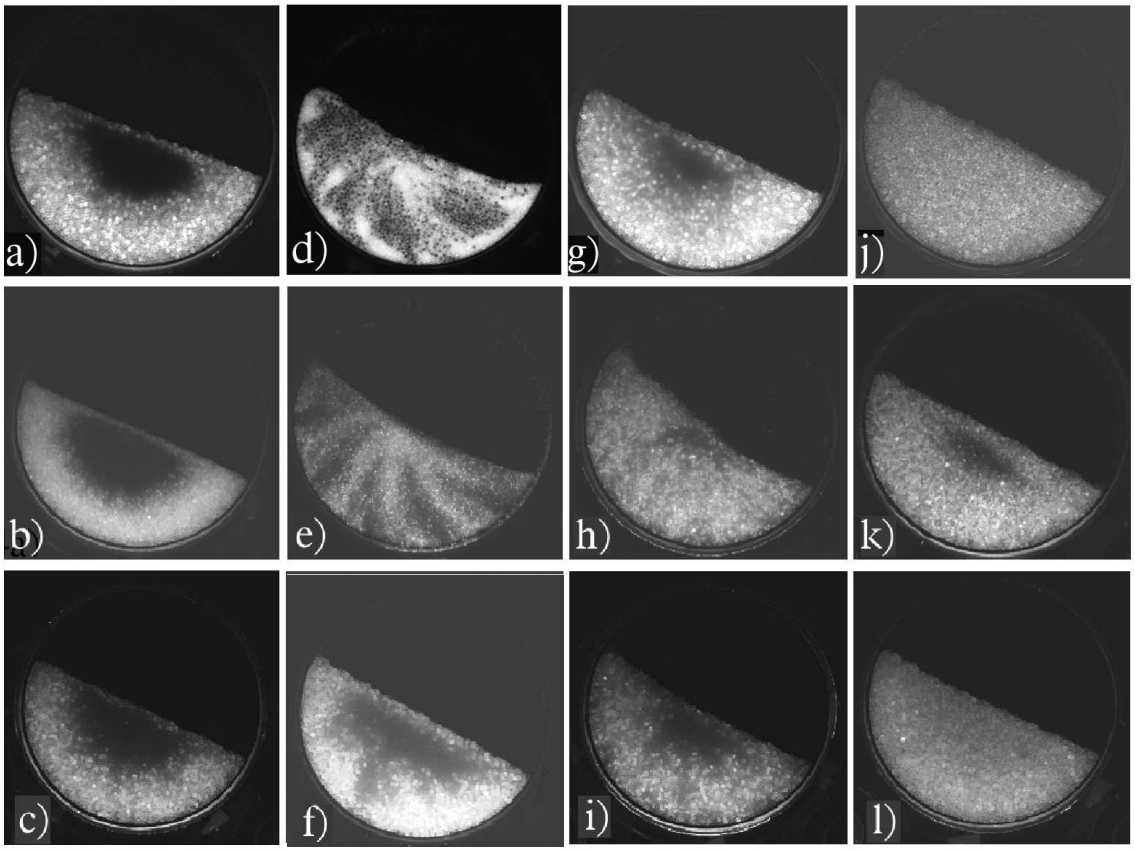

— From top to bottom the rows correspond to size ratios of 0.25, 0.53 and 0.75, respectively. From left to right the images represent results when dry – (a), (b) and (c); wet with the smaller particle (bright) being more hydrophilic – (d), (e), and (f); wet with both particles hydrophilic – (g), (h) and (i); and wet with the smaller particle (dark) being more hydrophobic – (j), (k) and (l). Results are in agreement with the predictions from theory (Figure 6.2). —

Figure 18: Varying Size Ratio and Wetting Angle.

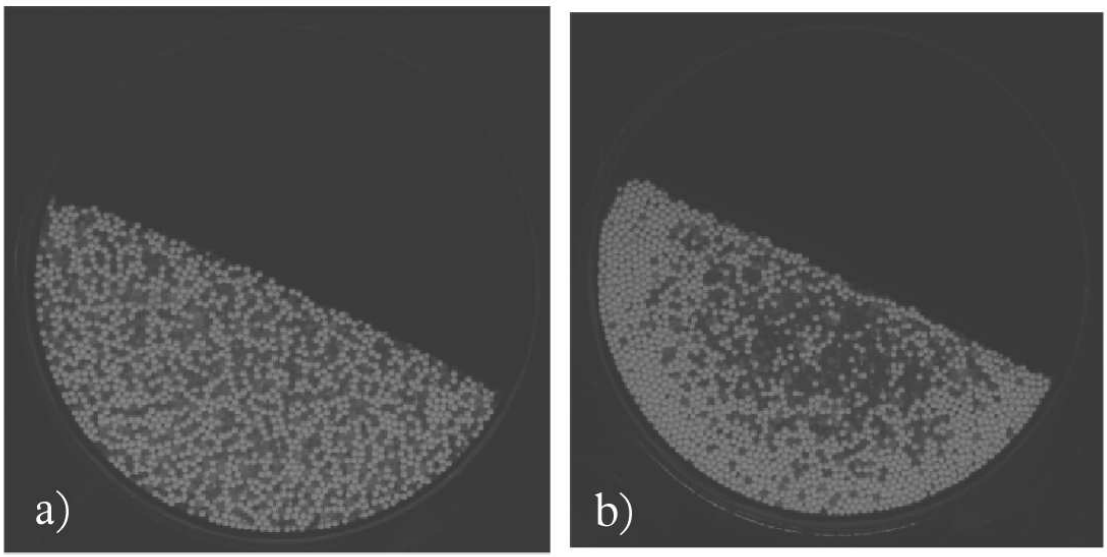

— When particles of size ratio 0.9 and wetting angle ratio 0.56 (Figure 6.2, point 6.6b) are tumbled: (a) dry, they will segregate radially only slightly; (b) add water and they segregate more significantly. —

Figure 19: Varying Density Ratios.

$$\mathbf{S} = \quad 1 - \frac{3}{(R+G+B)} min(R,G,B) \tag{6.9}$$

$$\mathbf{I} = \quad \frac{(R+G+B)}{3} \tag{6.10}$$

where the R, G, B values come from the digitized image. Equation 6.8 gives a value of hue in the range 0 to 180 degrees. When the ratio B/I $\geq$ G/I then H was set to H=360-H. $min(R,G,B)$ corresponds to the minimum of the three values of R, G, and B [129]. A threshold value of red to green intensity is determined from the known volume ratio and positions of the initial condition. The images are then segmented so that mixing measurement calculations may be performed. A mixing measure (IS), essentially the standard deviation of the concentration, is calculated from multiple spot concentration measurements as

$$IS = \sqrt{\frac{\sum_{i=1}^{N}(C - C_{avg})^2}{N-1}} \tag{6.11}$$

where N is the number of useful cells, C is the concentration of red or green pixels in a designated cell, and C_{avg} is the average concentration of red or green pixels in the entire image. Table 2 and 3 lists all the IS values for the experiments conducted, as well as the percentage change from the corresponding dry cases, which are calculated as

$$change\% = \frac{IS_{dry} - IS_{wet}}{IS_{dry}} \times 100\% \tag{6.12}$$

A positive change means the system is more mixed than in the dry case while a negative change means more segregated.

As is evident from the development of the phase diagrams, the *maximum* value of $\Re_i$ is the critical value for the case of cohesion-enhanced segregation (i.e., where one of $\Re_i$ >1). By analogy, one might argue that the critical value for cohesion-enhanced mixing is that of the *minimum* $\Re_i$. In Figure 6.7, we show both values of $\Re_i$, but highlight the expected critical value as a solid symbol. If one were to follow the critical values, we would obtain a rotated sigmoidal dependency, whereas tracking the average value would yield roughly a linear dependence. Our theory would predict that all experiments should lie in either the upper left or lower right quadrants (as our critical values do).

Table 2: Quantitative analysis of the experimental results (1).

	Dry case	**Wet case**	**Wet case**	**Wet case**
	6.4a			6.4b(s)
$\Re_1$				1.9 (1)
$\Re_2$				1 (1.9)
IS	0.16			0.24
IS change %				-54%
	6.5a	6.5d	6.5g	6.5j
$\Re_1$		1.2	0.63	0.63
$\Re_2$		0.04	0.04	0.07
IS	0.356	0.361	0.25	0.26
IS change %		-1.5%	29%	27%
	6.5b	6.5e	6.5h	6.5k
$\Re_1$		1.4	0.77	0.77
$\Re_2$		0.22	0.22	0.41
IS	0.37	0.39	0.21	0.31
IS change %		-5.8%	44%	18%
	6.5c	6.5f	6.5i	6.5l
$\Re_1$		1.6	0.88	0.88
$\Re_2$		0.49	0.49	0.93
IS	0.39	0.41	0.30	0.37
IS change %		-5.9%	24%	4.6%

Table 3: Quantitative analysis of the experimental results (2).

	Dry case	**Wet case**	**Wet case**	**Wet case**
	6.6a	6.6b		
$\Re_1$		1.8		
$\Re_2$		0.43		
IS	0.27	0.35		
IS change %		-29%		
	6.8a		6.8b	
$\Re_1$			0.88	
$\Re_2$			0.49	
IS	0.39		0.30	
IS change %			23%	
	6.8c	6.8d		
$\Re_1$		1.8		
$\Re_2$		0.43		
IS	0.25	0.33		
IS change %		-29%		

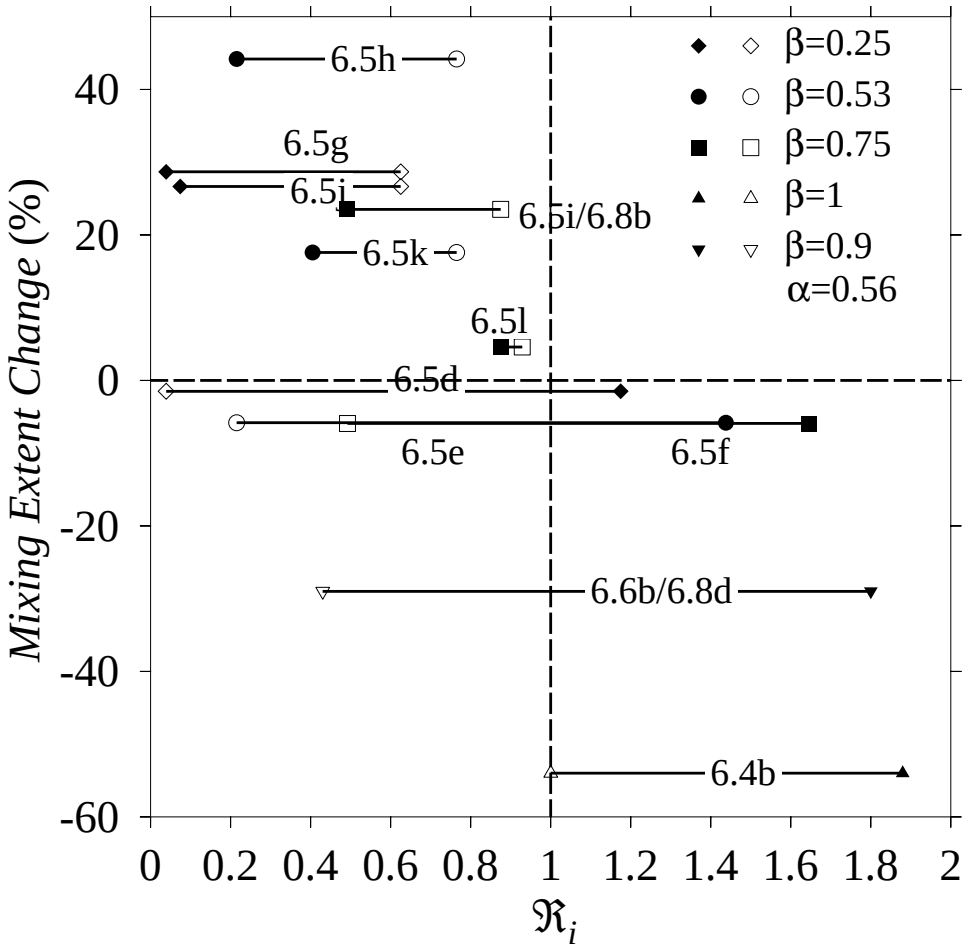

— The change in the extent of mixing is expected to be positive for values of $\Re_i$ <1 and negative for $\Re_i$ >1. Here we plot the values of the extent change and $\Re_i$ for experiments in Figures 6.4, 6.5, and 6.6. —

Figure 20: Mixing extent variation of pseudo-static cohesive systems.

6.5 PARTICLE DYNAMICS SIMULATIONS

To further test our theory, Particle Dynamics simulations are performed. As discussed in the Section 4, Particle Dynamics captures the bulk flow of the material via simultaneous integration of the interaction forces between individual pairs of particles, and the particle trajectories are obtained via explicit solution of Newton's equation of motion for every particle[85]. While the forces in the system typically include only a contact force (normal repulsion), tangential friction and gravity, additional particle interaction forces (e.g., capillary force and van der Waals force, etc.) can be easily added. In this work, the collisional forces are modeled after the work of Hertz and Mindlin [91].

The cohesive forces, which arise from liquid bridging, are modeled after the work of Lian and Thornton [94, 95, 130] and discussed in detail in Section 4.3. In the simulation, the bed is a 3D bed with a periodic depth of 4 or 5 particle diameters, and a frictional circular wall. Each particle can have as many liquid bridges as the coordination number. When one particle comes into contact with another, a steady pendular liquid bridge of a given volume is immediately formed at the contact point. The liquid content of each bridge is assumed to be a constant, here taken as 0.1% of the volume of the largest particle. If one particle comes into contact with another, initially both forces due to contact interactions and cohesive interactions act on the particles; however upon initial separation, a liquid bridge remains (as do the capillary force and the viscous force) until a critical separation distance is exceeded at which time the liquid bridge ruptures and the cohesive interaction disappears immediately.

Two sets of simulations are conducted to test our theory. One set of simulations (experiment 6.8a and 6.8b) is conducted using a computational analogue of the experiment 6.5c and 6.5i, – i.e., the glass beads of 0.75 mm (radius) along with 1.0mm (Table 1). As in the experiment 6.5c (Figure 6.5(c)), the particles segregate strongly when dry (Figure 6.8(a)), yet become more mixed when wet (Figure 6.8(b); point 6.8b in Figure 15).

The other set of simulations (experiment 6.8c and 6.8d, Table 1) is conducted with the smaller particle being less dense ($\alpha = 0.56$), and more hydrophilic ($\theta \approx 20^o$ versus $\theta \approx 60^o$). Here we chose slightly different absolute values of the wetting angles that nevertheless yield

essentially the same wetting angle ratio as the experiment 6.6*b* (see Table 1). As before, the asymptotic distribution for free-flowing (dry) particles represents only mild segregation (Figure 6.8(c)), while the addition of interstitial moisture (Figure 6.8(d)) again causes the particles to become more segregated, as predicted.

It should be pointed out that the method of IS calculation differs between the computations (which can probe the full three dimensional flow) and the optical technique used for experiments (which is limited to surface/wall measurements). Nevertheless, there is a surprising degree of agreement between the simulated IS percentage changes between Figures 6.8 and 6.5/6.6 (see Table 2 and 3).

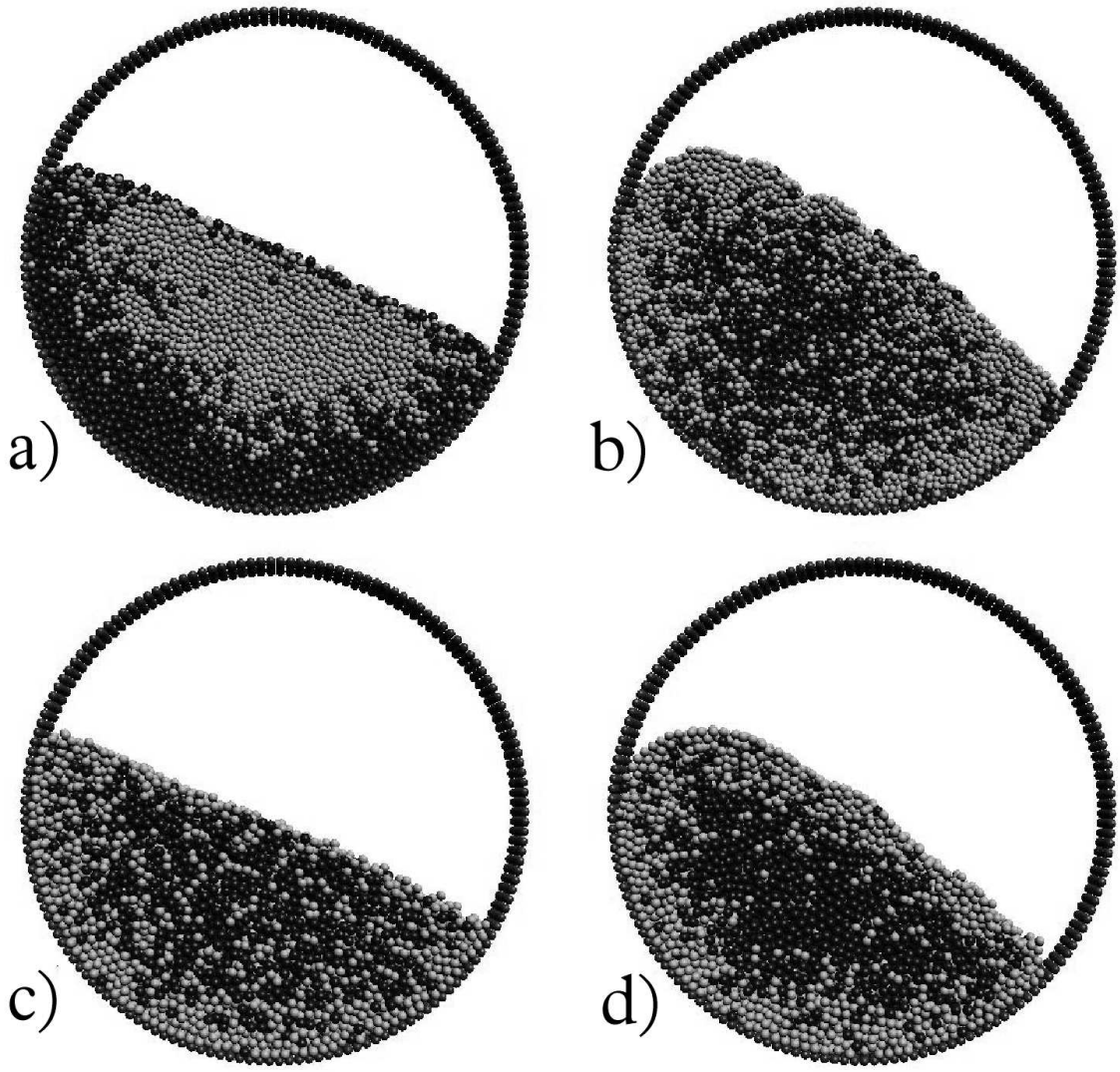

— (a) Dry and (b) wet mixing results for varying particle size only (corresponds to a computational equivalent of Figure 6.5c and 6.5i, respectively). (c) Dry and (d) wet mixing results for varying size, density, and wetting angle (roughly equivalent to Figure 6.6a and 6.6b, respectively). —

Figure 21: Results from PD simulation.

7.0 COHESIVE MIXING UNDER SHEAR

In a non-cohesive shearing flow, large particles are found to migrate to and stay on the top section of a device while small ones fall down to the bottom section[5, 6] (see Figure 22). Several segregation mechanisms have been proposed to explain these phenomena. Foo and Bridgwater[5] suggested that large particles have a tendency to migrate to the regime where higher shear exists. Savage and Lun [6] examined the case in which a mixture of small and large particles (same material) flow down a chute. They stated that a small particle has a higher possibility to sink by finding voids to fall into than a large particle.

In a wet particle flow, cohesion will compete with the collisional interaction and become dominant under some conditions. In this portion of the project, as with the "static" system, we examine – both theoretically and experimentally – the mixing and segregation in an annular shear cell. We attempt to extend previous theoretical arguments for "static" systems to sheared beds and developed phase diagrams which predict particle mixing/segregation phases.

7.1 CHARACTERIZATION TOOL

In order to use the Collision Number to examine the impact of cohesion on particle mixing/segregation, we extend the Co for a homogeneous system to binary systems where particles may have different sizes, densities and/or wetting characteristics (see Figure 14). By making an analogy to the carrier particle argument of the "static" systems (see Section 6.1), we re-define the collision number Co as

$$Co = \frac{2\pi\gamma R_e (cos\theta)_{min}}{\pi(\rho R^4)_e \lambda^2 (\frac{du}{dy})^2} \tag{7.1}$$

where γ is the interstitial fluid's surface tension, θ is the wetting angle, R_e is the geometric mean radius ($R_e = 2R_1R_2/(R_1 + R_2)$), and differing wetting characteristics are incorporated simply by using the larger value of θ (or the smaller value of $cos\theta$); $(\rho R^4)_e$ may represent either the smaller particle (1) or larger particle (2) in a dissimilar pair, depending on which is more affected by the collision between them and the surrounding environment (i.e., which has the smaller ratio of particle weight to collision force).

7.2 PHASE DIAGRAM

It is obvious that there are three collision numbers in binary systems, i.e., Co_{11}, Co_{22}, and Co_{12}, where 2 is defined as the larger of the particles. Comparing the magnitudes of these Co_{ij} leads to two dimensionless groups

$$\Re_1 = \frac{Co_{11}}{Co_{12}} \tag{7.2}$$

$$\Re_2 = \frac{Co_{22}}{Co_{12}} \tag{7.3}$$

After lengthy algebraic manipulation and by defining $\alpha = \rho_1/\rho_2$, $\beta = R_1/R_2$, and $\lambda = \cos\theta_1/\cos\theta_2$, we obtain

when $\alpha < \frac{3\beta-1}{\beta^3(\beta+1)}$

$$\Re_1 = \frac{1}{2}(1+\beta)\frac{cos\theta_1}{(cos\theta_1, cos\theta_2)_{min}} \tag{7.4}$$

$$\Re_2 = \frac{2\alpha\beta^3}{\alpha\beta^3+1}\frac{cos\theta_2}{(cos\theta_1, cos\theta_2)_{min}} \tag{7.5}$$

when $\frac{3\beta-1}{\beta^3(\beta+1)} < \alpha < \frac{\beta+1}{\beta^3(3\beta-1)}$

$$\Re_1 = \frac{1}{8}(1+\frac{1}{\alpha\beta^3})(\beta+\frac{1}{\beta}+2)\frac{cos\theta_1}{(cos\theta_1, cos\theta_2)_{min}} \tag{7.6}$$

$$\Re_2 = \frac{2\alpha\beta^3}{\alpha\beta^3+1}\frac{cos\theta_2}{(cos\theta_1, cos\theta_2)_{min}} \tag{7.7}$$

when $\alpha > \frac{\beta+1}{\beta^3(3\beta-1)}$

$$\Re_1 = \frac{2}{\alpha\beta^3+1}\frac{cos\theta_1}{(cos\theta_1, cos\theta_2)_{min}} \tag{7.8}$$

$$\Re_2 = \frac{2\alpha\beta^3}{\alpha\beta^3+1}\frac{cos\theta_2}{(cos\theta_1, cos\theta_2)_{min}} \tag{7.9}$$

Similar to that in a "static" system, in order to determine the mixing behavior we can then *analytically* determine the locations of the phase boundaries of our mixing/segregation diagram by identifying where in the parameter space of size ratio (β), density ratio (α), and wetting angle ratio (λ) differing hierarchies of Co_{ij} are observed.

The following cases may be observed

$$\Re_1 < 1, \Re_2 < 1 \qquad \frac{2\alpha\beta^3}{\alpha\beta^3+1} < \lambda < \frac{2}{1+\beta} \tag{7.10}$$

$$\Re_1 < 1 < \Re_2 \qquad \lambda < \frac{2\alpha\beta^3}{\alpha\beta^3+1} \tag{7.11}$$

$$\Re_2 < 1 < \Re_1 \qquad \lambda > \frac{2}{1+\beta} \tag{7.12}$$

When $\lambda < 2\alpha\beta^3/(\alpha\beta^3+1)$ or $\lambda > 2/(1+\beta)$, either $\Re_1 > 1$ or $\Re_2 > 1$ is true. This implies that the interaction of the two dissimilar particles (i.e., the "mixing" interaction) is always less significant than the interaction of the two similar particles (see Figure 14). In fact, for some values of λ, the dissimilar particles interaction is the least significant of the three possible interactions. We expect that this region of parameter space will therefore always favor segregation as similar particles cluster together and exclude dissimilar ones.

In contrast, in the case of $2\alpha\beta^3/(\alpha\beta^3+1) < \lambda < 2/(1+\beta)$, both $\Re_1$ and $\Re_2$ are less than 1. This indicates that the interaction between dissimilar particles is the strongest, therefore

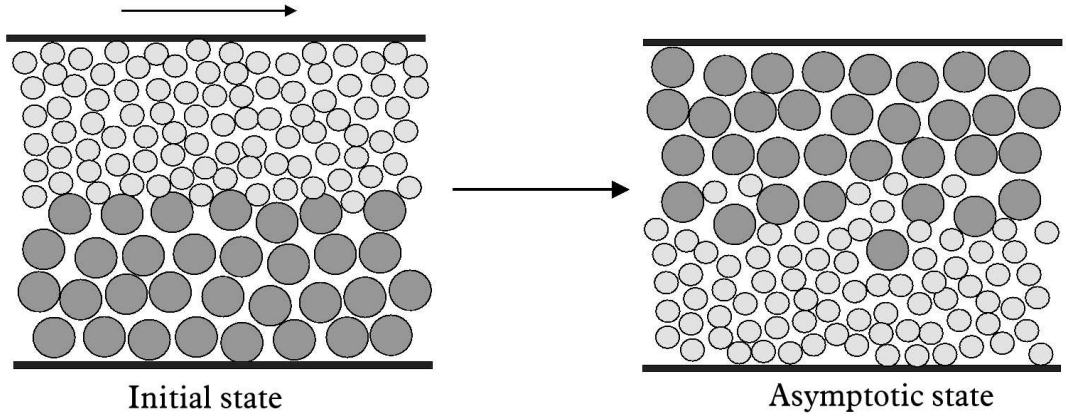

Figure 22: Non-cohesive segregation under shear

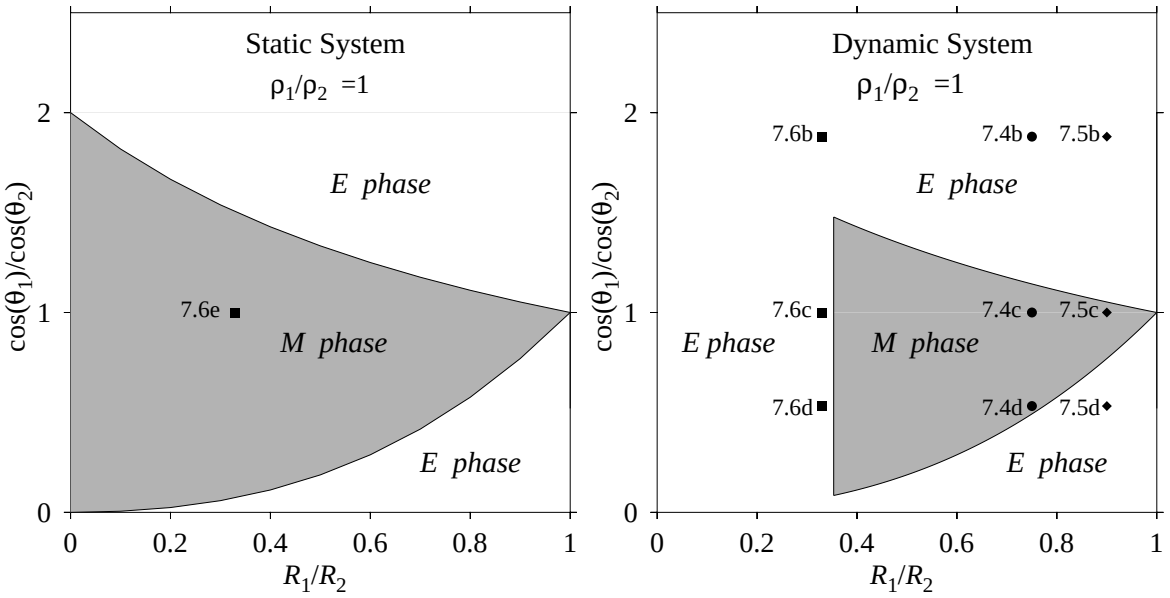

Figure 23: Phase Diagrams. (**Left**) Phase diagram determined by Bo_g for the systems with $\rho_1/\rho_2 = 1$. (**Right**) Phase diagram determined by Co for the systems with $\rho_1/\rho_2 = 1$. Compared to Left figure, one might notice the M phase shrinks as some regions becomes part of E phase.

favoring intimate particle mixing. Systems that lie in this region of parameter space are expected to be more mixed than the corresponding dry experiment.

A phase diagram then is developed to incorporate the implications of combining equations 7-10, 7-11 and 7-12, which outline regions of mitigated (M phase) and enhanced (E phase) segregation for particle mixing/segregation. The definitions of these phases are based on the values of $\Re_1$ and $\Re_2$, as in the case of the "static" system; that is, values of $\Re_i$ greater than 1 lead to segregation. Figure 7.2 shows the phase diagrams for the case of $\alpha = 1$. In the plot, the gray region corresponds to the M phase where both $\Re_i$ values are less than 1. Compared to left figure, one might notice the M phase shrinks as the light gray region becomes part of E phase.

7.3 EXPERIMENTAL SETUP

We choose an annular shear cell to conduct the experiments[131, 132, 133]. Figure 24 is the schematic diagram of the annular shear cell. In this apparatus, two stationary cylinders sit on a leveled metal plate: the inner one is made of stainless steel (17.2cm of diameter), and the outer one (21.6cm of diameter) is made of ultraviolet transmission (UVT) acrylic which allows the capture of the particle distribution via digital camera and video camera. To initiate an experiment, approximately 260ml of beads are initially layered (larger particles on the bottom and smaller particles on the top) into the 2.2cm gap between the two cylinders. On the top of the particle bed sits an annular ring which is made of stainless steel. The annular ring weighs roughly 2.0kg and is rotated by a computer-controlled motor. This ring is also free to move in the vertical direction to allow bed dilation, and thus achieve a constant pressure boundary condition. The bottom surface of the annular ring is coated with a layer of steel beads affixed in a random pattern to prevent particles from sliding. Since the gap width is small compared to the radius of the cylinder, we assume it is a pseudo-two-dimensional experiment with periodic boundaries in the streamwise direction.

We choose soda-lime glass beads for the experiment. Before each experiment, all the beads are soaked in a dilute HF solution both to clean the surfaces as well as produce

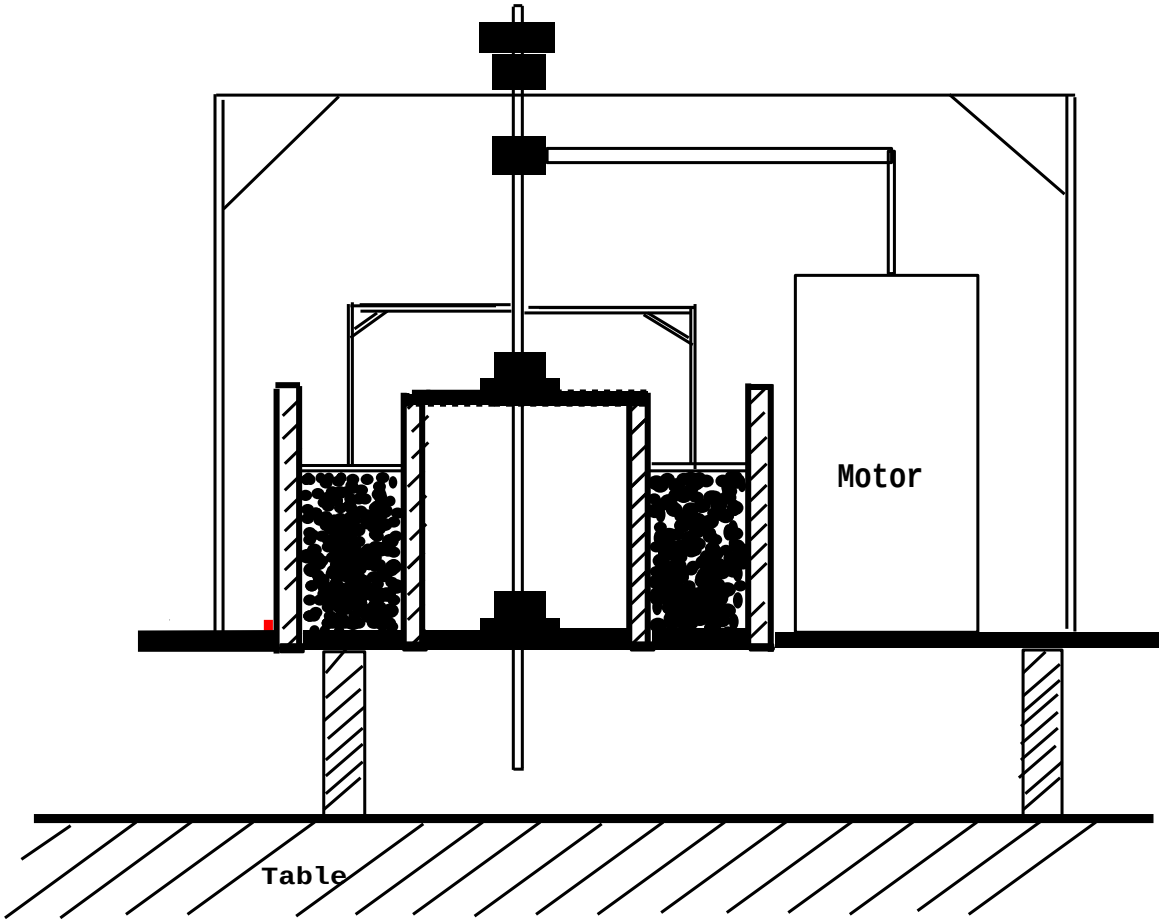

Figure 24: A schematic of the experimental annular shear cell.

Table 4: List of experiments conducted in "dynamic" systems.

Exp.	R_1 (mm)	R_2 (mm)	ρ_1 (g/cm^3)	ρ_2 (g/cm^3)	θ_1	θ_2	*Phase*
7.4a	0.75	1.0	2.5[1]	2.5			dry
7.4b	0.75	1.0	2.5	2.5	20°	60°	E
7.4c	0.75	1.0	2.5	2.5	60°	60°	M
7.4d	0.75	1.0	2.5	2.5	60°	20°	E
7.5a	0.9	1.0	2.5	2.5			dry
7.5b	0.9	1.0	2.5	2.5	20°	60°	E
7.5c	0.9	1.0	2.5	2.5	60°	60°	M
7.5d	0.9	1.0	2.5	2.5	60°	20°	E
7.6a	0.5	1.5	2.5	2.5			dry
7.6b	0.5	1.5	2.5	2.5	20°	60°	E
7.6c	0.5	1.5	2.5	2.5	60°	60°	E
7.6d	0.5	1.5	2.5	2.5	60°	20°	E
7.6e	0.5	1.5	2.5	2.5	60°	60°	M

approximately uniform surface roughnesses. Depending on the experiment, half are further treated with a surface-modifying hydrophilic silane (and a trace amount of fluorescent silane following a procedure detailed in Ref. [134]) and the other half with a hydrophobic silane (and a trace amount of colored fluorescent silane). As a result, the particles have wetting angles of $\theta \approx 20^o$ (hydrophilic) and $\theta \approx 60^o$ (hydrophobic), respectively. The wetting angles of beads are measured by inspection of magnified images of roughly micro-liter sized droplets on actual particle surfaces. The range of particle mechanical and surface properties examined in these experiments are summarized in Table 4.

We conduct experiments first with dry beads, then repeat the experiment under the same conditions except with the addition of a small amount of glycerol (≈1% by volume) – glycerol has approximately the same surface tension as water but a lower vapor pressure at room temperature. In each experiment, the rotation rate of the annular ring is set to 0.18 *rps* so that $Bo_g > Co > 1$ which is the case (2) ("fast" flow) discussed in Section 5.2. This implies the system is "cohesive" and Co is dominant in the flow. The particle distribution becomes time invariant after about 1 hour (i.e., the system reaches its asymptotic state). Pictures of the particle distribution are taken for later analysis. The effect of the cohesion force can be elucidated with an examination of the difference in the pictures between the dry and wet case at the corresponding asymptotic states. At the same time, we also apply a digital image processing technique to calculate concentration profiles for smaller (brighter) particles versus height of the bed, which provides quantitative support of our findings.

7.4 EXPERIMENTAL RESULTS AND DISCUSSION

7.4.1 Concentration profile

We first conduct two sets of binary experiments to test our theory. One set of experiments is with glass beads of 0.75 mm (radius) along with 1.0 mm – i.e., the size ratio is 0.75 (Table 4, experiments $7.4a, 7.4b, 7.4c, 7.4d$; Figure 25). The other set is with glass beads of 0.9 mm along with 1.0 mm – i.e., the size ratio is 0.9 (Table 4, experiment $7.5a, 7.5b, 7.5c, 7.5d$; Figure 26).

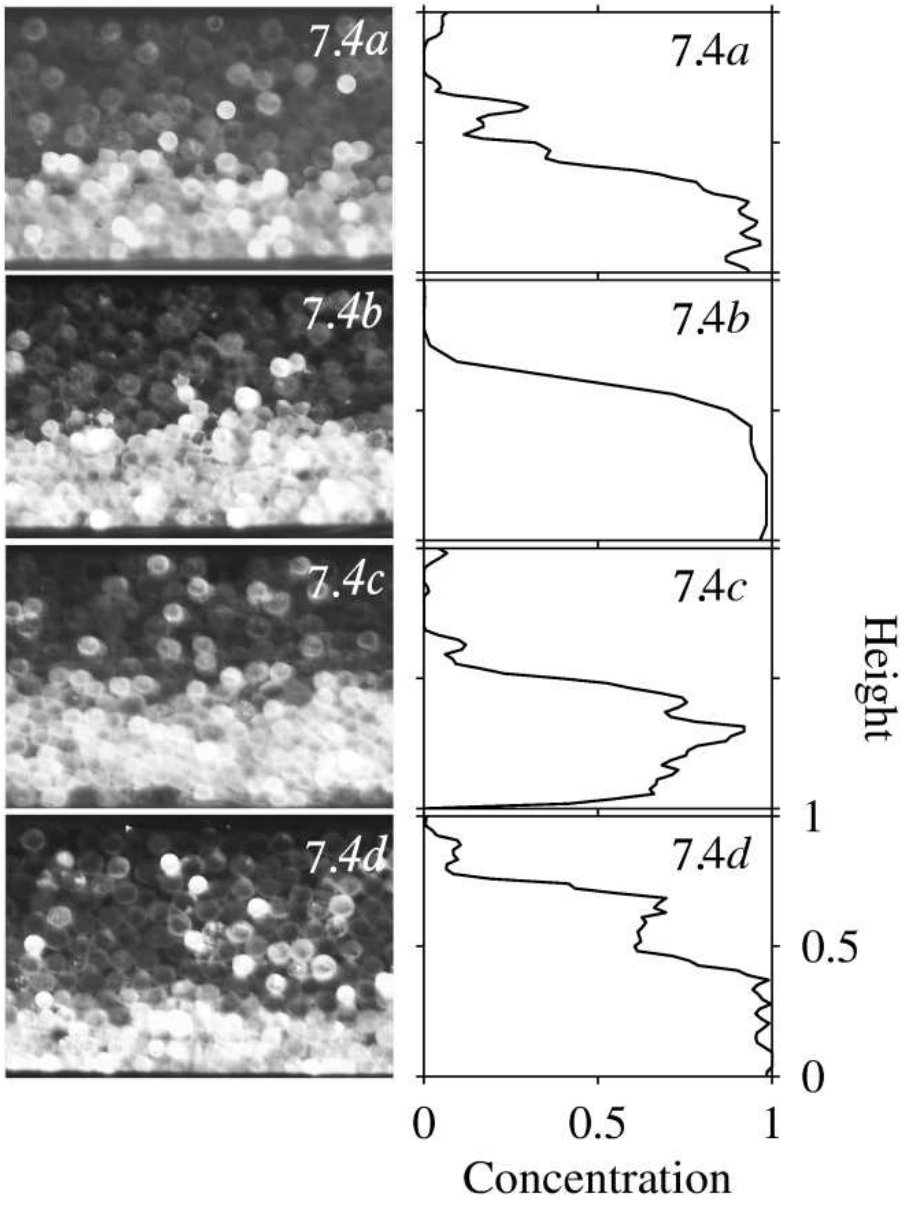

— From top to bottom, the images and concentration profiles represent results when dry – (7.4a); wet with the smaller/brighter particle being more hydrophilic – (7.4b); wet with both particles having similar wetting characteristics – (7.4c); and wet with the smaller/brighter particle being more hydrophobic – (7.4d). Results are in agreement with the predictions from theory (Figure 7.2). —

Figure 25: (**Left**) Experimental images for size ratio 0.75. (**Right**) Dimensionless concentration profiles of brighter/smaller beads versus height of the bed for corresponding experiments.

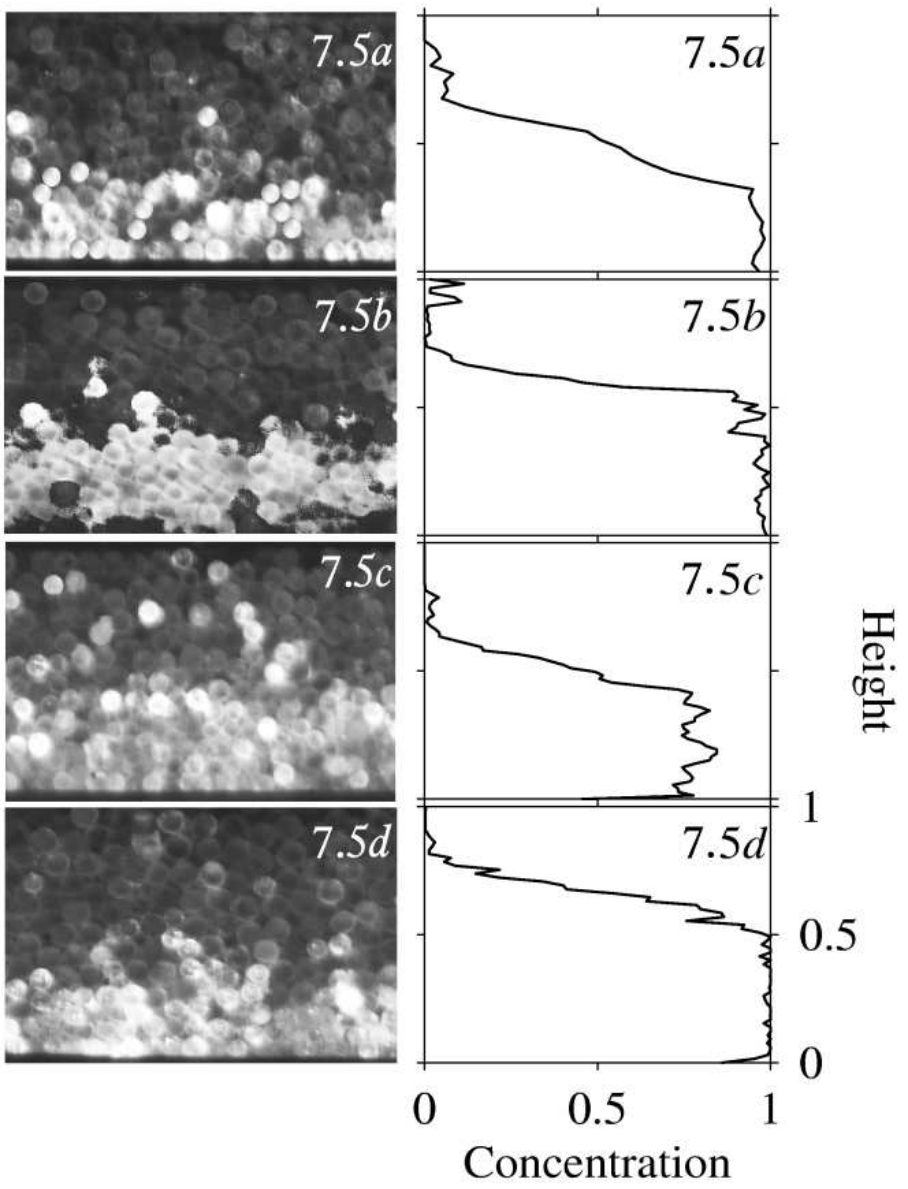

— From top to bottom, the images for size ratio 0.9 and concentration profiles of smaller/brighter beads (versus height of the bed) represent results when dry – (7.5a); wet with the smaller particle being more hydrophilic – (7.5b); wet with both particles having similar wetting characteristics – (7.5c); and wet with the smaller/brighter particle being more hydrophobic – (7.5d).

Figure 26: Experimental results for size ratio 0.9

For both size ratios, the dry cases (system 7.4a and 7.5a) lead to strong vertical segregation due to size differences (Figure 25(a) and 26(a)) — i.e., the smaller (brighter) particles stay at the bottom areas while the larger ones remain at the top areas when the asymptotic state is reached. When smaller (brighter) particles are more hydrophilic (Figure 25(b) and 26(b)), the system 7.4b and 7.5b represent the E phase (point 7.4b and 7.5b in Figure 23). We therefore expect that the segregation achieved in the dry cases will be enhanced (or remain strong) by adding glycerol. Figure 25(b) and 26(b) show that almost all of the larger particles (darker) stay in the upper region and the smaller/brighter ones remain in the lower region, as expected. The concentration profiles for smaller particles also show a steeper slope for the transition from the darker to the brighter area, indicating stronger segregation. When the particles have similar wetting characteristics (but with different colors, Figure 25(c) and 26(c)), we obtain the M phase (point 7.4c and 7.5c in Figure 23) so that more smaller/brighter particles are found to stay in the upper region and larger/darker particles in lower region, respectively, compared to the dry case, i.e., particles mix more than would be achieved in the dry cases. The concentration profiles for both cases show a smaller concentration of brighter beads at the bottom and a larger concentration on the top relative to the dry case. Finally, when the smaller/brighter particles are more hydrophobic (see Figure 25(d) and 26(d)), the systems respond differently. While the system 7.4d lies in M phase (point 7.4d in Figure 23) so that segregation is mitigated (Figure, 25(d)), the system 7.5d remains firmly in the E phase, therefore it stays strongly segregated as in the dry case.

We next conduct a set of experiments with glass beads of 0.5 mm along with 1.5mm – i.e., the size ratio is 0.33 (Table 4, experiments 7.6a, 7.6b, 7.6c, 7.6d; Figure 27). As shown in Figure 27(a), system 7.6a (dry case) segregates strongly. System 7.6b – smaller/brighter particle are more hydrophilic – remains firmly in the E *phase* (point 7.6b in Figure 23), therefore the particles also strongly segregate as predicted (Figure 27(b)). When the particles have similar wetting characteristics (but with different colors), as opposed to the cases of systems 4c and 5c, the system 7.6c stays in the E phase such that the particles segregate strongly (Figure 27(c)). Finally, when the smaller particles are more hydrophobic (system 7.6d), the system 7.6d also remains in E phase, and particles segregate as expected.

If one compares the phase diagram determined by Co to that by Bo_g, it is obvious that the M phase shrinks and E phase expands as some regions in Figure 23 (right) becomes part of the E phase. Therefore, it is interesting to note that the system 7.6c, which is in the E phase under Co dominant conditions, would evolve into the M phase (system 7.6e, Figure 23) if Bo_g becomes dominant (i.e., at smaller rotation rates of annular ring). In other words, our theory predicts that the particle distribution could be manipulated by varying shearing condition and that, in this specific instance, shearing (stirring) harder will cause more segregation! Therefore, we repeat the experiment with system 7.6c except with the rotation rate of 0.02 rps (point 7.6e in Figure 23), so that $Co \gg Bo_g > 1$. Experimentally, the procedure remains identical except that, we extend our experiment to around 2 hours before pictures are taken in order to assure we have reached the asymptotic state. As predicted by Figure 23, Figure 27(e) shows particles in this system are more mixed compared to both of the corresponding dry case 7.6a (Figure 27(a)) and the system 7.6c (Figure 27(c)).

7.4.2 Intensity of segregation

We apply another digital image processing technique to quantify the change of particle distribution in the system. The entire process of the particle migration in the system, from the initial state to steady state, is filmed using a digital camcorder. Then the movie is split into many stationary frames each containing the same number of pixels. In the frames, each pixels is identified as "red" or "green" pixel using a procedure similar to that outlined in Section 6.4.2. From the resultant concentration maps the concentration of red or green pixels in the entire area may be calculated.

By tracing the variation of IS, one can get a clear and complete picture about the kinetic movement of particles in the system. In dry cases, the segregation by size will force larger particles (initially loaded at the lower region) to migrate to the upper region and smaller particles (initially loaded at the upper region) to move down toward the lower region. This "migration" results in the occurrence first of mixing then demixing as the two types of particles cross the initially loaded boundary. After about 1 hour, the particle distribution in the system becomes relatively constant and the system is believed to have reached the asymptotic state.

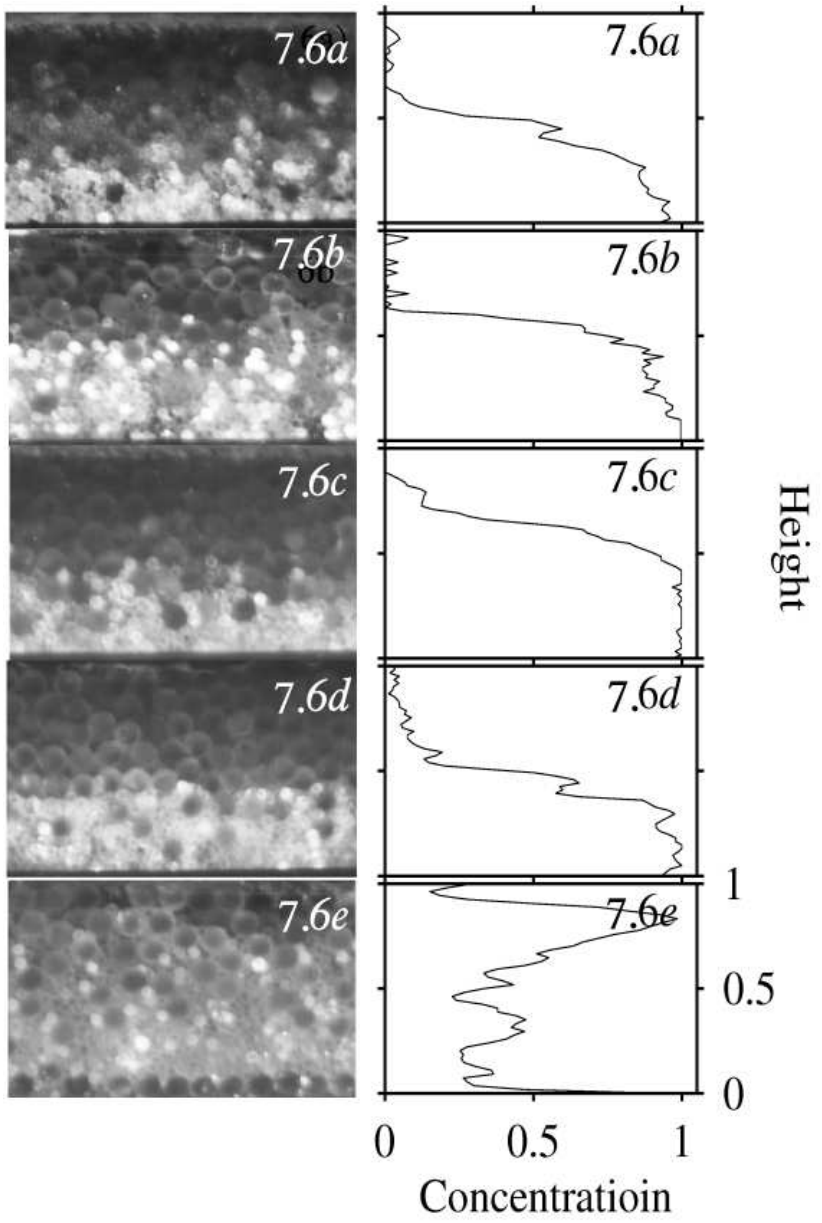

— From top to bottom, the images for size ratio 0.33 and concentration profiles represent results when dry – (7.6a); wet with the smaller/brighter particle being more hydrophilic – (7.6b); wet with both particles having similar wetting characteristics – (7.6c); and wet with the smaller/brighter particle being more hydrophobic – (7.6d); wet with both particles having similar wetting characteristics but slower shearing rotation – (7.6e).

Figure 27: Experimental results for size ratio 0.33

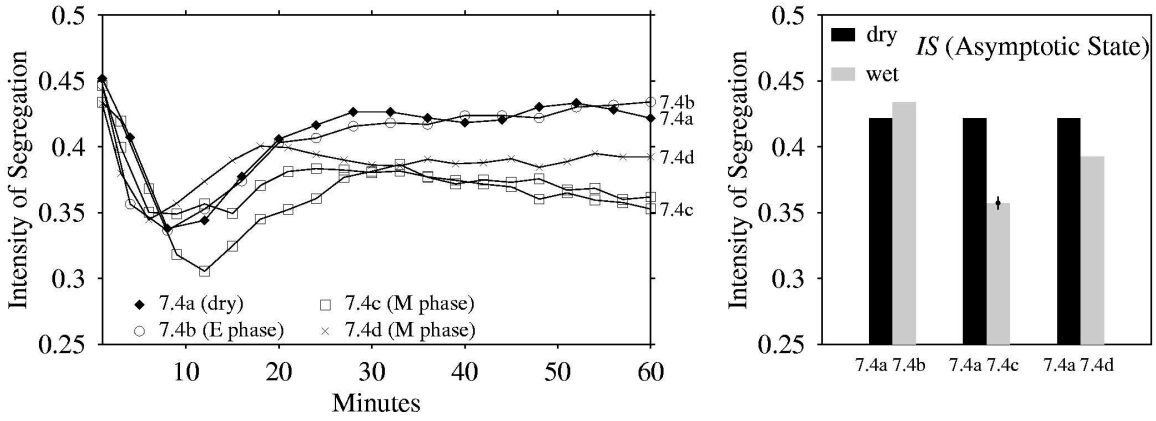

— Intensity of segregation decreases from initial state, once the shearing is added on the system and both types of particles start migration; After *IS* reaches the smallest value where the particles are believed to be most evenly distributed, it turns to increase continuously and eventually reaches a relatively constant value where the system is at the asymptotic state. The values of wet case are different from that in dry case dependent on the locations of the systems in the phase diagram (Figure 7.2) —.

Figure 28: **Left**: Variation of Intensity of Segregation of experiments of 7.4a, 7.4b, 7.4c and 7.4d. **Right**: Intensity of Segregation of experiments of 7.4a, 7.4b, 7.4c and 7.4d at the asymptotic states

This kinetic change could be visualized by examining the variation of Intensity of Segregation as a function of time (see line 7.4(a) in Figure 28). *IS* has the biggest value at the initial state since the particles are loaded in a completely segregated configuration. When the shearing is begun, *IS* starts decreasing from its initial value until it reaches the minimum value (where particles are believed to be distributed most evenly in the entire region, i.e., the extent of mixing is maximum). When demixing occurs, we see *IS* begins to increase, until the system reaches the asymptotic state, and the *IS* becomes relatively constant.

In each wet case, the segregation by size still forces the particle to migrate in order to reach the asymptotic state; however the particle distribution at the asymptotic state under these conditions differs from that in the dry case due to the impact of cohesion force (see line 7.4(b), 7.4(c), and 7.4(d) in Figure 28). In other words, particle segregation is either enhanced or mitigated dependent on the locations of the systems in the phase diagram (point 7.4b, 7.4c and 7.4d, Figure 23). Specifically, while system 7.4b is in the E phase, and therefore has a higher intensity of segregation at the asymptotic state compared to the dry case 7.4a; both system 7.4c and system 7.4d are in the M phase, and have lower intensity of segregations (see Figure 28).

In Figure 29, as in the case of the "static" system, we show the values of the mixing extent change and both values of $\Re_i$, but highlight the expected critical value as a solid symbol. Again, our theory predicts that all experiments should lie in either the upper left or lower right quadrants (as our critical values do), see Picture 29

Table 5 lists all the $\Re_1$, $\Re_2$ and IS values for the experiments conducted, as well as the percentage change from the corresponding dry cases. A positive change means the system is more mixed than in the dry case while a negative change means more segregated.

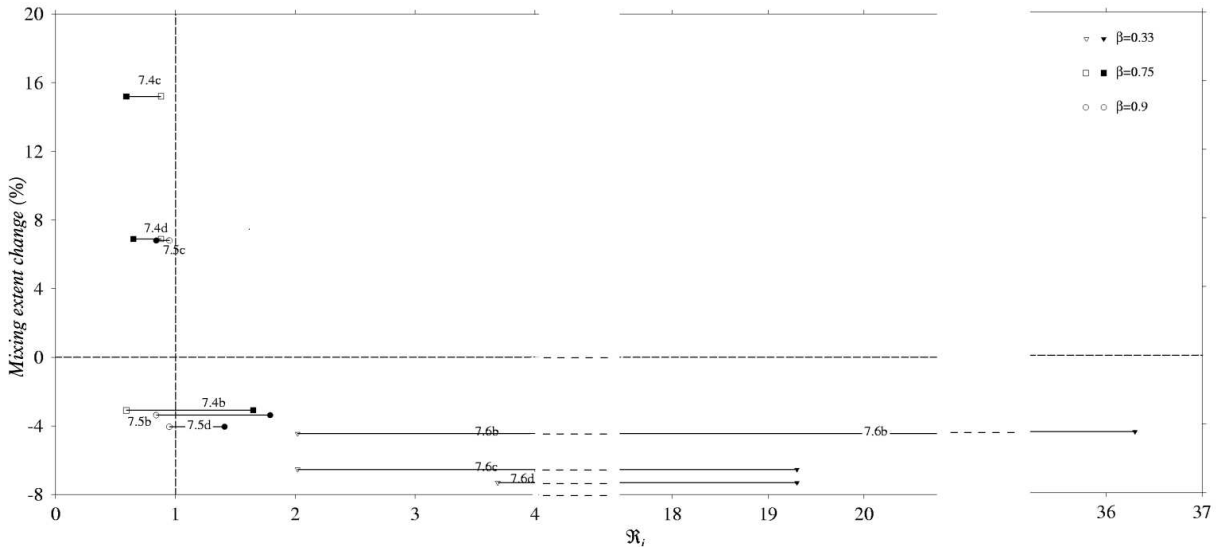

— The change in the extent of mixing is expected to be positive for values of $\Re_i$ <1 and negative for $\Re_i$ >1. Here we plot the values of the extent change and $\Re_i$ for experiments in Figures 7.4, 7.5, and 7.6. —

Figure 29: Mixing extent variation of shearing cohesive systems.

Table 5: Mixing rate variation (Intensity of Segregations) for the experiments. Negative symbol represents the segregation is enhanced and positive means the segregation is mitigated.

	Dry case	**Wet case**	**Wet case**	**Wet case**	**Wet slower case**
	7.4a	7.4b	7.4c	7.4d	
$\Re_1$		1.65	0.88	0.88	
$\Re_2$		0.59	0.59	0.65	
IS	0.421	0.434	0.357	0.392	
change %		-3.09%	15.2%	6.89%	
	7.5a	7.5b	7.5c	7.5d	
$\Re_1$		1.79	0.95	0.95	
$\Re_2$		0.84	0.84	1.41	
IS	0.385	0.398	0.359	0.4006	
change %		-3.38%	6.8%	-4.05%	
	7.6a	7.6b	7.6c	7.6d	7.6e
$\Re_1$		36.3	19.3	19.3	
$\Re_2$		2.02	2.02	3.69	
IS	0.382	0.399	0.407	0.410	0.342
change %		-4.45%	-6.54%	-7.32%	10.47%

8.0 VAN DER WAALS COHESION

When the size of particles is very small, the impact of the van der Waals force on the behavior of particles becomes significant. A better understanding of the impact of this force on the modeling and processing of particles would be of use to many industries (e.g., mixing and segregation). Despite an advanced understanding of contact mechanics[135, 83, 77, 136], none of the current computational models are capable of resolving both normal and tangential interactions of elastic-plastic particles in the presence of adhesion.

The impact of the adhesion force on the behavior of colliding particles/surfaces has long attracted attention from researchers[137, 138, 135, 83, 139]. Johnson *et al* [137] developed a model (i.e., **JKR** model) that includes the adhesion force on the deformation of elastic adhered particles in normal contact. In this model, it is assumed that the adhesion between particles are of infinitely short range and act only over the contact area. The contact area predicted by this model is larger than that predicted under the condition of no adhesion. This model leads to a finite negative load, i.e., pull-off force, that is required to separate the surfaces, given by $F_c = 3\pi\Gamma R^*$ (Γ is the surface energy of particles). An alternative model developed by Derjaguin *et al*. (**DMT** model) [138] instead argues that the adhesive normal forces should have a finite range outside the contact area. This model predicts a slightly larger pull-off force of $F_c = 4\pi\Gamma R^*$. The **JKR** model is most appropriate when soft materials with strong short-range adhesion are in elastic contact, while contacts between stiff materials with long-range attraction are better described by **DMT** [140]. Savkoor and Briggs [135] addressed the effect of tangential forces on the size of the contact area and normal contact stiffness. Recently Thornton *et al* [83] combined the work of Savkoor and Briggs[135] and Mindlin and Deresiewicz[139] to describe the tangential behavior of elastic particles.

In this work we will use the **JKR** model to examine the normal contact of particles, and combine Walton and Braun'[77] and Thornton's work[83] to study tangential contact.

The objective of the work in this section is to provide a comprehensive examination of the behavior of colliding elastic-plastic particles in the presence of adhesion, which can serve as a useful tool to further study of mixing and segregation of adhered particles.

8.1 FORCE-DISPLACEMENT EVOLUTION

In the absence of adhesion, the normal and tangential contact forces between colliding elasto-plastic particles can be calculated by the equations from 4-4 to 4-13 in Section 4.2. However, once adhesion exists, the magnitude of the contact radii of colliding particles differs from the cases without adhesion due to the impact of adhesion. Therefore the normal and tangential contact forces calculations are more complicated for adhesive versus non-adhesive collisions.

As in the non-adhesive case, adhesive collisions may be decomposed into a loading and an unloading stage (see Figure 4.3). When two adhesive particles approach each other, at the contact point (where there is no actual overlap, i.e., α=0), the adhesive attraction between particles will make the normal contact force fall to $F = -8/9F_c$, where F_c is the pull-off force. In the initial loading stage, particles experience elastic deformation (i.e., the contact force increases as $k_n\alpha^{3/2}$). After the yield point A (Figure 30) is reached, plastic deformation occurs and will continue until point C (the transition point, Figure 30) is reached. During the entire loading stage, the overlap α and the normal contact force F continuously increase, consequently the relative velocity of the two particles is gradually reduced and the initial kinetic energy is stored as their elastic strain energy. At the point C, the overlap and the normal contact force reach maximum values (i.e, α_{max} and F_{max}), and the relative velocity of the particles become zero. At this point, the loading stage is completed.

As in the case without adhesion, the unloading stage here is assumed to be elastic with a corrected radius of curvature, R_p, due to plastic deformation. During this stage the elastic energy stored during loading is gradually released and transformed back to kinetic energy. As a result, in this stage the particles move apart with continuously decreasing overlap, α, and normal contact force, F, while the relative velocity of the particles is gradually increased. At the point B (Figure 30), the normal contact force reduces to the minimum value $-F_{cu}$.

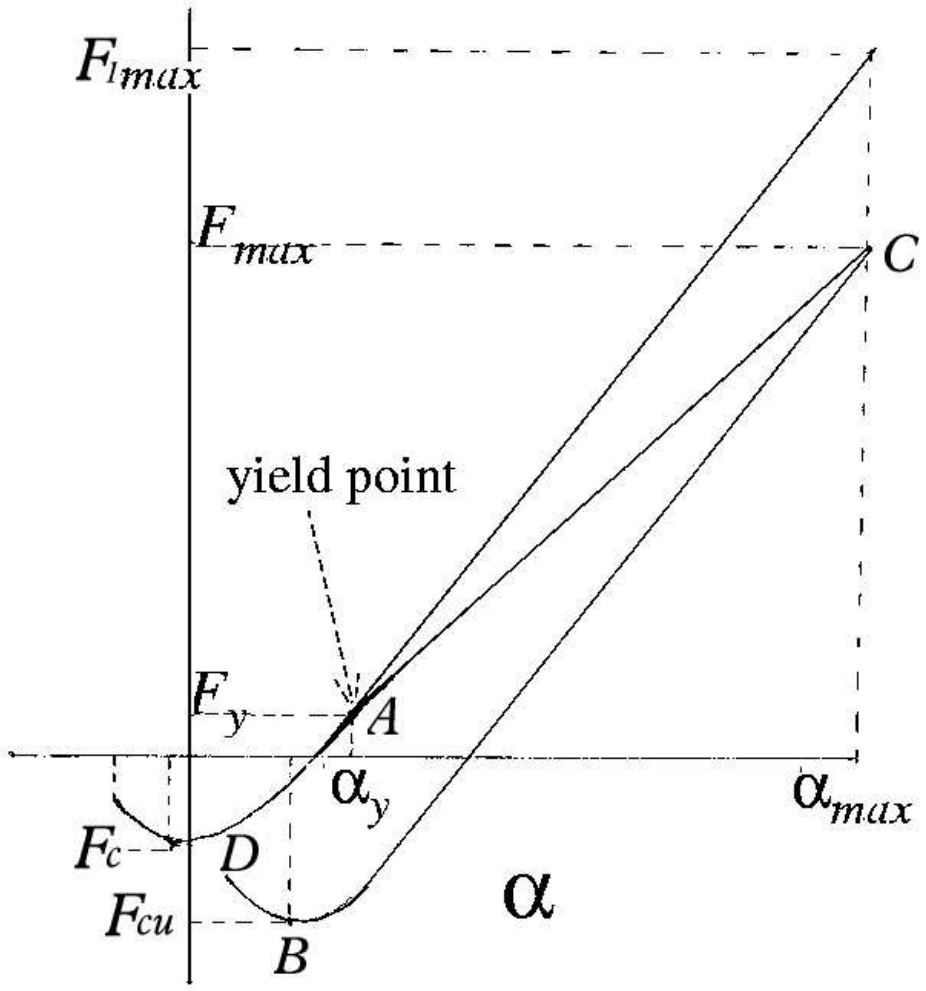

Figure 30: Force-displacement curve of plastic deformation with adhesion

Beyond that point there is insufficient elastic energy release to continue the decrease in contact force, F, and the adhesion force again dominates. Consequently, the contact force begins to increase until it reaches a value $-5/9P_{cu}$ at which time the contact breaks (point D, Figure 30).

8.2 CODE DEVELOPMENT

In this section, we outline the detailed mathematics necessary to capture the contact evolution outlined in Section 8.1.

8.2.1 Loading

8.2.1.1 Normal forces for adhesive elastic deformation Before the initial yield occurs, particles undergo elastic deformation. The normal contact force is modeled after the work of Thornton *et al* [136]. The normal force is updated at each time step as

$$F = F_{old} + \Delta F = F_{old} + k_n^e \Delta\alpha, \tag{8.1}$$

where $\Delta\alpha$ is the displacement increment and k_n^e is the normal stiffness for elastic deformation. Unlike the purely elastic case, here k_n^e depends on the degree of cohesion so that it is given as

$$k_n^e = 2E^* a \frac{3\sqrt{F_1} - 3\sqrt{F_c}}{3\sqrt{F_1} - \sqrt{F_c}} \tag{8.2}$$

where a is the contact radius given as

$$a = \sqrt[3]{\frac{3R^* F_1}{4E^*}}, \tag{8.3}$$

F_c is the pull-off force in the **JKR** model

$$F_c = \frac{3}{2}\pi R^* \Gamma, \tag{8.4}$$

and F_1 represents the effective Hertzian force which would produce the same contact area[136] (i.e., in the absence of adhesion). F_1 is given by

$$F_1 = F + 2F_c + \sqrt{4FF_c + 4{F_c}^2 - T^2E^*/4G^*}, \tag{8.5}$$

where Γ is the interface energy, and T is the tangential contact force.

It should be noted that for non-adhesive contact (i.e., $\Gamma = 0$) equation 8-5 reduce to the elastic solution.

8.2.1.2 Normal forces for adhesive plastic deformation When the normal force increases above the yield point, plastic deformation occurs. First, the initial yield state is identified by testing whether the contact radius has reached the value associated with yield, given in the expression

$$\sigma_y = \frac{2E^*a_y}{\pi R^*} - \sqrt{\frac{2\Gamma E^*}{\pi a_y}}, \tag{8.6}$$

where the subscript **y** represents the yield point, i.e., σ_y is the yield stress. Then the normal stiffness k_n^p for the subsequent plastic deformation is calculated using

$$k_n^p = \frac{3\pi R^*\sigma_y\sqrt{F_1} - 2E^*a_y\sqrt{F_c}}{3\sqrt{F_1} - \sqrt{F_c}}. \tag{8.7}$$

During plastic deformation, the plastic contact force F and the contact radius are updated by

$$F = F_{old} + \Delta F = F_{old} + k_n^p\Delta\alpha, \tag{8.8}$$

$$a = \sqrt[3]{\frac{3R^*F_1}{4E^*}}. \tag{8.9}$$

For calculation purpose, the equivalent adhesive and non-adhesive elastic force, F and F_1, are continuously updated using eqns 8-1 to 8-5, as they are necessary for unloading calculations.

8.2.2 Unloading

Unloading of a contact that has not begun to plastically yield is purely elastic, so that eqn 8-1 may be used ($\Delta\alpha$ now takes a negative value). The unloading stage beyond the yield limit is assumed to be elastic, except that the past, plastic deformation has permanently altered the (local) radius of curvature. The new radius of curvature, R_p, is given by

$$R_p = \frac{R^* F_{1max}}{F_{max} + \sqrt{4F_c F_{1max} - T^2 E^*/4G^*}}. \tag{8.10}$$

In the case where

$$4F_c F_{1max} - T^2 E^*/4G^* < 0, \tag{8.11}$$

an exception is made such that,

$$R_p = \frac{R^* F_{1max}}{F_{max}}.$$

During the unloading, the normal stiffness is changed, due to the change in apparent radius of curvature, and is now

$$k_n^u = 2E^* a \frac{3\sqrt{F_{1u}} - 3\sqrt{F_{cu}}}{3\sqrt{F_{1u}} - \sqrt{F_{cu}}}, \tag{8.12}$$

where a is the contact radius

$$a = \sqrt[3]{\frac{3R_p^* F_{1u}}{4E^*}}, \tag{8.13}$$

F_{cu} is given as

$$F_{cu} = \frac{3}{2}\pi\Gamma R_p^*, \tag{8.14}$$

and F_{1u} represents the effective Hertzian force

$$F_{1u} = F + 2F_{cu} \pm \sqrt{4FF_{cu} + 4{F_{cu}}^2 - T^2 E^*/4G^*}. \tag{8.15}$$

8.2.3 Effect of tangential forces

Savkoo and Briggs studied tangential collisions of adhesive spheres. In their analysis, which incorporates the **JKR** model into tangential contact mechanics[135], the tangential force primarily affects the behavior of colliding particles through changes in the contact radius. This effect is most apparent at the beginning stages of a collision which corresponds to a "peeling" mechanism. This can be seen from the equation 8-5. As the tangential force increases, the contact radius is reduced up to a critical value of T, give by

$$T_c = 4[\frac{(FF_c + {F_c}^2)G^*}{E^*}]^{\frac{1}{2}} \tag{8.16}$$

at which point the peeling is complete and the contact radius is given by

$$a = \sqrt[3]{\frac{3R^*(F + 2F_c)}{4E^*}}. \tag{8.17}$$

Upon further tangential loading (i.e., increase in T), Savkoor and Briggs suggested that the contact radius would be immediately reduced to the Hertzian value, $a = \sqrt[3]{3R^*F/4E^*}$. In contrast, Thornton and Yin [83] suggested that the contact radius should vary smoothly at T_c. Therefore they proposed two sliding criterion to ensure there is a smooth transition from peeling to sliding, see Ref [83].

In this work, the tangential contact stiffness is calculated and the tangential force is updated using the equations 4-11, 4-12 and 4-13 (see Section 4.2.2). The primary effect of adhesion, therefore, is through changes in contact radius and failure criterion (i.e., peeling, sliding). Adopting Thornton and Yin's modified analysis yields the following cases. For $F < F^*$, F^* is given by $F^* = 2F_c[(\eta - 1) + \sqrt{\eta(\eta - 1)}]$, where $\eta = 4G^*/(\mu^2 E^*)$, the failure criteria are given by

$$T = \mu(F + 2F_c) \qquad F \geq -0.3F_c \tag{8.18}$$

$$T = \mu F_1[1 - (F_1 - F)/3F_1]^{3/2} \qquad F \leq -0.3F_c. \tag{8.19}$$

However, when $F > F^*$,

$$T = \mu(F + 2F_c). \tag{8.20}$$

8.2.4 Contact damping

In the presence of adhesion, the attractive force discourages particle separation. Therefore when the initial relative velocity is smaller than some "capture velocity" the rebounding force is not big enough for the particle to "pull off". In this case, the contact force will oscillate continuously, and contact equilibrium will never be reached. This occurs because our contact mechanics choice dissipates energy only via plastic deformation, so that at sufficiently low velocities no energy is lost. In order to overcome this shortcoming, "contact damping" is added to the contact forces in the simulation to mimic dissipation in the form of sound, heat etc. and given by

$$damping = c\frac{E^*}{1-\nu^2} \tag{8.21}$$

where c is constant, and ν is the Poisson ratio.

Figure 31 shows the curves of normal contact forces versus impact times without application of contact damping where the impact velocities, $v = 0.2m/s$ and $v = 0.6m/s$ respectively, are below the "capture velocity". After the introduction of contact damping, the amplitudes of contact forces decrease with time and finally reach zero, see Figure 32.

8.3 CODE TESTS

Several simulations are conducted to test the code against results from the literature[136, 83, 130]. First we run a simulation with a particle (R=10μm) colliding with a wall to check the normal contact force evolution versus normal approach for non-adhesive elasto-plastic collisions. The parameters of the materials used in the simulation are: Young modulus,

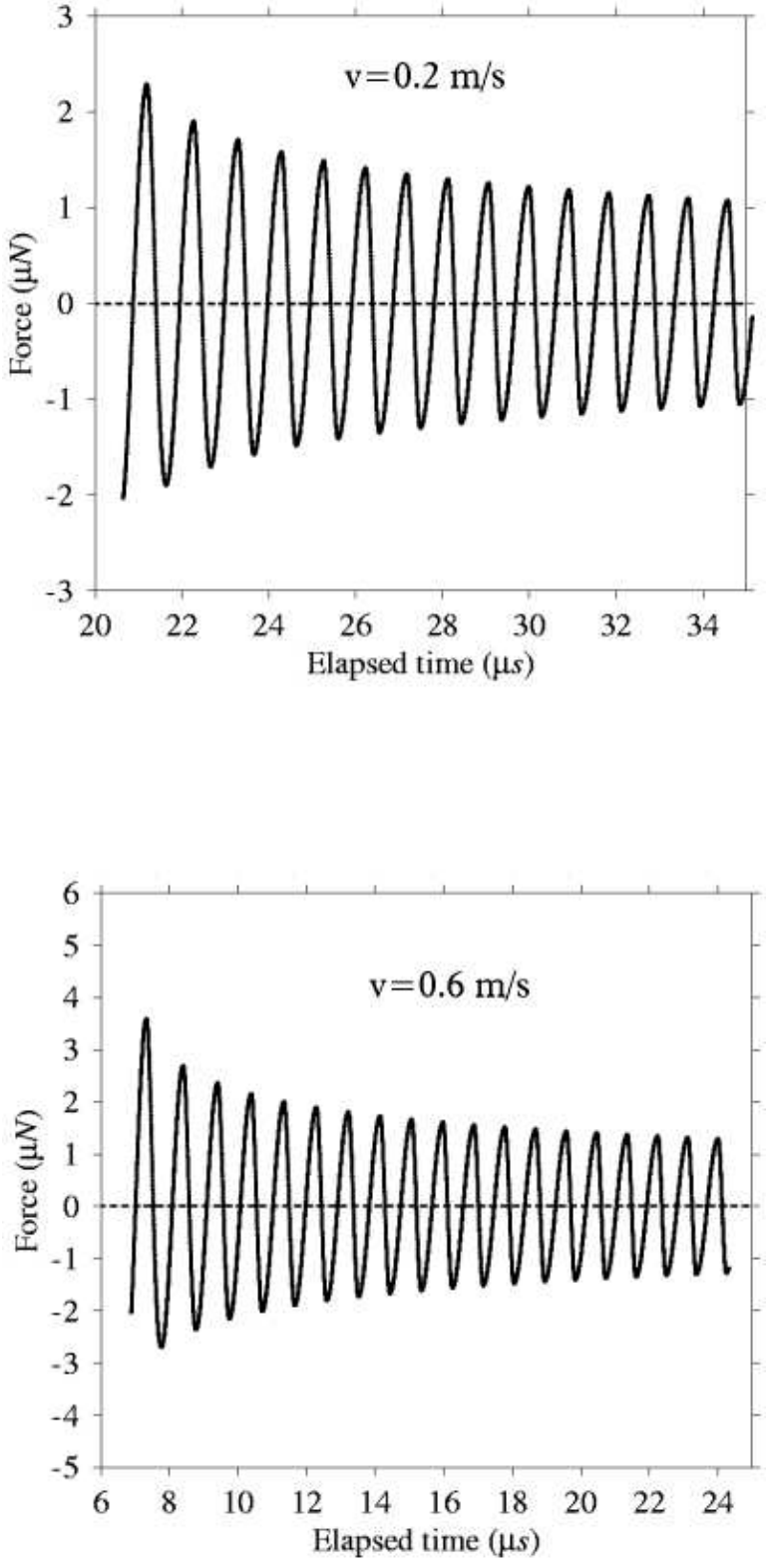

Figure 31: Normal forces versus elapsed time without contact-damping added.

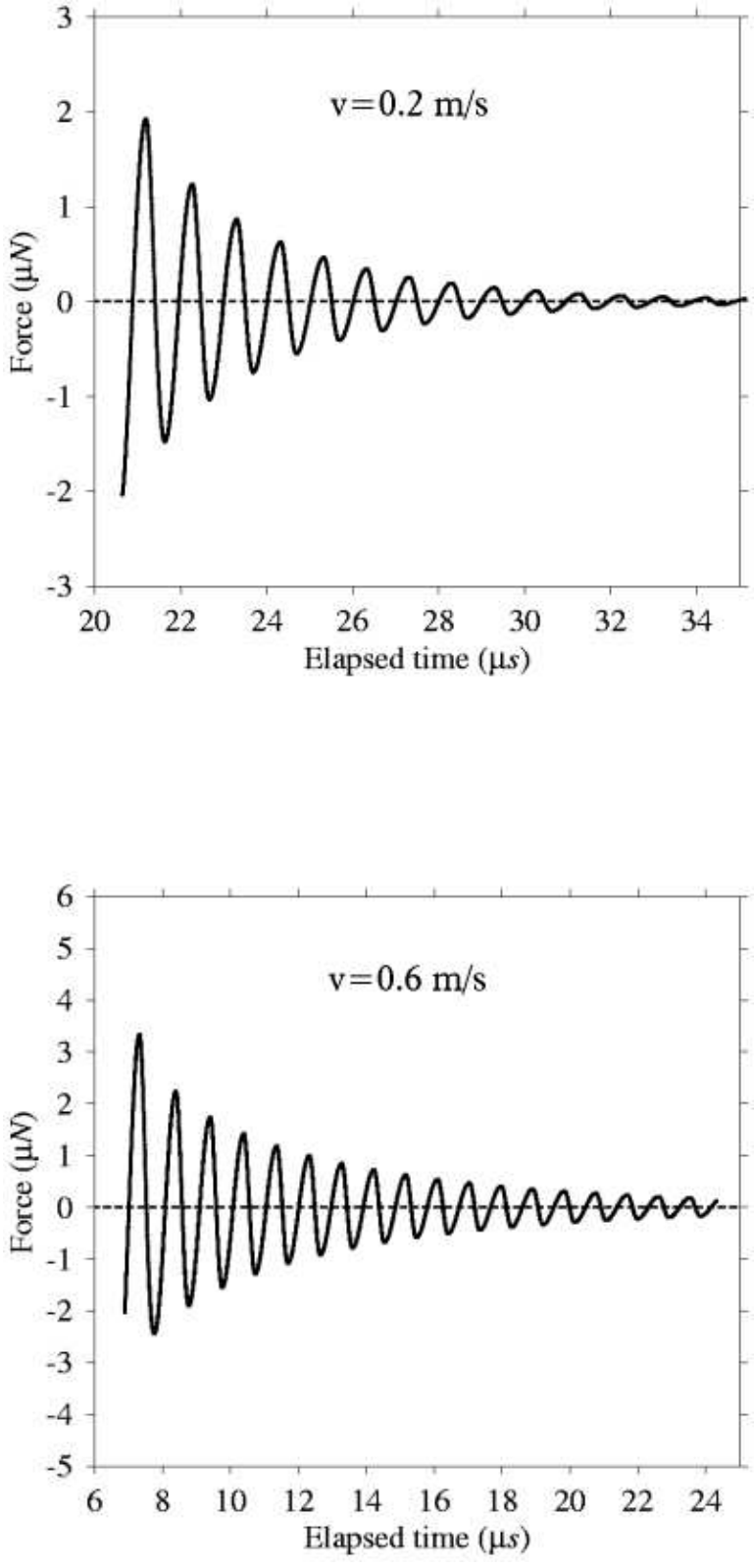

Figure 32: Normal forces versus elapsed time with contact-damping added.

$E = 215GPa$; yield stress, $\sigma_y = 3.04GPa$; density, $\rho = 8300kg/m^3$; Poisson ratio, $\nu = 0.3$; friction coefficient, and $\mu = 0.35$ for the particle; and $E = 215GPa$, $\rho = 7830kg/m^3$, $\nu = 0.3$ and $\mu = 0.35$ for the wall. Figure 33 shows the normal force-approach curves obtained for relative velocities of 5.0, 10.0 and 20.0 m/s. It can be seen that for different impact velocities, the slopes of the loading curves are equivalent to each other, as expected for non-adhesive elasto-plastic contact stiffness ($\frac{dF}{d\alpha} = 2E^* a_y$). In contrast, the slopes of the unloading curves are different since the contact curvature decreases when the impact velocity increases, causing the unloading to be stiffer. The simulation results match literature results[136] very well.

Next a simulation with adhesive particles is conducted for comparison with results reported by Thornton[83]. The simulation involves a particle ($R = 2.45\mu m$) colliding with a wall. The parameters used in this simulation are: $R = 2.45\mu m$, $\rho = 1.35Mg/m^3$, $E = 1.2GPa$, $\nu = 0.3$, $\mu = 0.35$, surface energy $\Gamma = 0.2J/m^2$ and $\sigma_y = 35.3e6Pa$ for the particle; and $\rho = 1.35Mg/m^3$, $E = 182GPa$, $\mu = 0.3$, $\mu = 0.35$ for the wall. Shown in Figure 34, as in the case of those without adhesion (Figure 33), the slopes of the loading curves are the same and those of the unloading curves are different for all relative velocities. As expected from eqn 8-14, in the unloading stage, the maximum negative normal force increases when the relative velocity increases.

Finally a simulation with two glass particles colliding obliquely is conducted. Figure 35 shows the comparison between the cases with and without adhesion, with the solid symbols representing the adhesive case and the open symbols representing the non-adhesive case. As can be seen, for all cases with adhesion, peeling occurs on the onset of loading. After peeling is complete, sliding takes place. Specifically, if the impact angle is 30^o or 45^o, the sliding continues until the tangential force increment ΔT is reduced to $\Delta T < \mu \Delta F$. Subsequently, the tangential force decreases, reverses in direction and finally, towards the end of the impact, sliding recurs. For the impact angle of 60^o, the sliding continues through the entire unloading stage of the impact. When the impact angle is 75^o, sliding occurs for the duration of the impact with no reversal of the tangential force direction.

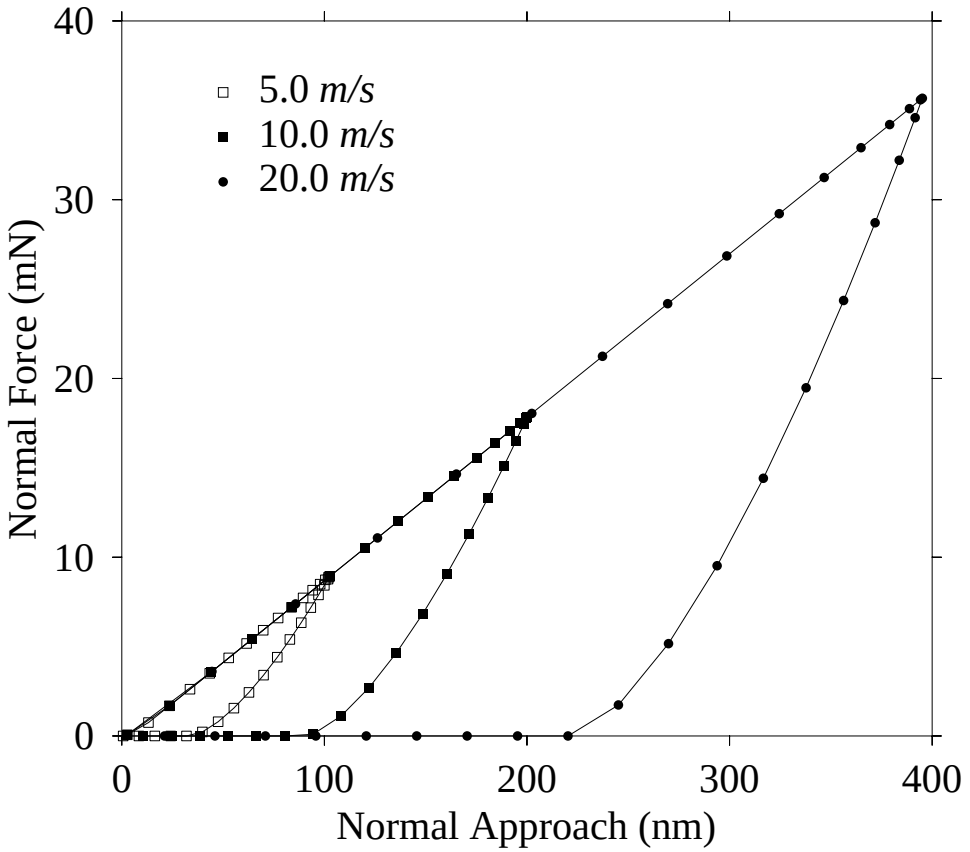

Figure 33: Force-displacement curve of normal elastic-plastic deformation without adhesion

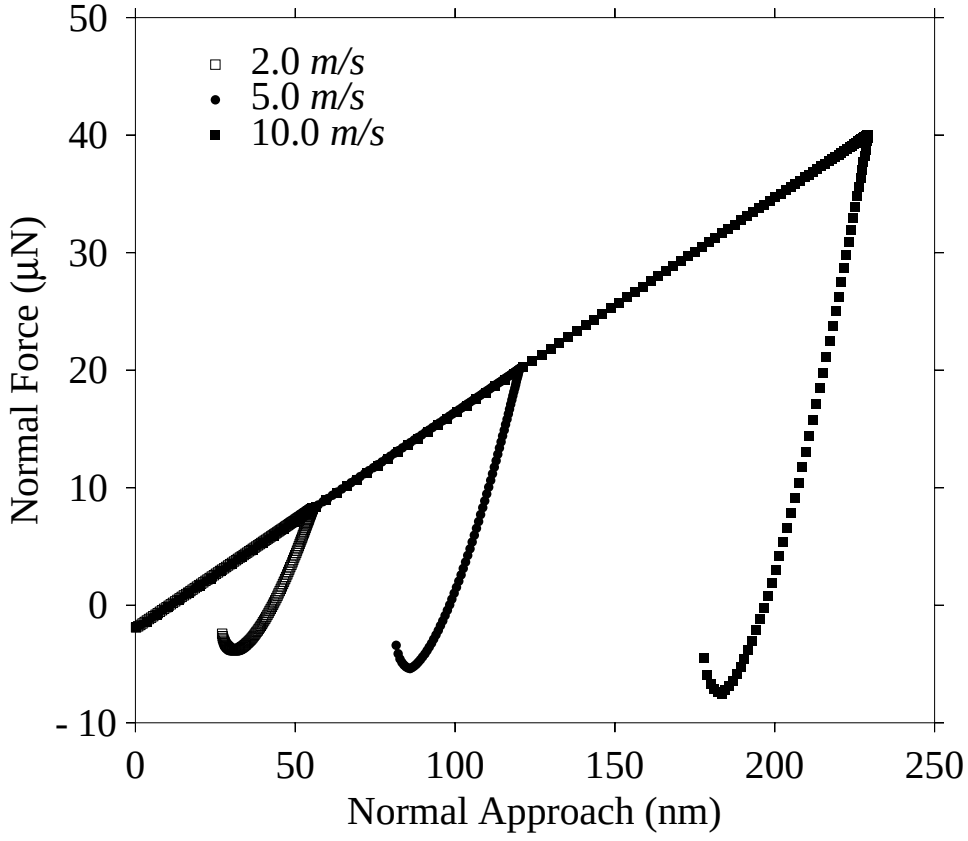

Figure 34: Force-displacement curve of normal elastic-plastic deformation with adhesion

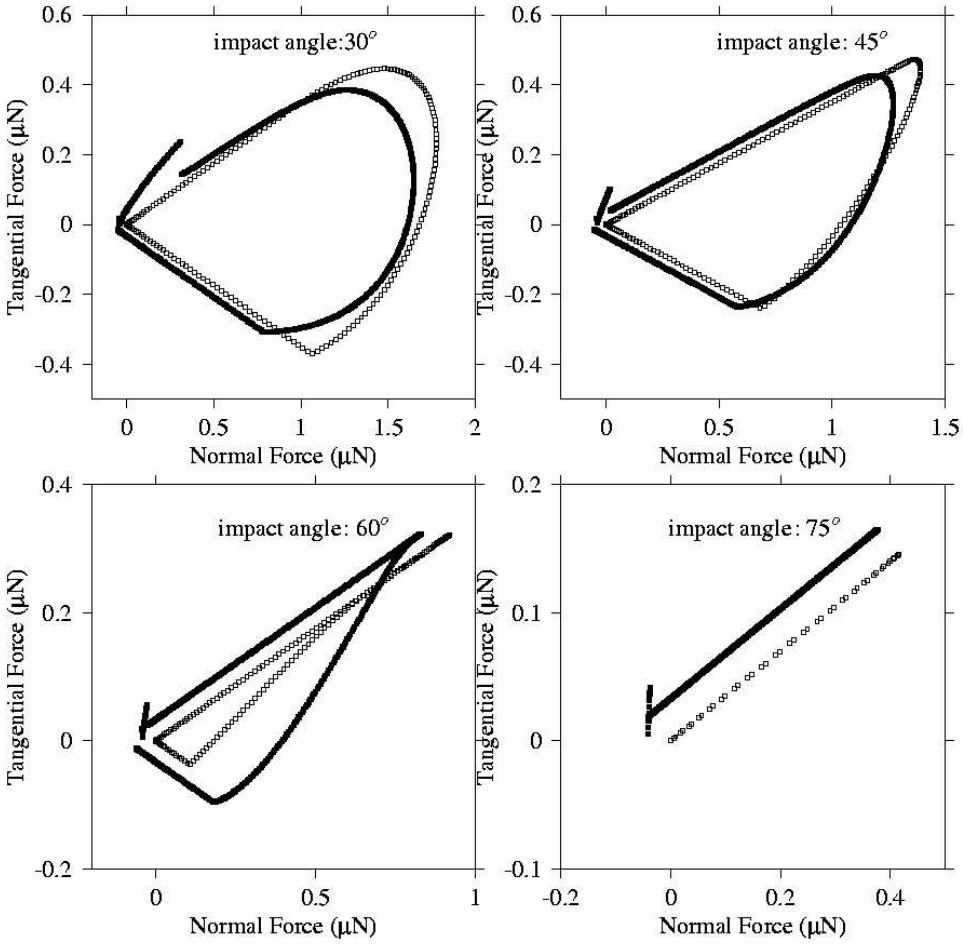

Figure 35: Force-displacement curve of oblique plastic deformation with and without adhesion

8.4 CHARACTERIZATION OF VAN DER WAALS COHESIVE MIXING

A new characterization tool is developed, which is an extension of the Granular Bond Number (Bo_g), Bo_{vdw}, used to quantify the impact of van der Waals interactions on cohesive mixing. It is given by the ratio of the van der Waals force (F_{vdw}) to the particle weight (F_w) as

$$Bo_{vdw_{ij}} = \frac{F_{vdw}}{F_W} = \frac{2\pi\Gamma_{ij}R^*}{\frac{4}{3}\pi g\ [R^3\rho]_m}, \tag{8.22}$$

where Γ is the surface energy of particles, $(R^3\rho)_m$ is the smaller of the two masses to represent the fact that less massive particle's motion will be dominated by the more massive particle (i.e., it will behave as a guest).

The values of the Bo_{vdw} for each potential pair of particles, i and j, within the system (i.e., for a binary system, the $Bo_{vdw_{11}}$, $Bo_{vdw_{22}}$, and $Bo_{vdw_{12}}$, where 2 is defined as the larger of the particles) need to then be compared.

Comparing the magnitudes of these $Bo_{vdw_{ij}}$ leads to two dimensionless groups

$$\Re_1 = \frac{vdw_{11}}{vdw_{12}} = \frac{\Gamma_{11}}{\Gamma_{12}}\ \frac{R_1+R_2}{2R_2}\ \frac{(R_1^3\rho_1, R_2^3\rho_2)_{min}}{R_1^3\rho_1} \tag{8.23}$$

$$\Re_2 = \frac{vdw_{22}}{vdw_{12}} = \frac{\Gamma_{22}}{\Gamma_{12}}\ \frac{R_1+R_2}{2R_1}\ \frac{(R_1^3\rho_1, R_2^3\rho_2)_{min}}{R_2^3\rho_2}, \tag{8.24}$$

which can be re-written by defining $\alpha = \rho_1/\rho_2$, $\beta = R_1/R_2$, and $\phi = \sqrt{\Gamma_{11}/\Gamma_{22}}$ together with ${\Gamma_{12}}^2 = \Gamma_{11}\Gamma_{22}$[50], yielding

$$\Re_1 = \frac{vdw_{11}}{vdw_{12}} = \phi\ \frac{\beta+1}{2}\ \frac{(\alpha\beta^3, 1)_{min}}{\alpha\beta^3} \tag{8.25}$$

$$\Re_2 = \frac{vdw_{22}}{vdw_{12}} = \frac{1}{\phi}\ \frac{\beta+1}{2\beta}\ \frac{(\alpha\beta^3, 1)_{min}}{1}. \tag{8.26}$$

In order to determine the mixing behavior we can then *analytically* determine the locations of the phase boundaries of our mixing/segregation diagram by identifying where in the parameter space of size ratio (β), density ratio (α), and surface energy ratio (ϕ) differing hierarchies of $Bo_{vdw_{ij}}$ are observed.

The following cases may be observed

If $\alpha\beta^3 > 1$

$$1 < \Re_1, 1 < \Re_2 \qquad \frac{2\alpha\beta^3}{1+\beta} < \phi < \frac{1+\beta}{2\beta} \tag{8.27}$$

$$\Re_1 < 1 < \Re_2 \qquad \phi < \frac{2\alpha\beta^3}{1+\beta} \tag{8.28}$$

$$\Re_2 < 1 < \Re_1 \qquad \phi > \frac{1+\beta}{2\beta} \tag{8.29}$$

If $\alpha\beta^3 < 1$

$$\Re_1 < 1, \Re_2 < 1 \qquad \frac{(\beta^3+\beta^2)\alpha}{2} < \phi < \frac{2}{1+\beta} \tag{8.30}$$

$$\Re_1 < 1 < \Re_2 \qquad \phi < \frac{(\beta^3+\beta^2)\alpha}{2} \tag{8.31}$$

$$\Re_2 < 1 < \Re_1 \qquad \phi > \frac{2}{1+\beta} \tag{8.32}$$

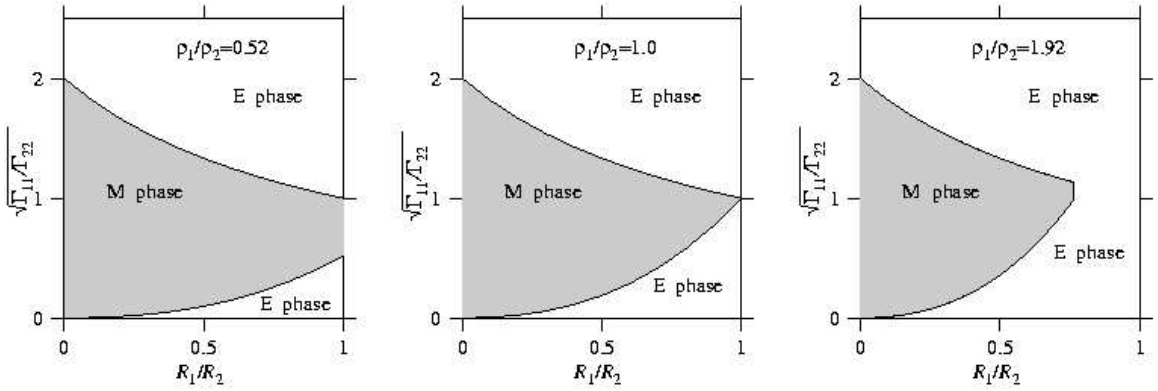

— Phase diagrams are a function of the ratios of sizes, densities, and values of the surface energy of different materials. From left to right are the phase diagrams for density ratio as 0.52, 1.0 and 1.92. As seen, the E phase shrinks as density ratio increases. —

Figure 36: Phase diagrams for binary adhesive systems.

In the case of $\alpha\beta^3 > 1$ (i.e., the smaller particle is more massive than the larger particle), either $\Re_2 > 1$ or $\Re_1 > 1$ is always true for any combination of particle properties (i.e., size, density and/or surface characteristics). This implies that the interaction of the two dissimilar

particles (i.e., the "mixing" interaction) is always less significant than the interaction of the two similar particles. In fact, for some values of ϕ, the dissimilar particles interaction is the least significant of the three possible interactions. We expect that this region of parameter space will therefore always favor segregation as similar particles cluster together and exclude dissimilar ones.

In contrast, in the case of $\alpha\beta^3 < 1$ (i.e., the small particle is less massive), when $\frac{(\beta^3+\beta^2)\alpha}{2} < \phi < \frac{2}{1+\beta}$, both $\Re_1$ and $\Re_2$ are less than 1. This indicates that the interaction between dissimilar particles is the most significant, therefore favoring intimate particle mixing. Systems that lie in this region of parameter space are expected to be more mixed than the corresponding non-adhesive experiment. For other values of ϕ, however, $\Re_2 > 1$ or $\Re_1 > 1$, so that in this region we expect some instances of cohesion-enhanced segregation.

Phase diagrams then are developed to visualize the impact of the van der Waals interaction on the mixing/segregation (see Figure 36), which outline regions of mitigated (**M** phase) and enhanced (**E** phase) segregation for particle mixing/segregation. It is clear that, in general, varying the density ratio causes a relative change in the size of the **M** and **E** phases – the **M** phase grows when the smaller particle is less dense and shrinks when it is more dense.

It is interesting to note that the phase diagrams are essentially identical to those for wet granular materials when the varying cohesion strengths are plotted as $\sqrt{\Gamma_1/\Gamma_2}$ rather that $\cos\theta_1/\cos\theta_2$ (see Figure 37).

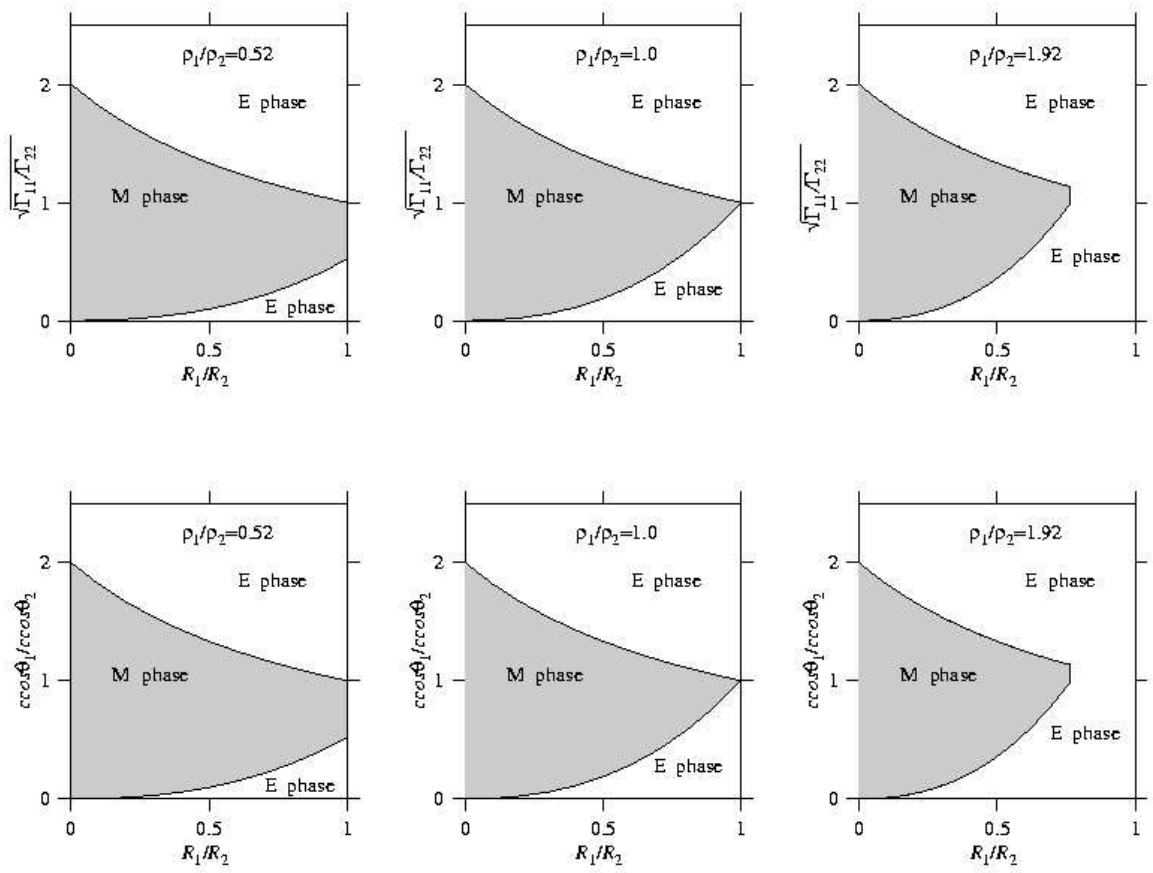

Figure 37: Top figures are phase diagrams for van der Waals cohesive systems; while bottom figures are for wet systems.

9.0 CONCLUSION

Particle mixing is encountered widely throughout industry in processes involving physical and chemical change, and is a central feature of many processes in pharmaceuticals, food, paper, ceramics and chemical industries. Segregation induced by differences in the properties of the particles alway hinders mixing operation, and may lead to problems such as low efficiency, poor quality, or even unsafe products.

Cohesive forces between particles – such as liquid bridge (capillary) forces, van der Waals forces, or electrostatic forces – become increasingly important as particle size decreases; however there are very few systematic studies of mixing and segregation in cohesive granular materials. Consequently, an understanding of the impact of cohesive forces on granular mixing and segregation remains poor.

This dissertation addresses particle mixing and segregation in cohesive (liquid-induced) systems under static and dynamic flow conditions, and examines the potential impact of van der Waals forces on these systems. It aims to provide some insight into the fundamentals of these problems for further study.

9.1 ALGORITHM

9.1.1 Liquid-bridging induced cohesion

9.1.1.1 Characterization tools By taking a discrete view of cohesion, two discrete characterization tools, Bo_g and Co, have been developed. The previous work of our group has shown that, while the Granular Bond Number, Bo_g, may be sufficient to define the granular

flow in a system where collision forces are sufficiently small (i.e., "static" system with $Co \gg Bo_g > 1$), it is necessary to consider Co in a system where the collision force is comparable to the cohesion force but larger than the particle weight (i.e., "dynamic" system with $Bo_g > Co > 1$). Furthermore, we extend Bo_g and Co for a homogeneous system to binary systems where particles may have different sizes, densities and/or wetting characteristics. In this way, we have explicitly tested the hypothesis that particle distributions at their asymptotic state can be determined by the relative importance of various forces acting on the particles.

9.1.1.2 Phase diagrams Since the liquid bridges act only pair-wise (i.e., the system is in the pendular regime), there are only three simple potential pairs of particles, i.e., 1-1, 2-2 and 1-2. We compare the values of the Bo_g or Co for different potential pairs of particles within the system, e.g., for a "static" system, we compute $\Re_1 = Bo_{g_{11}}/Bo_{g_{12}}$ and $\Re_2 = Bo_{g_{22}}/Bo_{g_{12}}$. Phase boundaries are then analytically identified by finding where in the parameter space of size ratio (R_1/R_2), density ratio (ρ_1/ρ_2), and wetting angle ratio ($cos\theta_1/cos\theta_2$) differing hierarchies of $Bo_{g_{ij}}$ are observed. When $\Re_1 < 1$ $\Re_2 < 1$, we expect that segregation will be limited at equilibrium, these systems are at **M** phase in the phase diagram. However, when either $\Re_1 > 1$ or $\Re_2 > 1$, we expect that cohesion will not mitigate segregation, but instead will lead to more segregation than would be achieved in the dry case, and these systems are at **E** phase in the phase diagrams. In general, we have shown this particle-level model can accurately predict the extent of particle mixing and segregation in cohesive wet granular systems with phase diagrams. These phase diagrams exhibit both mixed and segregated phases where the boundary is determined by the mechanical and surface properties of the particles, such that manipulation of surface properties and/or size/density ratios provides a method to control cohesive particle mixing and segregation.

By looking at the asymptotic state achieved in each experiment, we have shown that a liquid-bridging cohesion force may not only mitigate particle mixing, but alternatively enhance the possibility of segregation. Furthermore, the particle-level model that we have developed is able to accurately predict previously unreported results on the mixing and segregation of wet granular materials.

9.1.2 van der Waals cohesion

The impact of the van der Waals force on the behavior of particles becomes important when the size of particles is very small. A comprehensive examination of the behavior of colliding elastic-plastic particles in the presence of adhesion is conducted in this work. A computational model is developed to simulate systems which include van der Waals cohesion. This model can serve as a useful tool for further study of mixing and segregation of adhesive particles.

A characterization tool, Bo_{vdw}, is developed to quantify the impact of van der Waals forces on the particle mixing and segregation. The phase diagrams, which show both **M** and **E** phases, are essentially identical to those for wet granular materials when the varying cohesion strengths are plotted as $\sqrt{\Gamma_1/\Gamma_2}$ rather that $\cos\theta_1/\cos\theta_2$ (as is done for wet materials).

9.2 METHODOLOGY

In this work, we use both experiments and computations. Experimentally, since the capillary force between particles is a function of the wetting angle of the particles, we modify the particle surface chemistry in order to change the wetting characteristics (i.e., wetting angles). This enables us to investigate systems with varying degree of cohesion force. In addition, by chemically adding tracer-silane on the surfaces of particles, we can easily evaluate the differences between dry cases and wet cases both qualitative and quantitatively. Qualitatively, images are obtained with a CCD camera or digitalized-filming technique. Quantitatively, a C-language code has been developed to individually address and identify each pixel in an image so as to extract the particle distribution and ultimately calculate the standard deviation of concentration of pixels, i.e., the Intensity of Segregation.

We also have shown that Particle Dynamics simulation seems well suited for the study of cohesion in granular flow. This technique simultaneously integrates the interaction forces between individual pairs of particles, and calculates particle trajectories via the solution of

Newton's equation of motion for each particle. In a granular flow, the particles experience forces due to interactions between particles (e.g., collisions, contacts, or cohesive interactions) as well as interactions between the system and particles (e.g., gravitational forces). In PD, while the forces typically included only are gravity and contact force – normal (Hertzian) repulsion and tangential (Mindlin) friction, additional particle interaction such as cohesive forces can be easily added, and detailed information regarding particle concentrations, etc. may be easily calculated.

10.0 OUTLOOK

10.1 COHESIVE MIXING UNDER VAN DER WAALS FORCES

From Figure 38, we can see that the intensity of segregation (a measure of mixedness) changes most rapidly (i.e., the mixing rate is fastest) for an intermediate degree of cohesion[101]. In related work by Shinbrot *et al.*[141], they observed a qualitative change in flow pattern with a subsequent dramatic increase in mixing rate in cohesive tumbler systems. This observation is contrary to what is seen in our preliminary results where only a small increase in mixing rate is observed and qualitative differences in flow pattern are observed only at high Bo_g (see Figure 39)[101] – far from the mixing optimum.

This discrepancy may be attributed to the fact that *differing modes of cohesion* are at work in each case. Shinbrot *et al.*'s [141] work most likely represents van der Waals or perhaps electrostatic interactions (no moisture is present), while the work in our group on mixing to date involves liquid-induced cohesion. These differences in mixing behavior imply that different modes of cohesion may have a different impact on particle mixing/segregation.

Future work should be focused on the impact of different modes of cohesion (i.e., van der Waals force and capillary forces) on particle mixing. The following questions would be of interest in such a study:

- How does the presence of van der Waals interactions affect the diffusive mixing of particulate materials?
- Is the effect similar to that of the capillary force induced cohesion (the primary focus of the current work) or are the mechanics of these systems fundamentally different?
- What happens if multiple modes of cohesion are present (e.g., both van der Waals and capillary force exist in the system)?

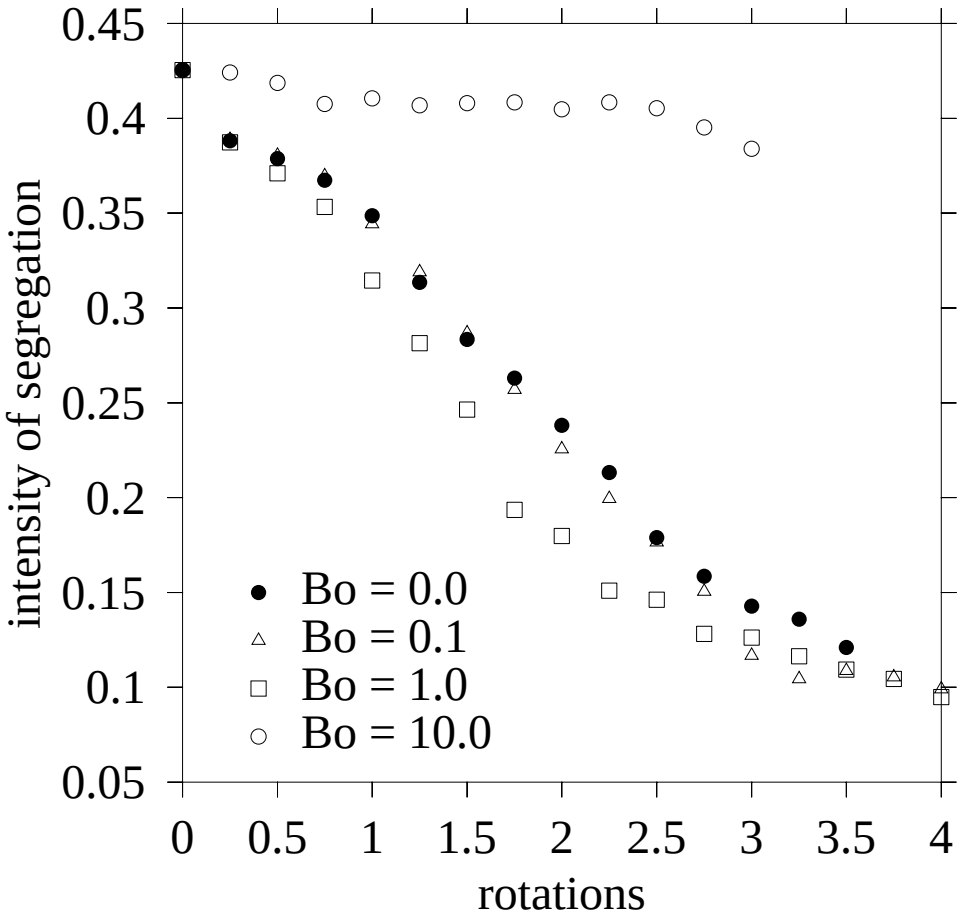

Figure 38: A quantitative comparison of mixing at different Bo_g numbers.

10.2 TECHNICAL APPROACH

It is relatively difficult to conduct experiments involving van der Waals forces due to the size of particles necessary, as well as the difficulty in limiting the effect of the side wall. Therefore it is expected that PD simulations should play a more significant role in future work in this area. Using the Particle Dynamics Simulations outlined in Section 8.0 it is possible to modify the mechanical properties of the particles such that differing segregation modes can be isolated and studied independently. Additionally, it is possible to modify the particle physical properties in ways which may not be practical in physical experiments. This would allow the examination of segregation due to cohesive differences by varying fluid-solid wetting angle, Hamker constants, electrostatic properties – properties that may be quite difficult to measure and/or control experimentally.

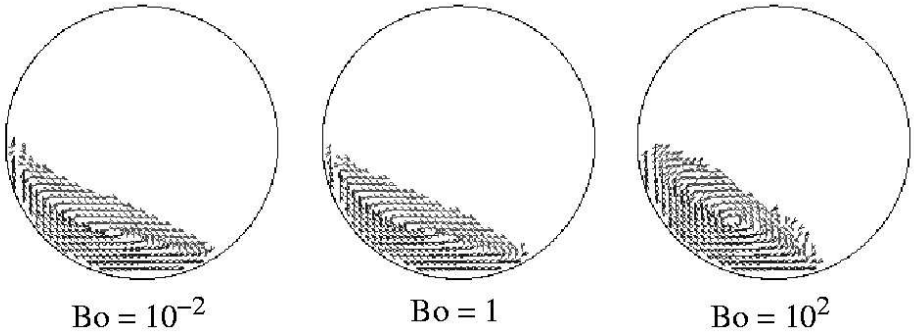

Figure 39: A comparison of flow patterns for tumblers at different Bo_g numbers. Note that qualitative differences are only observed at high Bo_g – far from the mixing optimum.

BIBLIOGRAPHY

[1] S. T. Nase, W. L. Vargas, A. A. Abatan, and J. J. McCarthy. Discrete characterization tools for wet granular media. *Powder Technology*, 116:214–223, 2001.

[2] C. Y. Wen and L. H. Chen. In Cheremisinoff N.P. and R. Gupta, editors, *The Handbook of Fluids in Motion*, pages 665–714. Ann Arbor Science, Ann Arbor, 1983.

[3] B.J. Ennis, J. Green, and R. Davies. The legacy of neglect in the us. *Chemical Engineering Progress*, 90:32–43, 1994.

[4] J. T. Jenkins and F. Mancini. Kinetic theory for binary mixtures of smooth,nearly elastic sphere. *Phy. Fluids A*, 1:2050–2057, 1989.

[5] W. S. Foo and J. Bridgwater. Particle migration. *Powder Technol.*, 36:271, 1983.

[6] S. B. Savage and C. K. K. Lun. *J.Fluid Mech.*, 189:311, 1988.

[7] R. P. Behringer. The dynamics of flowing sand. *Nonlinear Sci. Today*, 3:12–16, 1993.

[8] G.Metcalfe, T. Shinbrot, J.J. McCarthy, and J.M. Ottino. Avalanche mixing of granular materials. *Nature*, 374:39–41, 1995.

[9] C. Wightman, P.R. Mort, F.J. Muzzio, R.E. Riman, and R.K. Gleason. The structure of mixtures of particles generated by time-dependent. *Powder Technol.*, 84:231–240, 1995.

[10] D.W. Howell and R.P. Behringer. Fluctuation in granular media. *Chaos*, 9:559, 1999.

[11] T. Mullin. Mixing and de-mixing. *Science*, 295:1851, 2002.

[12] T. M. Knowlton, J.W. Carson, G. E. Klinzing, and W.C. Yang. The importance of storage, transfer, and collection. *Chemical Engineering Progress*, 90:44–54, 1994.

[13] J.C.Williams. Mixing and segregation in powders. In Martin Rhodes, editor, *Principles of powder technology*, pages 1–7. John Wiley and Sons, 1992.

[14] Melany Hunt. http://www.cco.caltech.edu/ granflow/homepage.html.

[15] A.W. Nienow, N. Harnby, and M. F. Edwards. Introduction to mixing problems. In N. Harnby, M. F. Edwards, and A. W. Nienow, editors, *Mixing in the Process Industries*, pages 10–16. Butterworths Heineman Publishers, London, 1992.

[16] In J. M. Ottino, editor, *The kinematics of mixing:stretching, chaos, and transport*. Cambridge University Press, Cambridge, 1990.

[17] J. Novosad and G. Standart. Studies on granular materials, iv. calculation of the shaft torque for mixing granular materials. *Collection of Czechoslovakian Chemical Communications*, 30:3247–3252, 1965.

[18] H. Li and J. J. McCarthy. Controlling cohesive particle mixing and segregation. *Physical Review Letters*, 90:18, 2003.

[19] D. Hornbaker, R. Albert, I. Albert, A.-L. Barabasi, and P.Schiffer. What keeps sandcastles standing. *Nature*, 387:765–767, 1997.

[20] M. Poux, P. Fayolle, and J. Bertrand. Powder mixing: some practical rules applied to agitated systems. *Powder Technology*, 68:213–234, 1991.

[21] L. T. Fan, Yiming Chen, and F. S. Lai. Recent developments in solid mixing. *Powder Technology*, 61:255–287, 1990.

[22] An introduction to the physics of granular materials. In J. Duran, editor, *Sands, powders, and grains*. Springer, New York, 1999.

[23] R. Hogg, N. S. Cahn, T. W. Healy, and D. W. Fuerstenau. Diffusional mixing in an ideal system. *Chemical Engineering Science*, 21:1025–1035, 1966.

[24] Tenda T., Komori S., and Murakami K. Modeling of mixing in a horizontal gas-solid agitated vessel with paddle-blades on double parallel axes. *Journal of Chemical Engineering of Japan*, 23:239–245, 1990.

[25] H. L. Bullock. Mixing in muller type mixers. *Chemical Engineering Process*, 51:243–248, 1955.

[26] J. M. Coulson and N. K. Maitra. The mixing of solid particles. *Industrial Chemistry*, February:55–59, 1950.

[27] H. E. Rose. A suggested equation relating to the mixing of powders and its application to the study of the performance of certain types of machine. *Transactions of the Institution of Chemical Engineering*, 37:4–12, 1959.

[28] J. Boss. Mixing time of grain materials. *Chemical Engineering Science*, 47:4027–4035, 1992.

[29] J. J. McCarthy. Mixing, segregation, and flow of granular materials. *Ph.D. thesis*, 1998.

[30] J. B. Lacey. Developments in the theory of particle mixing. *Journal of Applied Chemistry*, 4:257–267, 1954.

[31] G. Metcalfe and M. Shattuck. Pattern formation during mixing and segregation of flowing granular materials. *Phys. A*, 233:709–717, 1996.

[32] P. Arteaga and U. Tüzün. Flow of binary mixtures of equal density granules in hoppers-size segregation, flowing density, and discharge rates. *Chemical Engineering Science*, 45:205–223, 1990.

[33] M. Nakagawa, S.A. Altobelli, A. Caprihan, and E. Fukushima. NMRI study: axial migration of radially segregated core of granular mixtures in a horizontal rotating cylinder. *Chemical Engineering Science*, 52:4423–4428, 1997.

[34] D. Goodwill and A. Reed. Solving segregation problems in bins. *Proc. Eng.*, 70:49–50, 1989.

[35] J. Bridgwater. Fundamental powder mixing mechanisms. *Powder Technology*, 15:215–231, 1976.

[36] J.C. Williams. The segregation of particulate materials. *Powder Technology*, 15:245–251, 1976.

[37] In M. Rhodes, editor, *Introduction to particle technology*. John Wiley and Sons, New York, 1998.

[38] J.N. Israelachvelli. *Intermolecular and Surface Forces*. Academic Press, London, 1991.

[39] P. Pierrat and H. S. Caram. Tensile strength of wet granular materials. *Powder Technology*, 91:83–93, 1997.

[40] T. Mikami, H. Kamiya, and M. Horio. Numerical simulation of cohesive powder behavior in a fluidized bed. *Chem. Eng. Sci.*, 53:1927–1940, 1998.

[41] R. P. Behringer. The dynamics of flowing sand. *Nonlin. Sci. Tod.*, 3:12–16, 1993.

[42] C. M. Hrenya and J. L. Sinclair. On the effects of particle phase turbulence in dense gas-solids flow. *AIChE*, 43:853–861, 1997.

[43] P. Jiang, X. K. Luo, T. J. Lin, and L. S. Fan. High pressure and high temperature three-phase fludization – bed expansion phenomena. *Powder Technology*, 90:103–113, 1997.

[44] Gabriel I. Tardos. A fluid mechanistic approach to slow, frictional flow of powders. *Powder Technology*, 92:61–74, 1992.

[45] G. Debregeas and C. Josserand. A self-similar model for shear flows in dense granular materials. *Europhysics Lettes*, 52(2):137–143, 2000.

[46] S. Nasuno, A. Kudrolli, A. Bak, and J. P. Gollub. Time-resolved studies of stick-slip friction in sheared granular layers. *Physical Review E*, 58(2):2161–2171, 1998.

[47] S.T. Nase. Characterization of wet granular flow: application to mixing and segregation. *M.S. Thesis*, 2000.

[48] M.J. Adams and V. Perchard. The cohesive forces between particles with interstitial fluid. *Physical Review E*, 56(4):4467–4473, 1997.

[49] A. J. Goldman, R.G. Cox, and H. Brenner. Slow viscous motion of a sphere parallel to a plane wall - motion through a quiescent fluid. *Chem.Eng.Scie.*, 22:637–651, 1967.

[50] In J. Israelachvili, editor, *Intermolecular and Surface Forces*. Academic Press, San Diego, 1990.

[51] F. London. *Trans. Faraday Soc.*, 33:8–26, 1937.

[52] H.C. Hamaker. The london-van der waals attraction between spherical particles. *Physica*, 4:1058, 1937.

[53] In J.P.K. Seville, U. Tuzun, and R. Clift, editors, *Processing of Particulate Solids*. Blackie Academic and Professional, London, 1997.

[54] R. Albert, I. Albert, D. Hornbaker, P. Schiffer, and A.-L. Barabási. The angle of repose in wet and dry granular media. *Physical Review E*, 56:R6271–R6276, 1997.

[55] L Bocquet, E Charlaix, S Ciliberto, and J Crassous. Moisture-induced ageing in granular media and the kinetics of capillary condensation. *Nature*, 396:735–737, 1998.

[56] P. Tegzes, R Albert, M. Paskvan, A. L. Barabasi, T. Vicsek, and P. Schiffer. Liquid-induced transitions is granular media. *Physical Review E*, 60:5823, 1999.

[57] A. Samadani and A. Kudrolli. Segregation transitions in wet granular matter. *Phys. Rev. Lett.*, 85:5102–5105, 2000.

[58] D. Geromichalos, F. Mugele M. Kohonen, and S. Herminghaus. Mixing and condensation in a wet and dry granular media. *Phys. Rev. E.*, 56:R6271–R6276, 1997.

[59] H. Li and J.J. McCarthy. Phase diagrams for cohesive particle mixing and segregation. *Physical Review E*, 71:021305, 2005.

[60] S. M. Iveson and J. D. Litster. Fundamental studies of granule consolidation: Part 1. effects of binder surface tension. *Powder Technol.*, 88:15–20, 1996.

[61] S. M. Iveson and J. D. Litster. Fundamental studies of granule consolidation: Part 1. quantifying the effects of binder surface tension. *Powder Technol.*, 99:243–250, 1998.

[62] R.P. Zou, J.Q. Xu, C.L. Feng, A.B. Yu, S. Johnston, and N. Standish. Packing of multi-sized mixtures of wet coarse spheres. *Powder Technology*, 130:77–83, 1991.

[63] Martin Rhodes. Introduction to particle technology. page 132. John Wiley and Sons Ltd., West Sussex, England, 1997.

[64] Brian H. Kaye. Powder mixing. page 132. Chapman and Hall, London, 1997.

[65] In B. J. Ennis and J. D. Litster, editors, *Section 20: Size enlargement, in Perry's Chemical Engineerings' Handbook, 7th Edition,*. McGraw-Hill, New York, 1997.

[66] J.C.Williams. Mixing and segregation in powders. In Martin Rhodes, editor, *Principles of powder technology*, pages 71–90. John Wiley and Sons, 1992.

[67] J.A.Hersey, W.J.Thiel, and C.C.Yeung. Partially ordered randomized powder mixtures. *Powder Technology*, 24:251–256, 1979.

[68] ed. C. Thornton. Special issue of numerical simulations of discrete particle systems. *Powder Technology*, 109, 2000.

[69] K. Kuwagi, T. Mikami, and M. Horio. Numerical simulation of metallic solid bridging particles in a fluidized bed at high temperature. *Powder Technology*, 109 (1):27–40, 2000.

[70] Bardet J. P. Introduction to computational granular mechanics. In B. Cambou, editor, *Behavior of granular materials*, pages 99–169. Springer-Verlag, 1998.

[71] Yen K.Z.Y. and T.K. Chaki. A dynamic simulation of particle rearrangement in powder packings with realistic interactions. *J. Appl. Phys.*, 71:3164–3173, 1992.

[72] Thornton C. and C. W. Randall. Applications of theoretical contact mechanics to solid particle system simulation. In M. Satake and J. T. Jenkins, editors, *Micromechanics of Granular Material*, pages 133–142. Elsevier Science Publishers, Amsterdam, 1988.

[73] Satake M. Constitution of mechanics of granular materials through the graph theory. In S.C. Cowin and M. Satake, editors, *U.S.-Japan Seminar in Continuum Mechanics and Statistical Approaches in the Mechanics of Granular Materials*, pages 47–62. 1978.

[74] Tai Q. M. and M. H. Sadd. A discrete element study of the relationship of fabric to wave propagational behaviours in granular material. *Int. J. Numer. Anal. Meth. Geomech.*, 21:295–311, 1997.

[75] Kaneko Y., Shiojima T., and M. Horio. Dem simulation of fluidized beds for gas-phase olefin polymerization. *Chemical Engineering Science*, 54:5809–5821, 1999.

[76] Tsuji Y., Kawaguchi T., and T. Tanaka. Discrete particle simulation of two-dimensional fluidized bed. *Powder Technology*, 77:79–87, 1993.

[77] O.R. Walton and R.L. Braum. Viscosity,granular-temperature, and stress calculations for shearing assemblies of inelastic,frictional disks. *J. Rheol.*, 30:949–980, 1986.

[78] Herrmann H. J. and S. Luding. Modeling granular media on the computer. *Continuum Mech. Thermodyn.*, 10:189–231, 1998.

[79] Campbell C. S. Rapid granular flows. *Annu. Rev. Fluid Mech.*, 22:57–92, 1990.

[80] Ng T-T. Small-strain response of random arrays of spheres using dem. *J. Eng. Mech.*, 122:239–244, 1996.

[81] Thornton C. Numerical simulations of deviatoric shear deformation of granular media. *Géotechnique*, 50:43–53, 2000.

[82] C. Thornton. Force transmission in granular media. *KONA*, 15:81–90, 1997.

[83] C. Thornton, K. K. Yin, and M. J. Adams. Numerical simulation of the impact fracture and fragmentation of agglomerates. *Journal of Physics D: Applied Physics*, 29:424–435, 1996.

[84] D. V. Khakhar, J. J. McCarthy, and J. M. Ottino. Radial segregation of granular materials in rotating cylinders. *Phys. Fluids*, 9:3600–3614, 1997.

[85] P.A. Cundall and O.D.L. Strack. A discrete numerical model for granular assemblies. *Geotechnique*, 29:47–65, 1979.

[86] C.S.Campbell and C.E.Brennen. *J. Appl. Mech.*, 52:172–178, 1985.

[87] J. J. McCarthy and J. M. Ottino. Particle dynamics simulation: A hybrid technique applied to granular mixing. *Powder Technology*, 97:91–99, 1998.

[88] In C. Thornton, editor, *Powder Technology-Special Issue on Computer Modeling*. Elsevier Science Publishes, Amsterdam, 2000.

[89] In M. P. Allen and D. J. Tildesley, editors, *Computer simulation of Liquids*. Oxford Science Publication, Oxford, 1987.

[90] C. Thornton. Coefficient of restitution for nonlinear collisions of elastic-perfectly plastic spheres. *J. Appl. Mech.*, 64:383–386, 1997.

[91] K. L. Johnson. In *Contact Mechanics*. Cambridge University Press, Cambridge, 1987.

[92] O. R. Walton. Numerical simulation of inclined chute flows of monodisperse, inelastic, frictional spheres. *Mech. Mat.*, 16:239–247, 1993.

[93] Mindlin R. D. Compliance of elastic bodies in contact. *J. Appl. Mech.*, 16:256–270, 1949.

[94] G. Lian, C. Thornton, and M. J. Adams. A microscopic simulation of oblique collisions of 'wet' agglomerates. In R. P. Behringer and J. T. Jenkins, editors, *Powders and Grains 97*, pages 223–226. Balkema, Rotterdam, 1997.

[95] G. Lian, C. Thornton, and M.J. Adams. Discrete particle simulation of agglomerate impact coalescence. *Chem. Eng. Sci.*, 53:3381–3391, 1998.

[96] R. A. Fisher. On the capillary forces in an ideal soil. *J. Agric. Sci.*, 16:491–505, 1926.

[97] K. D. Kafui, C. Thornton, and M. J. Adams. Discrete particle-continuum fluid modeling of gas-solid fluidised beds. *Chemical Engineering Science*, 57:2395–2410, 2002.

[98] Y. Li, J. Zhang, and L. Fan. Numerical simulation of gas-liquid-solid fludization systems using a combined cfd-vof-dpm method: bubble wake behavior. *Chemical Engineering Science*, 54:5101–5107, 1999.

[99] T. Kawaguchi, M Sakamoto, and Y. Tsuji. Quasi-three-dimensional numerical simulation of spouted beds in cylinder. *Powder Technology*, 109:3–12, 2000.

[100] B. K. Mishra and Thornton C. Impact breakage of particle agglomerates. *Int. J. Miner. Process*, 61:225–239, 2000.

[101] J.J. McCarthy. Micro-modeling of cohesive mixing processes. *Powder Technology*, 138:63–67, 2003.

[102] K. Jain, D. Shi, and J. J. Mccarthy. Discrete characterization of cohesion in gas-solid flows. *Powder Technol.*, 146:160–167, 2004.

[103] R. A. Bagnold. Experiments on a gravity-free dispersion of large solid spheres in a newtonian fluid under shear. *Proc. Roy. Soc..*, 225:4–63, 1954.

[104] P.L.Stephenson and W.J. Thie. The effect of humidity on the production of ordered mixtures. *Powder Technology*, 25:115–119, 1980.

[105] P.L. Stephenson and W.J. Thiel. The effect of humidity on the production of ordered mixtures. *Powder Technology*, 25:115–119, 1980.

[106] N. Harnby. The mixing of cohesive powders. In N. Harnby, M. F. Edwards, and A. W. Nienow, editors, *Mixing in the Process Industries*, pages 78–94. Butterworths Heineman Publishers, London, 1992.

[107] Hsiau SS, Tai CH, and Chiang MC. Effect of moisture content on the convection motion of powders in a vibrated bed. *Advanced Powder Technology*, 15:673–686, 2004.

[108] Hsiau SS, Tai CH, and Chiang MC. Effect of interparticle force on mixing and segregation of dry granular materials. *Physical Review E*, 70(3):031301, Sep., 2004.

[109] Stambaugh J, Smith Z, Ott E, and *et al.* Segregation in a monolayer of magnetic spheres. *Physical Review E*, 70(3):031304, Sep., 2004.

[110] Kohonen MM, Geromichalos D, Scheel M, and *et al.* On capillary bridges in wet granular materials. *Physica A -Statistical mechanics and its applications*, 339(1-2):7–15, Aug., 2004.

[111] Jain N, Ottino JM, and Lueptow RM. Effect of interstitial fluid on a granular flowing layers. *Journal of fluid mechanics*, 508:23–44, June, 2004.

[112] Kudrolli A. Size separation in vibrated granular matter. *Reports on progress in physics*, 67(3):209–247, Mar., 2004.

[113] G. Lian, C. Thornton, and M. J. Adams. A theoretical study of liquid bridge forces between two rigid spherical bodies. *J. Colloid Int. Sci.*, 161:138–147, 1993.

[114] S. Torquato. Hard knock for thermodynamics. *Nature*, 405:521–523, 2000.

[115] R.W. Coughlin, B. Elbirli, and L.Vergara-Edwards. Interparticle force conferred by capillary-condensed liquid at contact points. *J. Colloid Int. Sci.*, 87:18–30, 1982.

[116] McCarthy J. J., Shinbrot T., Metcalfe G., Wolf J. E., and J. M. Ottino. Mixing of granular materials in slowly rotated containers. *AIChE Journal*, 42:3351–3363, 1996.

[117] Ding Y. L., R. N. Foster, J. P. Seville, and D. J. Parker. Scaling relationships for rotating drums. *Chemical Engineering Science*, 56:3737–3750, 2001.

[118] Mellman J. The tranverse motion of solids in rotating cylinders-forms of motion and transition behavior. *Powder Technology*, 118:251–270, 2001.

[119] Boateng A. A. and P. V. Barr. Modeling of particle mixing and segregation in the transverse plane of a rotary kiln. *Chemical Engineering Science*, 51:4167–4181, 1996.

[120] Boateng A. A. and P. V. Barr. Granular flow behaviour in the transverse plane of a partially filled rotating cylinder. *J. Fluid Mech.*, 330:233–249, 1997.

[121] Ito N., Obata K, and T. Hakuta. Heat transfer from the wall to a particle bed in a rotary drum. *Kagaku Kogaku Ronbunshu*, 9:628–634, 1983.

[122] Hill K. M., A. Caprihan, and J. Kakalios. Bulk segregation in rotated granular material measured by magnetic resonance imaging. *Physics Review Letters*, 78:50–53, 1997.

[123] J. F. Gilchrist D. V. Khakhar, J.J. McCarthy and J. M. Ottino. Chaotic mixing of granular materials in two-dimensional tumbling mixers. *Chaos*, 9:195–205, 1999.

[124] D. V. Khakhar, J. J. McCarthy, T. Shinbrot, and J. M. Ottino. Transverse flow and mixing of granular materials in a rotating cylinder. *Phys. Fluids*, 9 (1):31–43, 1997.

[125] C. M. Dury and G. H. Ristow. Competition of mixing and segregation in rotating cylinders. *Physics of Fluids*, 11:1387, 1999.

[126] J. J. McCarthy, D. V. Khakhar, and J. M. Ottino. Computational studies of granular mixing. *Pow. Technol.*, 109:72, 2000.

[127] D.V. Khakhar, A. V. Orpe, and S. K. hajra. Segregation of granular materials in rotating cylinders. *J. Phys. A*, 318:129, 2003.

[128] Peterson D., Hu S.H., Richards C.D., and R.F. Richards. The measurement of droplet temperature using thermochromic liquid crystals. *30th National Heat Transfer Conference*, 1995.

[129] Fortner B. and T.E. Meyer. *Number by Colors*. Springer-Verlag, New York, 1997.

[130] C. Thornton and K. K. Yin. Impact of elastic spheres with and without adhesion. *Powder Technology*, 65:153–166, 1991.

[131] Gabriel I. Tardos and M. Irfan Khan. Forces on a slowly rotating, rough cylinder in a couette device containing a dry, frictional powder. *Physics of Fluids*, 10(2):335–341, 1997.

[132] Mylene Lubert and Alain Ryck. Slip events and dilatancy in a sheared fine noncohesive powder. *Physical Review E*, 63:021502(1–7), 1997.

[133] S. B. Savage and S. McKeown. shear stresses developed during rapid shear of concentrated suspensions of large particles between concentric cylinders. *J. Fluid Mech.*, 127:453, 1983.

[134] J. L. Lenhart, J. H. van Zanten, J. P. Dunkers, C. G. Zimba, C. A. James, S. K. Pollack, and R. S. Parnas. Immobilizing a fluorescent dye offers potential to investigate the glass/resin interface. *J. Colloid Int. Sci.*, 221:75–86, 2000.

[135] A R. Savkoor and G. A. D. Briggs. The effect of tangential force on the contact of elastic solids in adhesion. *Proc. R. Soc. Lond. A*, 356:103–114, 1977.

[136] Thornton C. and Ning Z. A theoretical model for the stick/bounce behavior of adhesive, elastic-plastic spheres. *Powder Technoloy*, 99:154–162, 1998.

[137] Johnson K. L., Kendall K., and A. D. Robert. Surface energy and the contact of elastic solids. *Proceedings of the Royal Society of London, A*, 324:301–313, 1971.

[138] B. V. Derjaguin, V. M. Muller, and Y. U. P Toporov. Effect of contact deformation on the adhesion of particles. *Journal of colloid and interface science*, 52:105–108, 1975.

[139] Mindlin R. D. and Deresiewicz H. Compliance of elastic bodies in contact. *J. Appl. Mech.*, 20:327, 1953.

[140] G. V. Dedkov. Experimental and theorectical aspects of the modern nanotribology. *Phys. Stat. Sol. (a)*, 179:3–75, 2000.

[141] T. Shinbrot, A.W. Alexander, and F.J. Muzzio. Spontaneous chaotic mixing. *Nature*, 397:675–678, 1999.